Copyright

by

Mykhailo Fomyts'kyi

2004

The Dissertation Committee for Mykhailo Fomyts'kyi
certifies that this is the approved version of the following dissertation:

Numerical Simulation of High Intensity Laser-Plasma Interaction

Committee:

Charles Chiu, Supervisor

Boris Breizman , Supervisor

Todd Ditmire

Mike Downer

Wendell Horton

Robert van de Geijn

Numerical Simulation of High Intensity Laser-Plasma Interaction

by

Mykhailo Fomyts'kyi, BS

Dissertation

Presented to the Faculty of the Graduate School of

The University of Texas at Austin

in Partial Fulfillment

of the Requirements

for the Degree of

Doctor of Philosophy

The University of Texas at Austin

August 2004

Dedicated to world peace and peaceful use of science

Acknowledgments

There are many people whom I would like to thank for their help and support during my work on this dissertation. First of all, I would like to express my gratitude to my supervisors Charles Chiu and Boris Breizman, who have helped me a great deal in my professional growth and whose guidance was essential for the success of this work. I would like to thank them both for sharing their experience with me during many hours of discussion and for their invaluable help in my academic and professional development.

I would like to express my special appreciation to Mike Downer and his group for introducing me to the magical (for a theorist) world of state-of-the-art modern experimental physics. Working closely with Mike and his group inspired a lot of fruitful discussions and exchange of ideas, which motivated a number of breakthroughs on both the theoretical and the experimental sides.

I acknowledge Todd Ditmire and his group for helping me understand cluster experiments and for the valuable discussions, which have led to a better understanding of cluster physics.

My special thanks to Robert van de Geijn for bringing my skills of scientific computing to a new level.

Alexey Arefiev and Andrew Cole are thanked for studying and taking study breaks together, for mutual support, and for our exchange of ideas and jokes. I appreciate Sergey Kalmykov for his advice on wakefield and recommendations on jazz and beer. Also, I would like to thank Taras Kirichenko for being a true friend for almost a decade of my university life starting from Moscow and now in Austin.

I am grateful to the Physics Department, IFS, NSF FOCUS center, and DOE for their financial support of my education.

Finally, I would like to thank my wife Maggie, my parents, and my brother for their love, support, and encouragement.

MYKHAILO FOMYTS'KYI

The University of Texas at Austin
August 2004

Numerical Simulation of High Intensity Laser-Plasma Interaction

Publication No. ______________

Mykhailo Fomyts'kyi, Ph.D.
The University of Texas at Austin, 2004

Supervisors: Charles Chiu and Boris Breizman

In this work two different areas of high intensity laser-plasma interaction are considered. The first part of the dissertation describes the dynamics of laser-irradiated clusters. It addresses two different regimes of laser-cluster interactions. In the so-called Coulomb regime, the laser pulse removes a significant part of the electrons from the cluster. The remaining electrons form a cold electron core inside a positively charged ion shell. The ion shell expands due to its space charge. A different situation occurs in the so-called hydrodynamic regime. In this case, a two-component electron distribution is formed in the cluster due to stochastic vacuum heating. The cluster remains quasi-neutral and it expands due to the hot electron pressure. Understanding electron and ion dynamics in both these regimes is the main goal of the first part of the dissertation. Stochastic vacuum heating of the electrons is demonstrated in the hydrodynamic regime. Anisotropy in cluster expansion is predicted and the sign of the anisotropy is found to depend on the laser intensity. A model of harmonic generation in clusters is developed. Resonant enhancement of harmonic generation during cluster expansion is demonstrated. Our theoretical models are verified and extended via numerical simulations using a newly-developed particle-in-cell axisymmetric electrostatic code.

The second part of the dissertation deals with laser wakefield acceleration in the self-modulation regime seeded by a Raman shifted low amplitude laser pulse. Raman seeding provides means of coherent control of the excited wakefield. The energy threshold for pulse modulation in the diffraction limited regime is derived. The relative roles of the seed and the leading edge of the pulse in creating an initial perturbation are compared. One dimensional and two dimensional particle-in-cell simulations are employed to model the effects of the seed pulse. Examples of coherent control are demonstrated. Numerical simulations show that a 38 mJ Raman seeded pulse can generate relativistic bunches of ~ 1 nC. Conventional (unseeded) self-modulated laser wakefield acceleration would require significantly more energetic pulses at relativistic intensities for generating similar electron bunches. Our results indicate that a pulse repetition rate of ~ 1 kHz may be feasible with proper Raman seeding. The simulation also demonstrate the possibility of Raman-seeded acceleration by pulses of *subcritical* power ($P = 1/2P_c$, 19 mJ) in a plasma channel.

Contents

Chapter 1

Introduction

1.1 High intensity laser-plasma interaction

One of the major breakthroughs in laser technology is the invention in the early 1990s of chirped pulse amplification [1]. This has lead to creation of high power lasers, known as "table-top-terawatt" or "T^3" lasers. These lasers have very short pulselength of $10-100$ fs and very high intensities of $10^{15} - 10^{19}$ W/cm^2. These intensities are significantly greater than the ionization threshold, which is $\sim 10^{14}$ W/cm^2 for hydrogen. The matter easily becomes plasma during interaction with such pulses. For this reason plasma physics approach is appropriate for describing high intensity regime. Over the past few decades, the area of high intensity laser-plasma interaction has become very diverse, giving rise to the broad experimental and theoretical research with conceivable applications from particle acceleration [2] to nuclear fusion [3].

Laser interactions with plasma can be subdivided into three categories. The first one is the interaction with low density (*underdense*) plasma. In this regime, the laser frequency ω_0 is typically much larger than the plasma frequency. Therefore, the dielectric constant $\epsilon = 1 - \omega_p^2/\omega_0^2$ is close to unity and the laser pulse can propagate in the plasma. At high intensities the laser pressure can excite strong oscillations of plasma density. The shape of the pulse can be significantly affected by laser-plasma instabilities. One of the important applications of this interaction is utilizing the field of the excited wave, also referred to as wake, for acceleration of charged particles.

The second regime is typical for laser-solid interaction or interaction with *overdense* plasma ($\omega \ll \omega_p$). In this regime, the dielectric constant ϵ is negative and the electromagnetic wave interacts primarily with plasma surface. For high intensity pulses a number of interesting phenomena have been studied in this regime such as harmonic generation [4, 5, 6], electron and ion acceleration [7, 8], and inertial fusion [9].

The third regime corresponds to a cluster medium. A cluster is a large group (10^3-10^6) of atoms held together by van der Waals forces [10]. A cluster gas can be viewed as an intermediate state between gas and solid media, because the plasma is underdense on average, but each individual solid cluster is overdense. As a result, cluster medium can behave very different from both low density plasmas and solids. In particular, electrons in clusters can effectively absorb laser energy compared to the gas or solid targets [11] and transfer this energy to the ions [12, 13]. The intense study of laser-irradiated clusters was motivated by the experimental demonstration of X-ray generation [14, 15], creation of extremely hot plasmas, and fusion neutron production [3].

This dissertation addresses two different topics. First, in Part I, we study nonlinear laser-cluster interaction. A cluster, being a rather simple object, offers a lot of very interesting physics [16]. We assume that all atoms in the cluster are completely ionized, which usually applies to low Z materials in the strong field. Assuming complete ionization and, thus, reducing the problem to plasma physics allows us to advance further both analytically and numerically in the cases relevant to experiment, e.g. fusion experiments with deuterium clusters, where plasma effects are dominant.

There are two possible scenarios of laser-cluster interaction. In the so-called Coulomb regime, a significant part of the electrons is removed from the cluster by the laser pulse. Remaining electrons form an electron core inside an ion shell of the cluster [17]. The shell of uncompensated ions expands due to its space charge. In the other case (hydrodynamic regime) a two component electron distribution builds up in the cluster due to stochastic vacuum heating. The cluster remains quasi-neutral in this case and it expands due to the hot electron pressure.

In order to study electron and ion dynamics in these regimes, we have developed an efficient particle-in-cell code. We combine theoretical and numerical approaches to study formation of the electron core and collective core oscillations in uniform and nonuniform clusters. Analytical solutions are used to benchmark the code. As mentioned above, clusters are very effective in absorbing laser energy. Several models of absorption have been suggested [18, 17, 16]. We use numerical simulations to study stochastic vacuum heating of electrons and formation of the two component electron distribution [17].

Anisotropy in cluster expansion was experimentally observed by several groups [19, 20, 21]. Our study shows that the degree of anisotropy depends on the laser pulse intensity. In the hydrodynamic regime anisotropic expansion arises from anisotropy of the electron temperature. In the Coulomb regime, the expansion anisotropy is associated with anisotropic oscillations of the electron core.

We also study nonlinear response of a cluster with particular attention to the third harmonic generation. This study is motivated by recent experiments [22, 10]. Understanding harmonic generation in clusters is important, because it can provide a valuable diagnostic tool. Higher harmonics are also of interest for creating a source of coherent soft X-rays. Our newly developed model of harmonic generation [23] is based on the nonlinear response of the electron core in a nonuniform cluster. It is noteworthy, that numerical simulation allows us to study harmonic generation in an expanding cluster, which reveals resonance enhancement of harmonic generation when the the cluster eigenfrequency matches the third harmonic of the laser frequency.

The second part of the dissertation, Part II, deals with optimization and controll of laser wakefield acceleration (LWFA). LWFA is acceleration of electrons (or other charged particles) to relativistic speeds by the electric field of the plasma wave, excited by a laser pulse. The major advantage of this type of acceleration is that plasma can sustain electric field of high amplitude, which is determined by the plasma density. For example, for plasma density $n = 10^{19}$ cm^{-3} the maximum field amplitude is given by $E_{max} = m_e c\,\omega_p/e \approx$ 1 TeV/m. In contrast with this, in a linear radio-frequency (RF) accelerator, the maximum field is determined by the breakdown on the walls of the structure, which is limited to a much smaller value $\sim$ 100 MeV/m. Acceleration of the particles to large energies required for modern high energy experiments requires, therefore, extended acceleration structures.

Plasma based accelerator can *potentially* reduce the acceleration distances to centimeters and the whole accelerator to the size of a table-top laser system. This will significantly reduce the cost of accelerators, what makes the wide spread of their practical applications more feasible. However, despite enormous acceleration gradients in plasma-based accelerators, the electron bunches produced by current LWFA experiments can not compete with linear accelerators neither in peak or average current nor in the beam energy. The underlying reason is that it is very difficult to create extended regular acceleration structures in plasma, because the interaction length is limited by pulse diffraction, electron bunch dephasing, and laser-plasma instabilities [2].

Of the various methods of driving large-amplitude plasma waves [2], the self-modulated laser wakefield accelerator (SM-LWFA) [24, 25, 26] has so far yielded electron bunches of the highest energy (tails $>$ 200 MeV [27]), charge ($>$1 nC/bunch [28, 29]) and collimation (transverse emittance $\epsilon_\perp < 0.1\pi$ mm $\cdot$ mrad [30]). The beam properties achieved in SM-LWFA experiments [28, 29, 31, 32, 33] are favorable enough for near-term applications such as table-top nuclear activation of rare isotopes [29], injectors for conventional high-energy physics accelerators, and radiation oncology [34, 35, 36].

In Part II we study the applicability of Raman seeding technique for enhancing particle production and controll of the wakefield excitation and particle acceleration. In this scheme, the main pulse with frequency ω_0 is combined with a significantly weaker *seed* pulse of frequency $\omega_0 - \omega_p$ [37, 38, 39]. The beating of the two pulses resonantly excites a plasma wave, which serves as an initial perturbation for modulation instability [40]. We show that when the interaction length is limited by diffraction, the development of the pulse modulation is determined by the pulse energy only. As a result, low energy pulses can not acquire significant modulation unless the instability develops from a finite amplitude seed rather than from a noise. We study the affect of the seed on the development of the pulse modulation and wakefield excitation.

In particular, we show that by varying seed parameters one can control the timescale of the modulation and the phase of the excited wake. The latter is very important for multistage acceleration or when external electron injection is used.

Up to now electron production in SM regime in experiments has been associated with high intensity pulses, where the power of the laser pulse is greater than the critical power, i.e. $P > P_c$. We investigate the possibility of utilizing Raman seed for electron production by pulses in the sub-critical power domain. In this domain, we also investigate how channeling further lowers the production threshold.

1.2 Role of the numerical simulations

Both laser-cluster interaction and wakefield acceleration involve intrinsically nonlinear phenomena that are often too complicated for purely analytical treatment. In order to extend the study beyond the limitations of the of the analytical theory, we employ numerical simulations, which is a substantial part of this work. Due to complexity and diversity of laser-plasma interaction, it is virtually impossible or at least impractical to write a code capable of simulating all possible scenarios. Instead, we will tailor numerical algorithm to a specific problem at hand. Most of the problems require kinetic treatment. The standard tool for this is particle-in-cell (PIC) codes [41, 42]. In these codes, the plasma of 10^{15}-10^{20} real particles (unrealistic number for simulation on the largest supercomputers) is modeled by 10^4-10^7 macroparticles of proportionally larger charge and mass. The latter is routinely simulated on personal computers. The plasma frequency for macroparticles is the same as that for the real plasma, so are the dispersion relation and the distribution function. The unphysical collisional effects between macroparticles, caused by their artificially large charge, are suppressed numerically in PIC algorithm. The problem with PIC codes is that most of the problems involve multiple scales. For example, in laser-cluster interaction the cluster size R is typically much smaller than the laser wavelength λ. In wakefield problems one has to deal with the laser wavelength λ, plasma wavelength λ_p, and the pulse length $c\,\tau_{\text{pulse}}$. The size of the simulation domain is usually determined by the largest scale, whereas the smallest scale has to be resolved by significant ($\gg 1$) number of macroparticles. As a result, the total number of particle involved in the simulation, and, therefore, simulation time for a PIC code may become very large. In practice, only 1D full-scale simulations are affordable if a parameter scan is required. A few 2D simulations are possible on current personal computers and a limited parameter scan is possible with the help of supercomputers. 3D simulation are currently state-of-art and typically the simulation of only a few points in the parameter space is affordable even on supercomputers.

A better approach is to use as much knowledge about the physics of the problem at hand as possible, in order to reduce the problem to a simpler formulation, which can be simulated more efficiently. Code optimization can speed up simulation by tens of percent, algorithm optimization can improve the performance by hundreds or thousands percent. A relevant reduction of the physics problem can easily improve the performance of the code by orders of magnitude.

In order to simulate cluster response to the laser field, we take advantage of the fact that the problem becomes electrostatic for small clusters and moderate laser intensities(see Part I Sec. 5.1 for details). The smallest scale in this problem is the cluster size, rather than laser wavelength. Furthermore, if the laser pulse is linearly polarized, the problem becomes axisymmetric i.e. 2D. We thereby reduce the problem of a 3D cluster response to the laser field to a much simpler one. The corresponding code developed allows to solve the reduced problem of laser-cluster interaction on a personal computer.

The simulation of wakefield excitation also allows similar reduction of scales. In the so-called envelope approximation, only the evolution of the envelope of the laser pulse and the corresponding slowly varying ponderomotive force are considered. As a result, the smallest scale in the problem becomes plasma wavelength λ_p, which reduces the simulation time. We implemented a code, which combines this approach with fluid description of the plasma. This code is very effective for simulation of 2D wakefield excitation and some 2D effects of the pulse evolution, such as diffraction, channel guiding and relativistic self-focusing. However, it can not simulate SM-LWFA because wavebreaking and particle trapping cannot be described within fluid model. For this regime a PIC code is required. We used VORPAL code [43, 44, 45], which provides vast flexibility in specifying initial and boundary conditions, allows easy switching between numerical models, and simulation of 1D, 2D, and 3D problems.

Part I

Nano-clusters in an intense laser field

Chapter 2

Electron dynamics

2.1 Cold electron core equilibrium

Our study of the electron dynamics is based on the electron core model developed in Ref. [17]. In this introduction, we describe the assumptions and the main ingredients of this model.

The typical laser intensity in cluster experiments [10] is in the range of $10^{15} - 10^{16}$ W/cm^2, which is significantly larger than the ionization threshold ($\sim 10^{14}$ W/cm^2 for hydrogen). Therefore, the cluster becomes ionized at the very beginning of the laser pulse. For light atoms like hydrogen or helium the ionization is complete; for heavy atoms partial ionization may lead to additional effects that will not be discussed here.

A typical cluster size is 2-100 nm, which is much smaller than laser wavelength ($\sim 1\mu$). This implies that the laser field can be treated as a uniform in space function of time.

Inside the cluster, the plasma frequency ω_p is much larger than the laser frequency ω_0. In response to the laser electric field $E_0 \cos(\omega_0 t)$, the electrons inside the cluster move adiabatically in order to partially compensate the applied field. First, consider a uniform cluster when an external electric field of amplitude E_0 is introduced quasi-statically. As the field increases it extracts some electrons from the cluster. The extracted electrons cross the cluster boundary, accelerate, and leave. The remaining electrons form a spherical core inside the cluster as shown in Fig. 2.1. In order to see that this charge configuration corresponds to an equilibrium, we calculate the electric field inside the electron core displaced by distance d from the center.

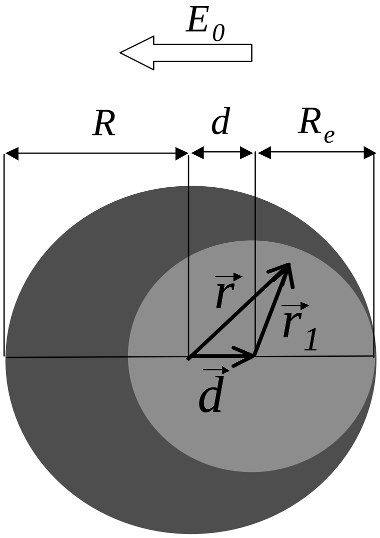

Figure 2.1: Electron core in a uniform spherical cluster [17]. The core adiabatically responds to the laser field.

$$\bar{\mathbf{E}} = \frac{4\pi Ne}{3}\bar{\mathbf{r}} - \frac{4\pi Ne}{3}\bar{\mathbf{r}}_{\mathbf{1}} + \bar{\mathbf{E}}_0 = \frac{4\pi Ne}{3}\bar{\mathbf{d}} + \bar{\mathbf{E}}_0, \tag{2.1}$$

where N is the ion density, $-e$ is the electron charge.

Note, that the field inside the electron core is uniform and depends only on the core displacement $\bar{\mathbf{d}}$ and the external field $\bar{\mathbf{E}}_0$. The core is in the equilibrium when

$$\bar{\mathbf{d}} = -3\frac{\bar{\mathbf{E}}_0}{4\pi N e} = -3\frac{e\bar{\mathbf{E}}_0}{m\omega_p^2}. \tag{2.2}$$

The radius of the electron core is given by

$$R_e = R - d. \tag{2.3}$$

If the external field is turned off, the core will move to the center. In this configuration the electron core is surrounded by the ion shell of thickness d. In the presence of a time dependent external field $E(t)$, which changes slowly compared to the plasma frequency ω_p, the core electrons will move as a rigid body in order to compensate the external field as long as the core does not cross the boundary of the cluster $E(t) \leq E_0$. If the core crosses the cluster boundary, then it looses some electrons and shrinks. In general, the radius of the core is given by [17]

$$R_e = R - \frac{3e}{m\omega_p^2}\max_{0\leq t'\leq t}(|E(t')|). \tag{2.4}$$

Once extracted from the cluster, electrons may never come back. This happens when the electron excursion is much larger than the cluster radius. In this case, the kinetic energy of an extracted electron exceeds the bounding potential of the charged cluster. For a sinusoidal laser field, $E = E_0\cos(\omega_0 t)$, the electron excursion is roughly $\zeta = eE_0/m\omega_0^2$. Therefore, the extracted electrons escape when $\zeta \gg R$.

We have used particle-in-cell simulation (See Chapter 5 for a detailed code description) to illustrate the process of electron core formation described above. Fig. 2.2 shows the evolution of the charge configuration as the external field quasi-statically increases to the value E_0.

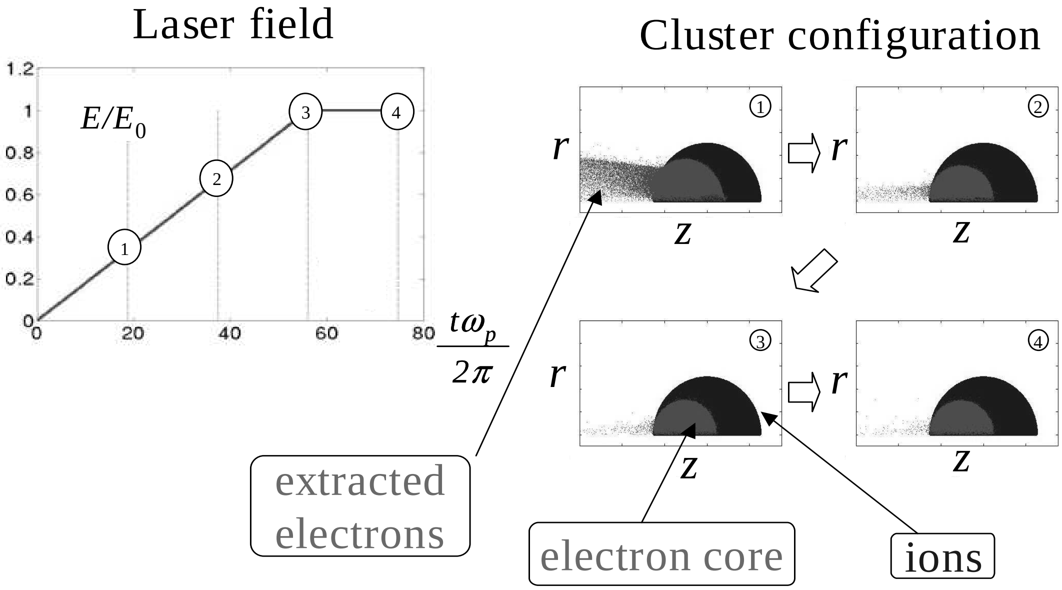

Figure 2.2: Simulation of the electron core formation. The left graph shows the time evolution of the quasi-static laser electric field. The graphs on the right show the particle configuration of 4 different times. As the field increases, more electrons leave the cluster, while the inner electrons form a spherical core. Once the field reaches its maximum value, the trapped (core) electrons reach an equilibrium.

2.2 Electron core oscillations

2.2.1 Uniform cluster

Electrostatic oscillations of the core satisfy the condition $\nabla \cdot \bar{\mathbf{D}} = 0$ for the electric displacement $\bar{\mathbf{D}}$. This condition gives the following equation for the electrostatic potential ϕ:

$$\nabla \cdot \left[\left(\Omega^2 - \omega_p^2(r) \right) \nabla \phi \right] = 0, \tag{2.5}$$

where $\omega_p(r) = \left(4\pi N(r)e^2/m\right)^{1/2}$ is the plasma frequency and Ω is the mode frequency.

For a dipole mode in spherical coordinates, we have

$$\phi = \psi(r)\cos(\theta), \tag{2.6}$$

which reduces Eq. (2.5) to

$$\left[\frac{1}{r^2}\frac{\partial}{\partial r}r^2\left(\Omega^2-\omega_p^2(r)\right)\frac{\partial}{\partial r}-\frac{2}{r^2}\left(\Omega^2-\omega_p^2(r)\right)\right]\psi = 0. \tag{2.7}$$

First, we reproduce the eigenfrequency Ω_0 (Mie frequency [46]) for a uniform cluster. We set $\overline{\omega}_p(r) = \Theta(r-R)\omega_{p0}$, where $\Theta(x)$ is Heaviside step function and we look for a solution in the form

$$\begin{aligned}\psi_0^- &= Ar,\ r<R,\\ \psi_0^+ &= \tfrac{B}{r^2},\ r>R.\end{aligned} \tag{2.8}$$

The matching condition at $r = R$ requires ϕ_0 and $\bar{\mathbf{D}}_r$ to be continuous:

$$\begin{cases} \left.\psi_0^-\right|_{r=R} = \left.\psi_0^+\right|_{r=R}, \\ \left(\Omega_0^2-\omega_{p0}^2\right)\left.\frac{\partial\psi_0^-}{\partial r}\right|_{r=R} = \Omega_0^2\left.\frac{\partial\psi_0^+}{\partial r}\right|_{r=R}. \end{cases} \tag{2.9}$$

The solvability condition for Eq. (2.9) gives the eigenfrequency

$$\Omega_0^2 = \omega_{p0}^2/3. \tag{2.10}$$

Note, that in a uniform cluster the restoring force acting on electrons inside the core is proportional to the core displacement, therefore, Eq. (2.10) holds for finite amplitude oscillations as well.

2.2.2 Nonuniform cluster

If the cluster is slightly nonuniform, then the eigenfrequency Ω would differ from Ω_0 only slightly. In order to find the corresponding correction to Ω_0, we proceed to follow the conventional perturbation theory approach. Eq. (2.5) can be rewritten in the form:

$$\nabla \cdot \left(\left[(\Omega^2 - \Omega_0^2) + (\Omega_0^2 - \overline{\omega}_p^2) + (\overline{\omega}_p^2 - \omega_p^2) \right] \nabla(\phi_0 + \delta\phi) \right) = 0. \tag{2.11}$$

Here $\omega_p = \omega_p(\bar{\mathbf{r}})$ is the perturbed plasma frequency, ϕ_0 is the electrostatic potential in a uniform cluster, so that

$$\nabla \cdot \left[\left(\Omega_0^2 - \overline{\omega}_p^2 \right) \nabla\phi_0 \right] = 0, \tag{2.12}$$

and $\delta\phi$ is the correction to the unperturbed potential due to cluster nonuniformity. We now linearize Eq. (2.11) with respect to small quantities $\Omega^2 - \Omega_0^2$, $\overline{\omega}_p^2 - \omega_p^2$, and $\delta\phi$:

$$\nabla \cdot \left[\left(\Omega^2 - \Omega_0^2 \right) \nabla\phi_0 + \left(\overline{\omega}_p^2 - \omega_p^2 \right) \nabla\phi_0 + \left(\Omega^2 - \omega_p^2 \right) \nabla\delta\phi \right] = 0. \tag{2.13}$$

Next, we multiply both sides of the equation by $-\phi_0$ and integrate by parts.

$$\int \left[\left(\Omega^2 - \Omega_0^2 \right) (\nabla\phi_0)^2 + \left(\overline{\omega}_p^2 - \omega_p^2 \right) (\nabla\phi_0)^2 + \left(\Omega^2 - \omega_p^2 \right) \nabla\phi_0 \nabla\delta\phi \right] dV = 0. \tag{2.14}$$

Here we have used Gauss theorem to eliminate the first term. The last term in the bracket in Eq. (2.14) can be integrated by parts again:

$$\int \left(\Omega^2 - \omega_p^2 \right) \nabla\phi_0 \nabla\delta\phi dV = - \int \delta\phi \nabla \cdot \left[\left(\Omega^2 - \omega_p^2 \right) \nabla\phi_0 \right] dV. \tag{2.15}$$

This expression is of the order of $\delta\phi^2$ and can be neglected. Therefore, Eq. (2.14) reduces to

$$\left(\Omega^2 - \Omega_0^2 \right) \int (\nabla\phi_0)^2 dV + \int \left(\overline{\omega}_p^2 - \omega_p^2(r) \right) (\nabla\phi_0)^2 dV = 0. \tag{2.16}$$

In order to calculate the first integral we multiply Eq. (2.12) by $-\phi_0$ and integrate by parts, which yields the following equation:

$$\Omega_0^2 \int (\nabla\phi_0)^2 dV = \int \overline{\omega}_p^2 (\nabla\phi_0)^2 dV. \tag{2.17}$$

Combining Eq. (2.16) and (2.17) we obtain

$$\frac{\Omega^2 - \Omega_0^2}{\Omega_0^2} = \frac{\int \left(\omega_p^2 - \overline{\omega}_p^2\right) (\nabla\phi_0)^2 dV}{\int \left(\overline{\omega}_p^2\right) (\nabla\phi_0)^2 dV}. \tag{2.18}$$

Since $\nabla\phi_0$ is constant inside the cluster and both $\omega_p(r)$ and $\overline{\omega}_p(r)$ are zero outside of the cluster we cancel $(\nabla\phi_0)^2$ in the numerator and denominator. The final answer for the frequency shift caused by the nonuniformity of the cluster can be written as

$$\frac{\Omega - \Omega_0}{\Omega_0} \approx \frac{1}{2}\frac{\Omega^2 - \Omega_0^2}{\Omega_0^2} = \frac{1}{2}\left\langle \frac{\delta N}{N_0} \right\rangle, \tag{2.19}$$

where δN is the perturbation in plasma density, $\langle\ \rangle$ denotes averaging over the cluster volume.

Simulation of free oscillations

In order to benchmark our code (See Chapter 5), we simulate free oscillations of the electron core with radius $R_e = \frac{3}{7}R$ inside a non-neutral cluster (with ion shell) with radius R. We excite the dipole mode by displacing the core with respect to the equilibrium by $d = \frac{1}{14}R$. We perform simulations for a uniform and nonuniform ion density profiles. In the case of uniform density, the frequency of the oscillations is $\Omega_0 = \omega_{p0}/\sqrt{3}$. In the case of nonuniform density, the frequency of the dipole mode Ω is given by Eq. (2.19). We use a parabolic density profile

$$N(r) = N_0 + \Delta N \frac{r^2}{R^2}, \tag{2.20}$$

with $\Delta N = 0$ and $\Delta N = \pm 0.2 N_0$. The dipole mode frequency shift for convex ($\Delta N = 0.2 N_0$) and concave ($\Delta N = -0.2 N_0$) profiles is then given by

$$\frac{\Delta\Omega}{\Omega_0} = \frac{3}{10}\frac{\Delta N}{N_0}\left(\frac{R_e}{R}\right)^2 = \pm 0.011. \tag{2.21}$$

We perform the simulations for three different profiles for $K \approx 208$ periods of the dipole mode. The frequency resolution is determined by the number of periods: $\delta\Omega/\Omega_0 = 1/K \approx 4.8 \cdot 10^{-3}$. The time step in the simulation is 0.028 of the period of the dipole mode. The numerical frequency drift in leap-frog method is $\delta\Omega_{num}/\Omega_0 = \frac{1}{24}\Omega_0^2 \Delta t^2 = 1.2 \cdot 10^{-3}$, where Δt is the time step (See Chapter 5). The computed spectrum of the cluster dipole moment is shown in Fig. 2.3. The "nonuniform" shift in the frequency of the eigenmode obtained from the simulation agrees with the theoretical predictions. The code has sufficient resolution to reproduce this shift.

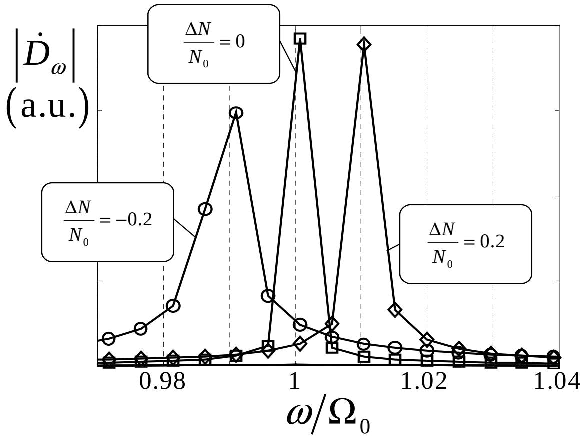

Figure 2.3: Spectra of the free electron core oscillations inside a spherical cluster. The figure shows the Fourier amplitude $|\dot{D}_\omega|$ of the cluster dipole moment in a spherical cluster with a radial density profile given by Eq. (2.20). The curves correspond to concave ($\Delta N = -0.2N_0$), flat ($\Delta N = 0$), and convex ($\Delta N = 0.2N_0$) density profiles.

2.3 Driven core oscillations

In the presence of the laser electric field, driven oscillations will occur at the laser frequency ω_0. The solution far from the cluster must match the external field. Therefore, instead of Eq. (2.8) we have

$$\begin{aligned} \psi_- &= Ar, \qquad\qquad r \le R, \\ \psi_+ &= \tfrac{B}{r^2} - E_{\text{laser}} r,\ r > R, \end{aligned} \tag{2.22}$$

where E_{laser} is the laser field. The matching conditions are

$$\begin{cases} AR = \frac{B}{R^2} - E_{\text{laser}} R, \\ \left(\omega_0^2 - \omega_{p0}^2\right) A = \omega_0^2 \left(-2\frac{B}{R^3} - E_{\text{laser}}\right). \end{cases} \tag{2.23}$$

Together with Eq. (2.6) and Eq. (2.22) they give the following electrostatic potential inside the cluster:

$$\phi_- = \frac{\omega_0^2}{\omega_{p0}^2/3 - \omega_0^2} E_{\text{laser}} r \cos(\theta). \tag{2.24}$$

The corresponding electric field inside the cluster is

$$E_- = -\frac{\omega_0^2}{\omega_{p0}^2/3 - \omega_0^2} E_{\text{laser}}. \tag{2.25}$$

As already noted above, in the case of a uniform cluster, this solution remains valid for finite amplitude oscillations. It follows form Eq. (2.1) and Eq. (2.25) that the equation for the electron core displacement in the oscillatory laser field can be written as

$$m\ddot{\bar{\xi}} = -e\left(\frac{4\pi N e}{3}\bar{\xi} + \bar{\mathbf{E}}_0 \cos(\omega_0 t)\right), \tag{2.26}$$

$$\ddot{\bar{\xi}} + \frac{\omega_{p0}^2}{3}\bar{\xi} = -e\bar{\mathbf{E}}_0 \cos(\omega_0 t). \tag{2.27}$$

The solution to this equation is

$$\bar{\xi} = -\frac{1}{\omega_{p0}^2/3 - \omega_0^2}\frac{e\bar{\mathbf{E}}_0}{m_e}\cos(\omega_0 t), \tag{2.28}$$

The core oscillates at the frequency ω_0, so that its characteristic velocity is $v_{core} = \omega_0 \xi$. The motion of the core is nonrelativistic even for relatively large amplitude pulses with $eE_0/m_e c\omega_0 \sim 1$ as long as $\omega_0 \ll \omega_{p0}$:

$$v_{core} \approx 3c\frac{\omega_0^2}{\omega_{p0}^2}\frac{eE_0}{m_e c\omega_0}. \tag{2.29}$$

Simulation of driven core oscillations in a uniform cluster

We simulate cold electron oscillations inside a uniform spherical cluster in the presence of the external laser field. The laser frequency is much smaller than the plasma frequency (we choose $\omega_0 = \omega_p/6$). The amplitude of the laser field grows linearly to its maximum value ($eE_0/mc\omega_0 = 0.063$) during the first several cycles and then remains constant. The simulation is done for 20 laser periods. The radius of the electron core is smaller than the radius of the ion sphere and the core does not touch the surface of the cluster during the oscillations. The ion density profile is fixed in the simulation. The top graph in Fig. 2.4 shows the position of individual particles after 17 periods. One can see that the electrons preserve the initial spherical shape predicted by the theory [17]. The bottom graph in Fig. 2.4 shows the evolution of the second time derivative $\ddot{D}$ of the cluster dipole moment D. The dashed lines indicate the amplitude of $\ddot{D}$ calculated analytically. The response of the uniform cluster is predominantly at the laser frequency. It also has a small component at $\Omega_0 = \omega_p/\sqrt{3}$, which is excited by the leading edge of the pulse. The time step in this simulation is $\frac{1}{10}$ of the Mie mode period ($2\pi/\Omega_0$); as a result the computed eigenfrequency is 1.4% larger than Ω_0.

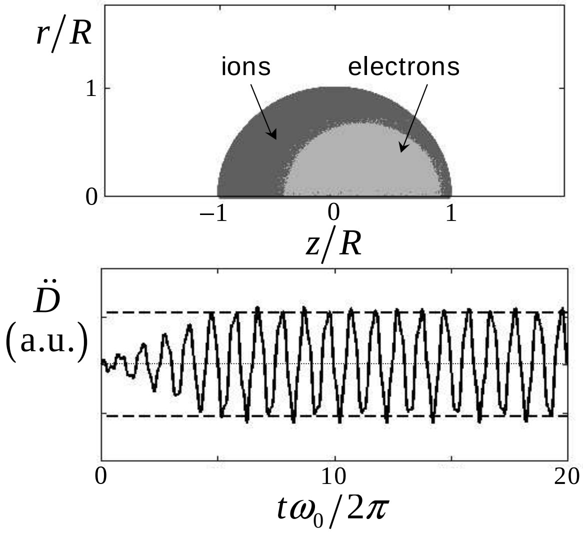

Figure 2.4: Driven core oscillations in a uniform spherical cluster. The top figure shows the cluster configuration after 17 laser periods. The bottom graph shows the time evolution of the second time derivative of the cluster dipole moment.

2.4 Electron heating

If the laser electric field is not strong enough to completely remove the extracted electrons from the cluster, then two electron populations will coexist [17]. Electrons respond differently to the laser field, depending on whether they cross the cluster boundary or stay inside the cluster. The extracted electrons can undergo stochastic heating, whereas the inner (core) electrons remain cold. Collisional heating of the core is usually insignificant on the time scale of the laser pulse [17]. This leads to the formation of a two component electron distribution, as predicted in [17].

The characteristic excursion of an extracted electron in the oscillating laser field $E = E_0 \cos \omega_0 t$ can be estimated as $\zeta = eE_0/m_e\omega_0^2$. In this section we assume that ζ is much smaller than the cluster radius R, so that the extracted electrons are bound to the cluster. We also assume that the the field changes slowly compared to plasma response in the cluster ($\omega_0 \ll \omega_p$, $\omega_p^2 = 4\pi n_0 e^2/m_e$), and that the radius of the cluster is much smaller than the laser wavelength ($R \ll \lambda$).

Initially all electrons are in equilibrium. As the laser field increases, electrons will redistribute themselves in order to compensate the field. This happens almost instantaneously for the core electrons, since $\omega_0 \ll \omega_p$. Therefore the electric field inside the cluster is virtually zero and the electrons inside the cluster follow the electric field quasi-statically.

Those electrons, which cross the cluster boundary will be accelerated by the laser field for half of a period. Since the field amplitude is small, the electron won't travel far from the cluster. As the field changes its sign they will be pushed back into the cluster carrying energy of the order of $\frac{m}{2}\left(\frac{eE}{m\omega_0}\right)^2$.

There is an important difference between the electrons which never left the cluster and those which at least once crossed the boundary of the cluster. The motion of the inside (cold core) electrons is very regular and they are subject only to collisional heating. The motion of the extracted and pulled back electrons is ballistic inside the cluster. As these electrons reach the other side they bounce back from the ion potential, which leads to chaotic motion. If the length of the pulse is larger than the time it takes for a hot electron to cross the cluster the electron can undergo the process of vacuum heating many times, each time randomly changing its momentum by the value of the order of eE_0/ω_0. As hot electrons gain more energy, the condition $\zeta \ll R$ may fail and the electrons may escape. This happens because the potential drops as $1/r$ for a spherical cluster, contrary to in 1D and 2D geometries, where electrons are always bound to the cluster.

In order to model the buildup of the hot electron population, we choose an initially neutral spherical cluster of a radius $R = 40$ nm with an immobile uniform ion background. The laser field is taken to be sub-relativistic with $eE_0/m_e c\omega_0 = 0.025$. The laser wavelength is $\lambda = 0.8\ \mu$. The corresponding excursion of an extracted electron ($\zeta = eE_0/m_e\omega_0^2$) is 10% of the cluster radius. The electric field is oscillatory with amplitude starting from 0 and linearly rising withing 2.5 laser periods to its maximum value and than remaining constant. For an electron with momentum eE/ω_0 it would take about 3 cycles to pass through the cluster across the diameter. We simulate 10 laser cycles in order to observe multiple passes of electrons through the cluster. Many heated electrons pass the cluster along shorter secants and thus are able to undergo the process of vacuum heating many times.

Figure 2.5 shows the time evolution of the electron momentum distribution. The center peak of the distribution corresponds to the cold electron core, the tails correspond to the stochastically heated electrons. Note, that the traditional vacuum heating [47] occurs in a single bounce: an electron is extracted from the surface by the external electric field and then pushed back during the other part of the cycle. The corresponding momentum gain is of the order of eE/ω_0. In a cluster, electrons can undergo this process many times. Indeed, as seen in Fig. 2.5, the maximum normalized electron momentum at $t = 2\tau$ is of the order of $4eE/\omega_0$. This means that some electrons were able to

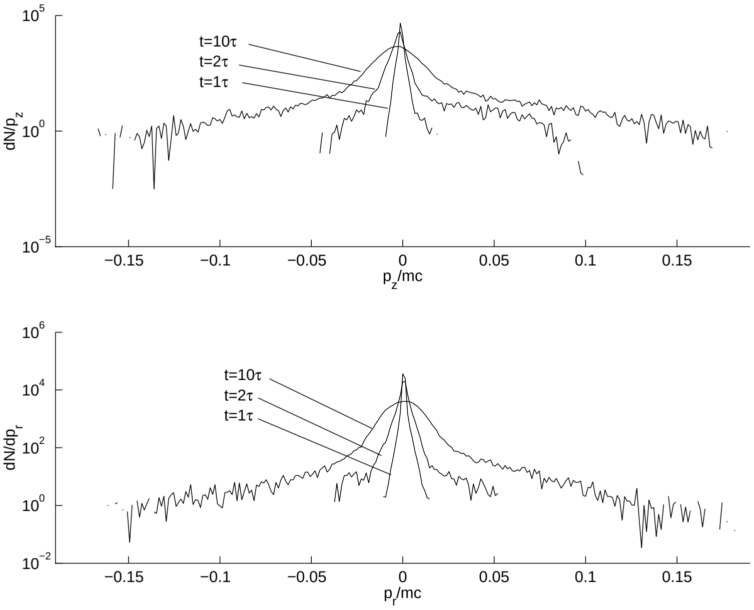

Figure 2.5: Electron momentum distribution

gain energy each semi-period. Another interesting feature is that the electron momentum distribution is anisotropic. For example at $t = 2\tau$ one can clearly see that the momentum distribution along the field is noticeably wider than the distribution perpendicular to the field.

The graph indicates that the central peak also becomes broader with time. Thus broadening is not associated with collisional heating because particle-in-cell code suppresses binary collisions. It turns out that the heating results from numerical noise at the boundary of the electron core.

In order to observe the build up of the two component electron distribution, we keep track of the electrons that travel more than 80% of ζ from the cluster surface at least once. This selects the electrons that gain the largest energy during a laser cycle. The top graph in Fig. 2.6 shows the distribution

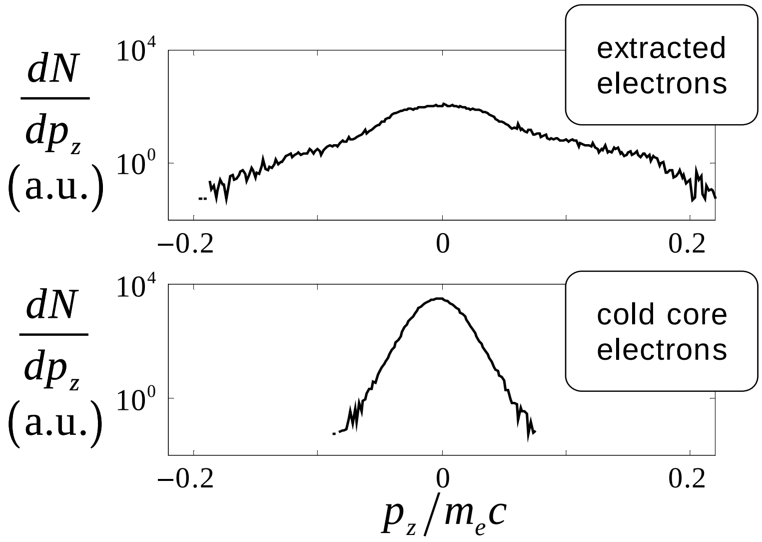

Figure 2.6: The distribution of the extracted electrons (top graph) and the cold core electrons (bottom graph) over axial momentum p_z after 20 laser periods.

of such electrons over axial momentum p_z. The corresponding distribution of the remaining electrons (cold electron core) is shown in the bottom graph of Fig. 2.6. We observe an order of magnitude difference between the temperatures of these two populations after 20 laser periods. As the fast electrons from the narrow edge layer expand, they spread over the entire cluster volume. They, therefore, contribute to the electron density inside the cold core, causing the core to expand. This expansion allows some cold electrons to come close enough to the edge to be extracted by the laser field during its next period. As a result, the number of hot electrons grows in time as shown in Fig. 2.7.

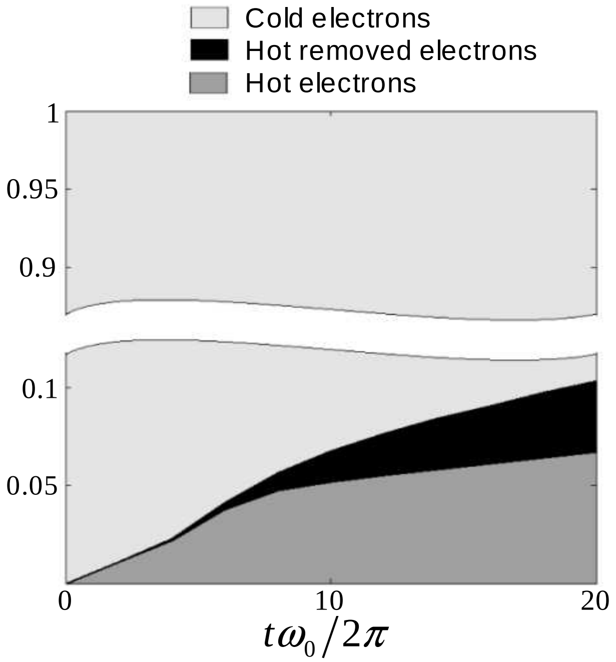

Figure 2.7: Formation of the two component electron distribution. “Cold electrons” are the electrons that never traveled more than 80% of the typical electron excursion ζ from the cluster surface. “Hot electrons” are the electrons which have crossed this boundary at least once. “Hot removed electrons” are hot electrons that reached the boundary of the simulation box and were removed from the simulation. The area plot shows the corresponding fraction for each group of the electrons as a function of time.

Chapter 3

Ion dynamics

3.1 Coulomb and hydrodynamic regimes of explosion

As we saw in Chapter 2, electron distribution during the interaction depends on the amplitude of the laser field and the size of the cluster.

In one limiting case, when the electron excursion is much larger than the cluster radius $\zeta = eE/m\omega_0^2 \gg R$, the extracted electrons leave the cluster and never come back. The confined electrons, if any, form a cold electron core surrounded by an ion shell. This regime corresponds to large laser intensities and small clusters. The ion shell explodes under the Coulomb force of its uncompensated charge. The time scale of the expansion is given by the inverse ion plasma frequency ω_{pi}^{-1}, which is typically comparable to the duration of the laser pulse. In this case, the electron core oscillates in the laser field and the cycle-average electron charge distribution should be used to calculate the force acting on ions.

In the opposite limit when $\zeta \ll R$ a two component electron distribution builds up in the cluster. In this case one can introduce an effective temperature of the hot electron population and calculate the force on the ions as a gradient of the electron thermal pressure. This regime is referred to as hydrodynamic regime. Condition $\zeta \ll R$ corresponds to large clusters or small laser field.

3.2 Anisotropy in cluster explosion

3.2.1 Coulomb regime

Consider a cluster of radius R with an electron core of radius $R_e = R - d$, where d is the amplitude of the core oscillations (see Fig. 3.1). The radial component of the instantaneous electric force acting on an ion at point **A** is given by [48, 49]

$$F_{\perp} = \frac{mR\omega_p^2}{3}\left(1 - \frac{R_e^3}{\left(R^2 + d^2 \sin^2(\omega_0 t)\right)^{3/2}}\right), \tag{3.1}$$

(this force is perpendicular to the laser electric field). The azimuthal force at point **B** is parallel to the laser electric field and is given by

$$F_{||} = |e|E_0^{\text{laser}} \sin(\omega_0 t) + \frac{mR\omega_p^2}{3}\left(1 - \frac{R_e^3/R}{R^2 + d^2 \sin^2(\omega_0 t)}\right). \tag{3.2}$$

To obtain the time averaged forces, we expand Eq. (3.1) and Eq. (3.2) in powers of d/R and average over one laser cycle:

$$\begin{aligned} \left\langle F_{||}\right\rangle &\approx m\omega_p^2 d\left(1 - \tfrac{3}{2}\tfrac{d}{R}\right), \\ \left\langle F_{\perp}\right\rangle &\approx m\omega_p^2 d\left(1 - \tfrac{3}{4}\tfrac{d}{R}\right). \end{aligned} \tag{3.3}$$

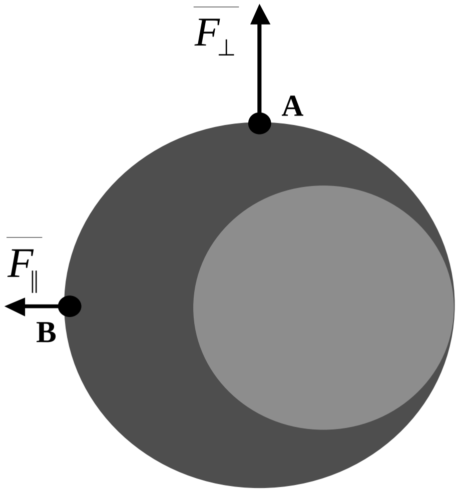

Figure 3.1: Cluster configuration in the Coulomb regime. The core undergoes oscillations at the laser frequency causing anisotropy in the ion expansion causing the force at points **A** and point **B** to be different.

We now abserve that the average force perpendicular to the laser field is larger than that parallel to the field:

$$\langle F_\perp \rangle > \left\langle F_{||} \right\rangle \tag{3.4}$$

The relative anisotropy in given by

$$\frac{\langle F_\perp \rangle - \left\langle F_{||} \right\rangle}{\left\langle F_{||} \right\rangle} \approx \frac{3}{4}\frac{d}{R} = \frac{9}{4}\frac{\omega_0^2}{\omega_p^2}\frac{\zeta}{R} \ll 1 \tag{3.5}$$

One should note, that Eqs. (3.3) were derived for the ions, which are initially at the surface of the cluster. These ions will gain the largest energy during expansion. The relation (3.4) does not hold for all ions. In fact, one can show that for ions, which originally are on the sphere with radius R_e

$$\begin{aligned}\left\langle F_{||} \right\rangle &= \frac{m\omega_p^2}{4}\left(\frac{4d}{\pi} - \frac{d^2}{R_e}\right), \\ \langle F_\perp \rangle &= \frac{m\omega_p^2}{4}\frac{d^2}{R_e}. \end{aligned} \tag{3.6}$$

Therefore, the anisotropy sign will change for the ions with lower energy. It is remarkable, that in this case $\left\langle F_{||}\right\rangle - \langle F_{\perp}\rangle$ is linearly proportional to d.

We performed numerical simulation of the anisotropic cluster expansion in the Coulomb regime. The parameters are chosen such that $d/R = 2/5$ and $\zeta/R = 8$. The ion mass is set to be artificially large, so that the cluster hardly change its shape during the interaction with the laser pulse. Figure 3.2 shows that the extracted electrons are gone and the inside electrons have formed electron core as it should be in the Coulomb regime.

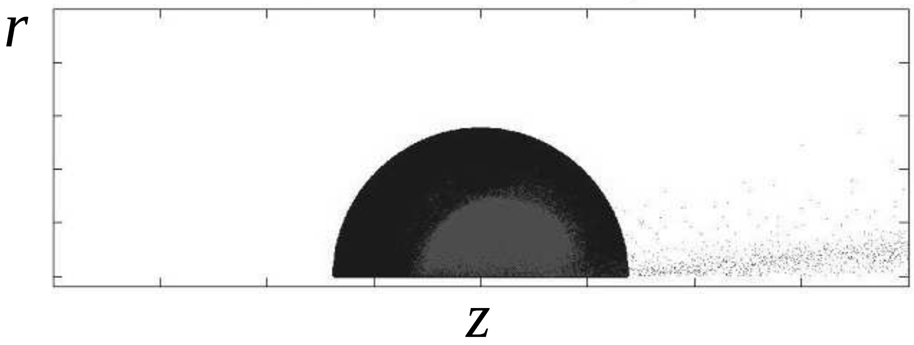

Figure 3.2: Cluster configuration in the Coulomb regime. The outer ion shell expands due to the Coulomb force from its uncompensated charge. The core undergoes oscillations at the laser frequency causing anisotropy in the ion expansion.

Figure 3.3 shows angular anisotropy in the ion momentum for the most energetic ions. The angular dependence of the largest ion momentum is consistent with (3.4).

One should note, that for the realistic ion mass the cluster will expand on faster timescale. One of the consequences will be that the electrons will constantly leak from the core of the cluster. The field created by the escaping electrons may significantly reduce or even reverse the effect described above if

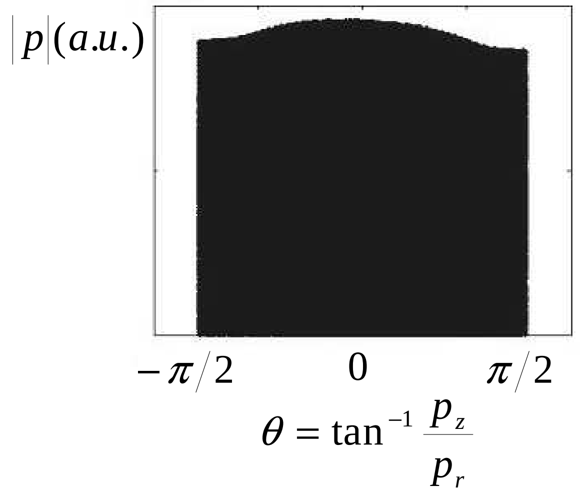

Figure 3.3: The absolute value of the ion momentum as a function of the angle between the ion velocity and the normal plane to the laser electric field.

the electrons leak sufficiently fast.

3.2.2 Hydrodynamic regime

Anisotropy in the hydrodynamic regime is determined by the anisotropy in the electron temperature. As was pointed out in Chapter 2, Sec. 2.4, the electron momentum distribution along the laser field is broader than that perpendicular to the laser electric field. As a result, the ions, which expand along the field will gain more energy than the ions, which expand perpendicular to the laser field.

Figure 3.4 shows cluster configuration in the simulation with $\zeta/R = 1/10$. Figure 3.5 shows that the anisotropy in this regime is significantly larger that in the Coulomb regime and has the opposite sign.

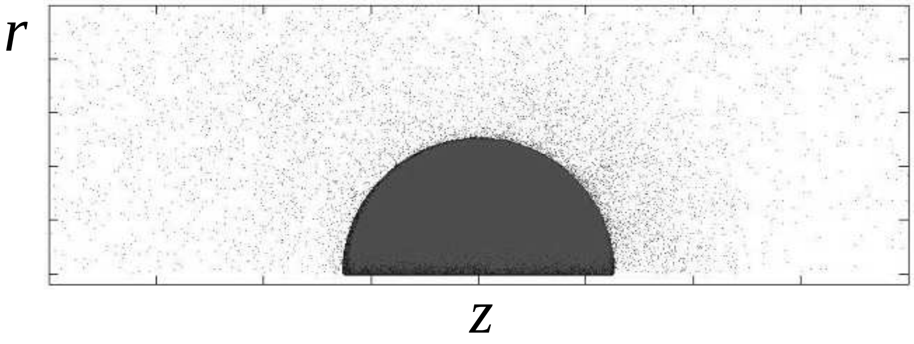

Figure 3.4: Cluster configuration in the hydrodynamic regime after 10 laser periods. Hot electron do not have enough energy to leave the cluster. The ion acceleration is caused by the thermal electron pressure.

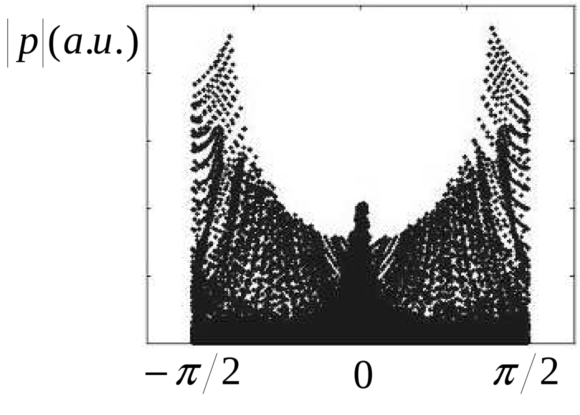

Figure 3.5: The absolute value of the ion momentum as a function of the angle between the ion velocity and the normal plane to the laser electric field.

Chapter 4

Harmonic generation in clusters

4.1 Problem formulation and assumptions

Recent experiments on laser interaction with small clusters reveal an interesting phenomenon of harmonic generation [22, 10]. This effect can serve as a diagnostic tool in cluster experiments. It may also be useful for producing coherent short pulses of soft X-rays. The experiments typically deal with clusters that are smaller in size than both the incident laser wavelength and the radiated wavelength. It is therefore appropriate to treat the harmonic emission as dipole radiation of the cluster. This approach reduces the problem to finding Fourier harmonics of the cluster dipole moment, which is the main technical goal of this chapter.

It is apparent that the cluster response to the laser field has to be nonlinear to produce harmonics. The physics origin of this nonlinearity is the nonlinearity of electron oscillations in the potential well created by the ion background. There are several simplifications that facilitate the corresponding analysis. First, if the laser pulse is not too strong (which we assume to be the case) then the electron motion in the cluster is *nonrelativistic.* It is noteworthy, that the applicability condition for this assumption to a high density cluster is considerably weaker than the corresponding condition in vacuum (see Section 2.1). Second, it is allowable to use *electrostatic approximation* to calculate the electron response. Third, the problem becomes *axisymmetric* when the laser is linearly polarized.

Yet another important aspect of the problem is that the electron response can be strongly enhanced by collective effects when the harmonic frequency resonates with a linear eigenmode in the cluster. The mode of primary interest is the Mie dipole mode [46, 16]. The corresponding eigenfrequency for a nearly uniform cluster is $\omega_p/\sqrt{3}$, where ω_p is the electron plasma frequency.

Making use of the features described above, we develop an analytical model and a numerical code to calculate nonlinear electron response induced in the cluster by the laser pulse. The code allows us to go beyond the technical limitations of the analytical theory. In particular, the theory is restricted to the case of only slightly nonuniform cluster with a fixed ion density profile, whereas the code is free from this constraint, which enables it to simulate self-consistently the resonant enhancement of harmonic generation during cluster expansion. In addition, the code takes account of hot electrons that undergo "vacuum heating" at the cluster boundary. This will enable us to compare the relative roles of the hot electron population and the cold electron core.

Nonlinear excitation of the Mie resonance has recently been discussed in Refs. [50, 51, 52] in relation to harmonic generation in clusters. Although the model developed in these references has the same basic ingredients as our theory (collective eigenmode and nonlinear coupling), the actual cause of the nonlinear response and the rigorousness of its analysis are different. Reference [51] deals with a single-fluid model for heated electrons in a spatially uniform spherical ion background. The authors assume that the electron cloud oscillates as a rigid body in step with the applied field and that certain part of the electron cloud crosses the ion boundary. Within this model, the effect of the sharp edge in ion density is crucial. The resulting nonlinear force is proportional to the gradient of the electron density at the edge of the ion sphere. The problem with this model is that the rigid displacement approximation fails for the edge electrons, which invalidates the perturbative approach used in Refs. [50, 51, 52].

As shown in Ref. [17], there are two electron populations in the cluster, the cold core and the heated halo, and they respond differently to the applied laser field. In an equilibrium state, the radius of the cold electron core is smaller than that of the ion-cluster. As long as the core is inside the ion sphere, it moves coherently in response to the laser-field. In Sec. 4.3 we will show that the core motion can be described by rigid displacement as long as the cluster non-uniformity is small. Although this may resemble the rigid displacement approximation from Ref. [50], the fact that we consider only those core electrons that do not touch the edge makes a big difference and allows us to derive an accurate analytical expression for their nonlinear response. In contrast with the core electrons, the halo electrons move chaotically. The chaotic electron halo that crosses the ion boundary can contribute to harmonic generation. However, this contribution cannot be described in terms of rigid coherent displacement.

Based on the two-component electron picture, we will demonstrate that the cold electron core plays the dominant role in harmonic generation, provided that the ion density profile inside the cluster is nonuniform. A natural reason for this nonuniformity is the ion motion during cluster expansion.

In what follows, we will limit our analysis to the case of a single cluster. By doing so, we will demonstrate the basic mechanism of harmonic generation with particular attention to the third harmonic. However, our results will not be quite ready for quantitative comparison with experimental data since the experiments typically deal with many clusters. One would therefore need to take into account that the measured signal involves averaging over the cluster distribution and the laser beam profile. Also, interference effects need to be considered to properly interpret the data. These two aspects go beyond the scope of the present work.

4.2 Nonlinearities in clusters

There are two factors that lead to the nonlinearity of the electron core response. First, relativistic motion is nonlinear. The small dimensionless parameter describing this nonlinearity is v_{core}/c. Second, nonuniformity of the cluster density makes the oscillations nonlinear. The corresponding small dimensionless parameter is $\frac{\delta n}{n_0}\frac{d}{R}$, where d/R is the ratio of the core displacement to the cluster radius and $\delta n/n_0$ is the relative nonuniformity of the ion density. In order to understand the relative role of the two factors leading to the nonlinearity, we estimate the ratio of the small parameters involved:

$$\frac{v_{core}/c}{\delta n/n_0 \cdot d/R} = 2\pi \frac{R n_0}{\lambda \delta n}. \tag{4.1}$$

Since the laser wavelength is much larger than the cluster radius (the ratio λ/R is about 10^2 in experiments described in Ref. [10]), we conclude that a small density perturbation in the cluster can easily be the main reason for nonlinearity of the core response.

In addition to the core electrons, there are some electrons which are extracted from the cluster and accelerated by the external field. The behavior of these electrons depends on the amplitude of the laser field. In the strong field limit, when the characteristic excursion of an extracted electron $\zeta = eE_0/m_e\omega_0^2$ is much larger than the cluster radius R, these electrons are not trapped in the cluster potential and they leave the cluster. In the opposite case of $\zeta \ll R$, the extracted electrons return to the cluster as the external field changes sign. As these electrons bounce back and forth, they continuously gain energy due to so-called vacuum heating [47] or surface heating [16]. As a result, a two-component electron distribution arises in the cluster [17]. Of these two, it is the cold component that produces the most of the coherent nonlinear response.

4.3 Analytical treatment of harmonic generation

The aim of this section is to describe analytically how the laser field produces a strong response of the cluster at the third harmonic of the laser frequency. This effect is very similar to the response of a weakly nonlinear oscillator that is driven by a sinusoidal force, $f \sin \omega_0 t$, where ω_0 is close to $\frac{1}{3}$ of the oscillator eigenfrequency Ω. The corresponding equation of motion for the oscillator has the form:

$$\frac{d^2x}{dt^2} + \Omega^2 x = \alpha x^3 + f \sin \omega_0 t, \tag{4.2}$$

where the coefficient α characterizes the nonlinearity. To lowest order in f, the driving force produces a linear response:

$$x = \frac{f}{\Omega^2 - \omega_0^2} \sin \omega_0 t. \tag{4.3}$$

The resulting nonlinear force αx^3 contains a spectral component at $3\omega_0$. This component can generate a strong resonance response when $3\omega_0$ is close to Ω.

In order to link the cluster problem to the oscillator problem, we use a Lagrangian for the cluster electrons in the presence of immobile ions,

$$\begin{aligned} L = {} & \frac{m_e}{2} \int d^3\bar{\mathbf{r}} n(\mathbf{r}) \left(\frac{\partial \xi_i}{\partial t} \right)^2 - \frac{e^2}{2} \int d^3\mathbf{r} d^3\mathbf{r}_1 n(\mathbf{r}) n(\mathbf{r}_1) \left(\frac{1}{|\mathbf{r} + \xi(\mathbf{r};t) - \mathbf{r}_1 - \xi(\mathbf{r}_1;t)|} - \frac{1}{|\mathbf{r} - \mathbf{r}_1|} \right) \\ & + e^2 \int d^3\mathbf{r} d^3\mathbf{r}_1 n(\mathbf{r}) N(\mathbf{r}_1) \left(\frac{1}{|\mathbf{r} + \xi(\mathbf{r};t) - \mathbf{r}_1|} - \frac{1}{|\mathbf{r} - \mathbf{r}_1|} \right) + e \int d^3\mathbf{r} n(\mathbf{r}) E_i(t) \xi_i(\mathbf{r};t). \end{aligned} \tag{4.4}$$

The dynamical variable in this Lagrangian is the electron displacement vector $\xi_i(\mathbf{r};t)$, where $\mathbf{r}$ is the particle equilibrium position, and the subscript i for ξ denotes the corresponding Cartesian component. The functions $n(\mathbf{r})$ and $N(\mathbf{r})$ are the unperturbed densities of electrons and ions in the absence of the laser electric field $E_i(t)$. The individual terms in the Lagrangian represent the electron kinetic energy, the electron-electron Coulomb energy, the electron-ion Coulomb energy, and the electron interaction with the laser electric field (this field is time-dependent, but spatially uniform within the cluster). It is apparent that $n(\mathbf{r})$ and $N(\mathbf{r})$ are equal within the cold electron core. We will assume that the ion density profile extends beyond the electron core, so that there is a positive ion shell around the neutralized core (see Fig. 2.1). We will also assume that the electron displacement is smaller than the shell thickness Δ, so that all electrons remain inside the potential well in their oscillatory motion. This requires the laser electric field to be smaller than:

$E_0 \ll (\omega_p^2/3 - \omega_0^2) m_e \Delta/e$ [see Eq. (2.28)] .

In order to make the problem tractable analytically, we will introduce an additional assumption that $N(\mathbf{r})$ is nearly flat within a spherical boundary. Yet, we will retain a small deviation from a purely flat ion profile, which turns out to be essential for harmonic generation.

We now expand the Lagrangian in powers of $\xi_i(\mathbf{r};t)$ up to fourth-order terms. For brevity we suppress $\mathbf{r}$ and t in the arguments of displacement, but we keep $\mathbf{r_1}$ in the argument. This expansion starts from quadratic terms since the linear term vanishes due to the requirement that $\xi_i(\mathbf{r};t) = 0$ represents electron equilibrium. We then find that

$$\begin{aligned}
L = {} & \frac{m_e}{2}\int d^3\mathbf{r}\, n(\mathbf{r}) \left(\frac{\partial \xi_i}{\partial t}\right)^2 - \frac{e^2}{4}\int d^3\mathbf{r} d^3\mathbf{r}_1 n(\mathbf{r}) n(\mathbf{r}_1) \left[\xi_i - \xi_i(\mathbf{r}_1)\right]\left[\xi_k - \xi_k(\mathbf{r}_1)\right] \frac{\partial^2}{\partial x_i \partial x_k}\frac{1}{|\mathbf{r}-\mathbf{r}_1|} \\
& - \frac{e^2}{12}\int d^3\mathbf{r} d^3\mathbf{r}_1 n(\mathbf{r}) n(\mathbf{r}_1) \left[\xi_i - \xi_i(\mathbf{r_1})\right]\left[\xi_k - \xi_k(\mathbf{r}_1)\right]\left[\xi_l - \xi_l(\mathbf{r}_1)\right] \frac{\partial^3}{\partial x_i \partial x_k \partial x_l}\frac{1}{|\mathbf{r}-\mathbf{r}_1|} \\
& - \frac{e^2}{48}\int d^3\mathbf{r} d^3\mathbf{r}_1 n(\mathbf{r}) n(\mathbf{r}_1) \left[\xi_i - \xi_i(\mathbf{r}_1)\right]\left[\xi_k - \xi_k(\mathbf{r}_1)\right] \\
& \times \left[\xi_l - \xi_l(\mathbf{r}_1)\right]\left[\xi_m - \xi_m(\mathbf{r}_1)\right] \frac{\partial^4}{\partial x_i \partial x_k \partial x_l \partial x_m}\frac{1}{|\mathbf{r}-\mathbf{r}_1|} \\
& + \frac{e^2}{2}\int d^3\mathbf{r} d^3\mathbf{r_1} n(\mathbf{r}) N(\mathbf{r_1}) \xi_i \xi_k \frac{\partial^2}{\partial x_i \partial x_k}\frac{1}{|\mathbf{r}-\mathbf{r_1}|} \\
& + \frac{e^2}{6}\int d^3\mathbf{r} d^3\mathbf{r_1} n(\mathbf{r}) N(\mathbf{r_1}) \xi_i \xi_k \xi_l \frac{\partial^3}{\partial x_i \partial x_k \partial x_l}\frac{1}{|\mathbf{r}-\mathbf{r_1}|} \\
& + \frac{e^2}{24}\int d^3\mathbf{r} d^3\mathbf{r}_1 n(\mathbf{r}) N(\mathbf{r}_1) \xi_i \xi_k \xi_l \xi_m \frac{\partial^4}{\partial x_i \partial x_k \partial x_l \partial x_m}\frac{1}{|\mathbf{r}-\mathbf{r}_1|} \\
& + e\int d^3\mathbf{r}\, n(\mathbf{r}) E_i(t) \xi_i .
\end{aligned} \tag{4.5}$$

The quadratic parts of the electron-electron and electron-ion Coulomb energies can be conveniently combined into a single term, which gives

$$L = \frac{m_e}{2}\int d^3\mathbf{r}\, n(\mathbf{r}) \left(\frac{\partial \xi_i}{\partial t}\right)^2 + \frac{e^2}{2}\int d^3\mathbf{r} d^3\mathbf{r_1} n(\mathbf{r}) n(\mathbf{r}_1) \xi_i \xi_k(\mathbf{r}_1) \frac{\partial^2}{\partial x_i \partial x_k}\frac{1}{|\mathbf{r}-\mathbf{r}_1|}$$

$$
\begin{aligned}
&-\frac{e^2}{12}\int d^3\mathbf{r}d^3\mathbf{r}_1 n(\mathbf{r})n(\mathbf{r}_1)\left[\xi_i-\xi_i(\mathbf{r}_1)\right]\left[\xi_k-\xi_k(\mathbf{r}_1)\right]\left[\xi_l-\xi_l(\mathbf{r}_1)\right]\frac{\partial^3}{\partial x_i\partial x_k\partial x_l}\frac{1}{|\mathbf{r}-\mathbf{r}_1|}\\
&-\frac{e^2}{48}\int d^3\mathbf{r}d^3\mathbf{r}_1 n(\mathbf{r})n(\mathbf{r}_1)\left[\xi_i-\xi_i(\mathbf{r}_1)\right]\left[\xi_k-\xi_k(\mathbf{r_1})\right]\\
&\times\left[\xi_l-\xi_l(\mathbf{r_1})\right]\left[\xi_m-\xi_m(\mathbf{r_1})\right]\frac{\partial^4}{\partial x_i\partial x_k\partial x_l\partial x_m}\frac{1}{|\mathbf{r}-\mathbf{r}_1|}\\
&+\frac{e^2}{6}\int d^3\mathbf{r}d^3\mathbf{r_1}n(\mathbf{r})N(\mathbf{r_1})\xi_i\xi_k\xi_l\frac{\partial^3}{\partial x_i\partial x_k\partial x_l}\frac{1}{|\mathbf{r}-\mathbf{r_1}|}\\
&+\frac{e^2}{24}\int d^3\mathbf{r}d^3\mathbf{r_1}n(\mathbf{r})N(\mathbf{r_1})\xi_i\xi_k\xi_l\xi_m\frac{\partial^4}{\partial x_i\partial x_k\partial x_l\partial x_m}\frac{1}{|\mathbf{r}-\mathbf{r_1}|}\\
&+e\int d^3\mathbf{r}n(\mathbf{r})E_i(t)\xi_i. \qquad (4.6)
\end{aligned}
$$

The transformation of Eq. (4.5) into Eq. (4.6) involves the observation, that the quantity

$$\int\left[n(\mathbf{r}_1)-N(\mathbf{r}_1)\right]\frac{d^3\mathbf{r}_1}{|\mathbf{r}-\mathbf{r}_1|} \qquad (4.7)$$

is constant within the electron core, because this quantity represents the equilibrium electrostatic potential created by the ion shell in the core.

It is noteworthy that the electron-ion terms in Eq. (4.6) vanish in the case of a uniform spherical ion background. Indeed, for $N(\mathbf{r})=\text{const}$, integration over $\mathbf{r_1}$ gives

$$\int\frac{N(\mathbf{r}_1)d^3\mathbf{r}_1}{|\mathbf{r}-\mathbf{r_1}|}=-\frac{4\pi}{6}Nr^2+\frac{4\pi}{2}NR^2, \qquad (4.8)$$

where R is the cluster radius. The third and the fourth derivatives of this expression equal zero, which eliminates the corresponding electron-ion terms for $N(\mathbf{r})=\text{const}$. We also observe that the third- and the fourth order electron terms in the Lagrangian vanish if we consider a rigid displacement of the electron core. The underlying physics is that rigid displacement of all electrons does not affect their mutual potential energy. As a result, the rigid displacement is an exact solution of the equations of motion for a uniform spherical cluster in the presence of a sinusoidal driving field. These observations suggest that a displacement $\xi_i(\mathbf{r};t)$ with a weak spatial dependence is a relevant candidate solution for a slightly nonuniform and/or non-spherical cluster. The spatial variation in such a solution would scale linearly with the small nonuniform part of $N(\mathbf{r})$. This allows us to neglect the third- and fourth order electron-electron interaction terms in Eq. (4.6) compared to the corresponding electron-ion terms, which simplifies the Lagrangian to

$$\begin{aligned}
L = \frac{m_e}{2}\int d^3\mathbf{r}n(\mathbf{r})\left(\frac{\partial\xi_i}{\partial t}\right)^2 + \frac{e^2}{2}\int d^3\mathbf{r}d^3\mathbf{r_1}n(\mathbf{r})n(\mathbf{r_1})\xi_i\xi_k(\mathbf{r_1})\frac{\partial^2}{\partial x_i\partial x_k}\frac{1}{|\mathbf{r}-\mathbf{r_1}|}\\
+\frac{e^2}{6}\int d^3\mathbf{r}d^3\mathbf{r_1}n(\mathbf{r})N(\mathbf{r_1})\xi_i\xi_k\xi_l\frac{\partial^3}{\partial x_i\partial x_k\partial x_l}\frac{1}{|\mathbf{r}-\mathbf{r_1}|}\\
+\frac{e^2}{24}\int d^3\mathbf{r}d^3\mathbf{r_1}n(\mathbf{r})N(\mathbf{r_1})\xi_i\xi_k\xi_l\xi_m\frac{\partial^4}{\partial x_i\partial x_k\partial x_l\partial x_m}\frac{1}{|\mathbf{r}-\mathbf{r_1}|}\\
+e\int d^3\mathbf{r}n(\mathbf{r})E_i(t)\xi_i, \qquad (4.9)
\end{aligned}$$

and gives the following Euler-Lagrange equation:

$$\begin{aligned}
m_e\frac{\partial^2\xi_i(\mathbf{r};t)}{\partial t^2} - e^2\int d^3\mathbf{r_1}n(\mathbf{r_1})\xi_k(\mathbf{r_1};t)\frac{\partial^2}{\partial x_i\partial x_k}\frac{1}{|\mathbf{r}-\mathbf{r_1}|}\\
-\frac{e^2}{2}\xi_k(\mathbf{r};t)\xi_l(\mathbf{r};t)\int d^3\mathbf{r_1}N(\mathbf{r_1})\frac{\partial^3}{\partial x_i\partial x_k\partial x_l}\frac{1}{|\mathbf{r}-\mathbf{r_1}|} \qquad (4.10)\\
-\frac{e^2}{6}\xi_k(\mathbf{r};t)\xi_l(\mathbf{r};t)\xi_m(\mathbf{r};t)\int d^3\mathbf{r_1}N(\mathbf{r_1})\frac{\partial^4}{\partial x_i\partial x_k\partial x_l\partial x_m}\frac{1}{|\mathbf{r}-\mathbf{r_1}|} - eE_i(t) = 0.
\end{aligned}$$

Here the space-time dependance of ξ is now explicitly displayed.

Assuming that the laser electric field is monochromatic and linearly polarized, we set

$$E_i(t) = \frac{\epsilon_i}{2}\left[E_0\exp(-i\omega_0 t) + \text{c.c. }\right], \qquad (4.11)$$

where ϵ_i is the unit polarization vector and E_0 is the field amplitude, and we seek ξ_i in the form:

$$\xi_i = \xi_{(0)i} + \frac{1}{2}\left[\xi_{(1)i}\exp(-i\omega_0 t) + \xi_{(2)i}\exp(-2i\omega_0 t) + \xi_{(3)i}\exp(-3i\omega_0 t) + \text{c.c.}\right] + \cdots . \tag{4.12}$$

This representation leads to a truncated set of equations for the Fourier amplitudes of the displacement. In particular, to the leading order the third harmonic equation has the form:

$$\begin{aligned}
&9m_e\omega_0^2\xi_{(3)i}(\mathbf{r}) + e^2\int d^3\mathbf{r_1} n(\mathbf{r_1})\xi_{(3)k}(\mathbf{r_1})\frac{\partial^2}{\partial x_i\partial x_k}\frac{1}{|\mathbf{r}-\mathbf{r_1}|}\\
&+\frac{e^2}{4}\left[\xi_{(2)k}(\mathbf{r})\xi_{(1)l}(\mathbf{r}) + \xi_{(1)k}(\mathbf{r})\xi_{(2)l}(\mathbf{r})\right]\int d^3\mathbf{r_1}N(\mathbf{r_1})\frac{\partial^3}{\partial x_i\partial x_k\partial x_l}\frac{1}{|\mathbf{r}-\mathbf{r_1}|}\\
&+\frac{e^2}{24}\xi_{(1)k}(\mathbf{r})\xi_{(1)l}(\mathbf{r})\xi_{(1)m}(\mathbf{r})\int d^3\mathbf{r_1}N(\mathbf{r_1})\frac{\partial^4}{\partial x_i\partial x_k\partial x_l\partial x_m}\frac{1}{|\mathbf{r}-\mathbf{r_1}|} = 0.
\end{aligned} \tag{4.13}$$

Calculation of the nonlinear force in Eq. (4.13) involves equations for the second and first harmonics:

$$\begin{aligned}
4m_e\omega_0^2\xi_{(2)i}(\mathbf{r}) + e^2\int d^3\mathbf{r_1} n(\mathbf{r_1})\xi_{(2)k}(\mathbf{r_1})\frac{\partial^2}{\partial x_i\partial x_k}\frac{1}{|\mathbf{r}-\mathbf{r_1}|}&\\
+\frac{e^2}{4}\xi_{(1)k}(\mathbf{r})\xi_{(1)l}(\mathbf{r})\int d^3\mathbf{r_1}N(\mathbf{r_1})\frac{\partial^3}{\partial x_i\partial x_k\partial x_l}\frac{1}{|\mathbf{r}-\mathbf{r_1}|} &= 0, \quad (4.14)\\
m_e\omega_0^2\xi_{(1)i}(\mathbf{r}) + e^2\int d^3\mathbf{r_1} n(\mathbf{r_1})\xi_{(1)k}(\mathbf{r_1})\frac{\partial^2}{\partial x_i\partial x_k}\frac{1}{|\mathbf{r}-\mathbf{r_1}|} + eE_0\epsilon_i &= 0. \quad (4.15)
\end{aligned}$$

It is apparent that $\xi_{(1)i}$ scales linearly with the laser field amplitude E_0 and that $\xi_{(2)i}$ scales as E_0^2. Therefore, both nonlinear terms in Eq. (4.13) scale as E_0^3. Yet, in the case of nearly flat ion density profile, the first of the two nonlinear terms in Eq. (4.13) is much smaller than the second one. The reason is that $\int d^3\mathbf{r_1}N(\mathbf{r_1})\frac{\partial^3}{\partial x_i\partial x_k\partial x_l}\frac{1}{|\mathbf{r}-\mathbf{r_1}|}$ vanishes for a uniform spherical cluster. Therefore, $\xi_{(2)i}$ is proportional to the deviation δN from the uniform ion density. As a result, the first nonlinear term in Eq. (4.13) is proportional to the square of δN, whereas the second term is linear in δN.

Equation (4.13) involves a self-adjoint linear operator $\widehat{L}$ defined by:

$$\widehat{L}_{ik}\xi_{(3)k} \equiv -\frac{e^2}{m_e}\int d^3\mathbf{r_1} n(\mathbf{r_1})\xi_{(3)k}(\mathbf{r_1})\frac{\partial^2}{\partial x_i \partial x_k}\frac{1}{|\mathbf{r}-\mathbf{r_1}|}. \tag{4.16}$$

Let Ω^2 be an eigenvalue of this operator and η_i be the corresponding eigenvector, so that

$$\widehat{L}_{ik}\eta_k \equiv -\frac{e^2}{m_e}\int d^3\mathbf{r_1} n(\mathbf{r_1})\eta_k(\mathbf{r_1})\frac{\partial^2}{\partial x_i \partial x_k}\frac{1}{|\mathbf{r}-\mathbf{r_1}|} = \Omega^2\eta_i, \tag{4.17}$$

with a normalization condition,

$$\int n(\mathbf{r})\eta_i^*(\mathbf{r})\eta_i(\mathbf{r})d^3\mathbf{r} = 1. \tag{4.18}$$

We can then rewrite Eq. (4.13) in the form

$$\begin{aligned} &m_e\left(9\omega_0^2-\Omega^2\right)\xi_{(3)i}(\mathbf{r}) + m_e\left(\Omega^2\delta_{ik}-\widehat{L}_{ik}\right)\xi_{(3)k}(\mathbf{r}) \\ &+\frac{e^2}{24}\xi_{(1)k}(\mathbf{r})\xi_{(1)l}(\mathbf{r})\xi_{(1)m}(\mathbf{r})\int d^3\mathbf{r_1} N(\mathbf{r_1})\frac{\partial^4}{\partial x_i\partial x_k\partial x_l\partial x_m}\frac{1}{|\mathbf{r}-\mathbf{r_1}|} = 0. \end{aligned} \tag{4.19}$$

If $9\omega_0^2$ is close to Ω^2 and the nonlinear force is sufficiently small, then equation Eq. (4.19) implies that $m_e(\Omega^2\delta_{ik}-\widehat{L}_{ik})\xi_{(3)k}(\mathbf{r}) \approx 0$. In other words, $\xi_{(3)i}(\mathbf{r})$ must be an eigenvector of the operator $\widehat{L}$ up to an overall multiplicative factor, i.e. $\xi_{(3)i}(\mathbf{r}) \approx C\eta_i$ with C a constant. In order to find the constant C, we multiply Eq. (4.19) by $n(\mathbf{r})\eta_i^*(\mathbf{r})$ and integrate the result over the volume. Since $\widehat{L}$ is a self-adjoint operator, this procedure annihilates the term involving $(\Omega^2\delta_{ik}-\widehat{L}_{ik})$. Solving for C gives

$$\begin{aligned} C = \; &-\frac{e^2}{24m_e\left(9\omega_0^2-\Omega^2\right)}\int d^3\mathbf{r} n(\mathbf{r})\eta_i^*(\mathbf{r})\xi_{(1)k}(\mathbf{r})\xi_{(1)l}(\mathbf{r})\xi_{(1)m}(\mathbf{r}) \\ &\times\int d^3\mathbf{r_1} N(\mathbf{r_1})\frac{\partial^4}{\partial x_i\partial x_k\partial x_l\partial x_m}\frac{1}{|\mathbf{r}-\mathbf{r_1}|}. \end{aligned} \tag{4.20}$$

As already noted, only the deviation δN from the uniform density profile contributes to the inner integral in Eq. (4.20), which allows us to disregard small non-uniformity in the quantity $n(\mathbf{r})\eta_i^*(\mathbf{r})\xi_{(1)k}(\mathbf{r})\xi_{(1)l}(\mathbf{r})\xi_{(1)m}(\mathbf{r})$ within the cold electron core and treat this quantity as a constant. We then obtain

$$C = -\frac{e^2 n \eta_i^* \xi_{(1)k}\xi_{(1)l}\xi_{(1)m}}{24 m_e\left(9\omega_0^2 - \Omega^2\right)} \int d^3\mathbf{r} \int d^3\mathbf{r_1} \delta N(\mathbf{r_1}) \frac{\partial^4}{\partial x_i \partial x_k \partial x_l \partial x_m} \frac{1}{|\mathbf{r} - \mathbf{r_1}|}, \quad (4.21)$$

where $\xi_{(1)i}$ is related to the laser electric field by Eq. (4.15),

$$\xi_{(1)i} = -\frac{eE_0\epsilon_i}{m_e(\omega_0^2 - \Omega^2)}, \quad (4.22)$$

and the outer integration needs to be performed over the spherical volume of the electron core.

It is apparent that, for the nearly spherical cluster, η_i has to be parallel to the laser electric field, as the direction of this field is the only preferred direction in the problem. We denote this direction with a subscript s. Equations (4.21) and (4.22) together with the definition of $\xi_{(3)i}$ and the normalization condition of Eq. (4.18) lead to

$$D_{(3)s} = -e \int d^3\mathbf{r} n \xi_{(3)s} = \frac{n e^3 \epsilon_s}{24 m_e\left(9\omega_0^2 - \Omega^2\right)} \left[\frac{eE_0}{m_e(\omega_0^2 - \Omega^2)}\right]^3$$

$$\times \int d^3\mathbf{r} \int d^3\mathbf{r_1} N(\mathbf{r_1}) \epsilon_i \epsilon_k \epsilon_l \epsilon_m \frac{\partial^4}{\partial x_i \partial x_k \partial x_l \partial x_m} \frac{1}{|\mathbf{r} - \mathbf{r_1}|}. \quad (4.23)$$

In order to evaluate the integral on the right-hand side of this expression, we use a Legendre polynomial expansion for $N(\mathbf{r_1})$ in angular variable:

$$N(\mathbf{r_1}) = \sum_{l=0}^{\infty} N_l(r_1) P_l(\cos\theta_1), \quad (4.24)$$

where θ_1 is the angle between the vectors $\mathbf{r_1}$ and ϵ_i. We find that only N_0, N_2, and N_4 contribute to the integral, and the result of the integration is

$$\int d^3\mathbf{r} \int d^3\mathbf{r_1} N(\mathbf{r_1}) \epsilon_i \epsilon_k \epsilon_l \epsilon_m \frac{\partial^4}{\partial x_i \partial x_k \partial x_l \partial x_m} \frac{1}{|\mathbf{r} - \mathbf{r_1}|} \quad (4.25)$$

$$= -\frac{16\pi^2}{5}\left[r^2\frac{\partial N_0}{\partial r} + \frac{4}{7r}\frac{\partial}{\partial r}\left(r^3 N_2\right) - \frac{8}{63r}\frac{\partial}{\partial r}\left(\frac{1}{r}\frac{\partial}{\partial r}r^7\int_r^\infty dr\frac{N_4}{r^3}\right)\right]_{r=R_e},$$

where R_e is the radius of the cold electron core.

The total power radiated by an oscillating dipole with the amplitude defined by Eq. (4.23) is given by:

$$\begin{aligned} P = \; & \frac{e^2\omega_p^4}{3c^3}\left[\frac{3\pi}{10}\frac{\omega_0^2}{(9\omega_0^2-\Omega^2)}\frac{e^3E_0^3}{m_e^3R_e^3\left(\omega_0^2-\Omega^2\right)^3}\right]^2 \\ & \times\left[r^5\frac{\partial N_0}{\partial r} + \frac{4r^2}{7}\frac{\partial}{\partial r}\left(r^3N_2\right) - \frac{8r^2}{63}\frac{\partial}{\partial r}\left(\frac{1}{r}\frac{\partial}{\partial r}r^7\int_r^\infty dr\frac{N_4}{r^3}\right)\right]^2_{r=R_e}. \end{aligned} \tag{4.26}$$

4.4 Nonlinear response of the cold electron core (simulation results)

4.4.1 Cluster with a fixed ion density profile

This section addresses the case in which the excursion of the extracted electrons is much larger than the cluster radius. In this regime, most of the extracted electrons escape from the cluster and never come back. As a result, the cluster contains only cold electrons that are trapped inside the electrostatic potential well and respond to the laser field adiabatically.

In order to simulate the response of the confined electrons only, we choose an initially spherical cluster in which the radius of the cold electron core is less than the radius of the ion sphere, so that the core is surrounded by a positively charged ion shell. Such a configuration can be created by a very short pump laser pulse that removes the edge electrons before a lower amplitude probe pulse arrives. Starting from this configuration, we simulate the cluster response to the probe pulse.

We first present simulation results for the case of immobile ions with a radial density profile given by Eq. (2.20), with $\Delta N/N_0 = -0.2$. The laser pulse is 60 periods long. The amplitude of the laser field rises from zero to its maximum value during the first 6 periods and then remains constant. We perform simulations with different amplitudes and frequencies of the laser field in order to compare the frequency and amplitude scalings of the cluster response, which may be evaluated by Eq. (4.23) using the ion profile of Eq. (2.20). The expression obtained may be rewritten in the following normalized form:

$$\frac{D_{(3)s}}{Q_e R_e} = 0.062 \frac{\Delta N}{N_0} \frac{R}{R_e} \left(\frac{c}{\omega_{p0} R} \right)^3 \left(\frac{eE_0}{m_e c \omega_0} \right)^3 \frac{\omega_{p0}^5 \omega_0^3}{\left(9\omega_0^2 - \Omega^2\right) \left(\omega_0^2 - \Omega^2\right)^3}, \quad (4.27)$$

where Q_e and R_e are the charge and the radius of the electron core, ω_{p0} is the plasma frequency corresponding to N_0, and $\Omega = \Omega_0 + \delta\Omega = 0.989 \cdot \omega_{p0}/\sqrt{3}$ is the eigenfrequency in nonuniform cluster.

At each time step, the code computes the first time derivative $\dot{D}$ of the cluster dipole moment D. This gives $\dot{D}$ as a function of time. In order to calculate the cluster response at the third harmonic, we Fourier transform $\dot{D}$ and filter out all frequencies except those in the third harmonic vicinity, which finally gives us the computed value of $D_{(3)s}$.

In the first set of simulations, we choose the laser frequency such that $3\omega_0 = 1.06 \cdot \Omega_0$ and vary the laser amplitude. According to Eq. (4.27), the cluster response at the third harmonic should cubically depend on amplitude. Figure 4.1 shows comparison between the simulation results and the theoretical prediction given by Eq. (4.27). For low laser amplitudes the linear cluster displacement is smaller than the size of the electron core and the results of the simulation are in good agreement with the theory. As the amplitude of the core oscillations increases, the average ion density seen by the electron core

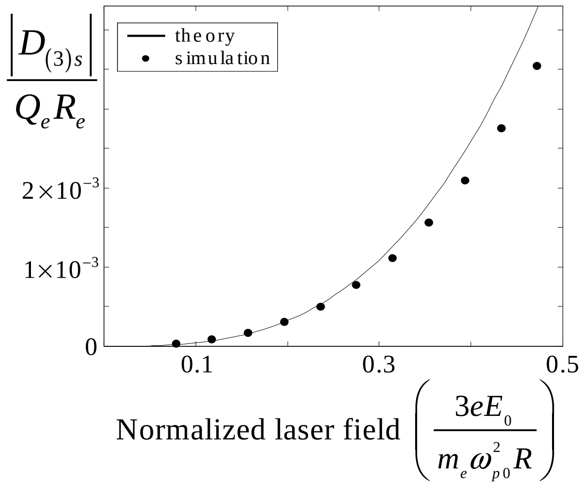

Figure 4.1: Normalized dipole moment of the cluster at the third harmonic ($|D_{(3)s}|/Q_e R_e$) as a function of the laser field amplitude. The dots are the simulation results, the solid line is the theoretical prediction given by Eq. (4.27). The cluster is nonuniform with a density profile given by Eq. (2.20), where $\Delta N/N_0 = -0.2$.

decreases, moving the resonance frequency Ω away from $3\omega_0$, which explains the deviation from the theoretical curve in Fig. 4.1.

In the second set of simulations, we keep the laser field amplitude fixed and we vary the laser frequency in the proximity of the "resonance" frequency $\Omega/3$. The results are presented in Fig. 4.2 that shows the cluster dipole moment at the third harmonic as a function of the laser frequency. We observe very good agreement between simulations and theory in this figure.

4.4.2 Enhancement of the 3rd harmonic during cluster expansion

As already stated, the frequency of the dipole mode Ω is larger than the triple laser frequency at solid state densities. As the cluster expands, its density and

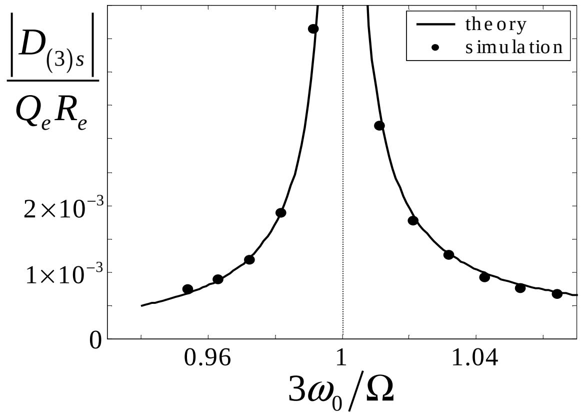

Figure 4.2: Normalized dipole moment of the cluster at the third harmonic ($|D_{(3)s}|/Q_eR_e$) as a function of the laser frequency. The dots are the simulation results, the solid line is the theoretical prediction given by Eq. (4.27). The cluster is nonuniform with a density profile given by Eq. (2.20), where $\Delta N/N_0 = -0.2$.

the eigenfrequency Ω decrease, so that Ω can eventually cross the resonance value $3\omega_0$.

In order to simulate this process, we use the same setup as for induced oscillations in subsection 2.3, except we let the ions move. Almost all the electrons remain inside the cluster during the simulation. Only a small fraction of electrons crosses the boundary at the end of the simulation. This configuration allows us to demonstrate the harmonic generation in the expanding cluster due to the cold electrons alone.

We choose the initial conditions in such a way, that the third harmonic is slightly bellow the eigenfrequency ($3\omega_0 = 0.88\Omega$). We first take an artificially large ion mass $m_i = 50000m_e$ in order to slow down cluster expansion and make the effect more pronounced. Figure 4.3 shows the result of this simulation. We observe that:

a) The electron response is virtually linear at the beginning of the laser

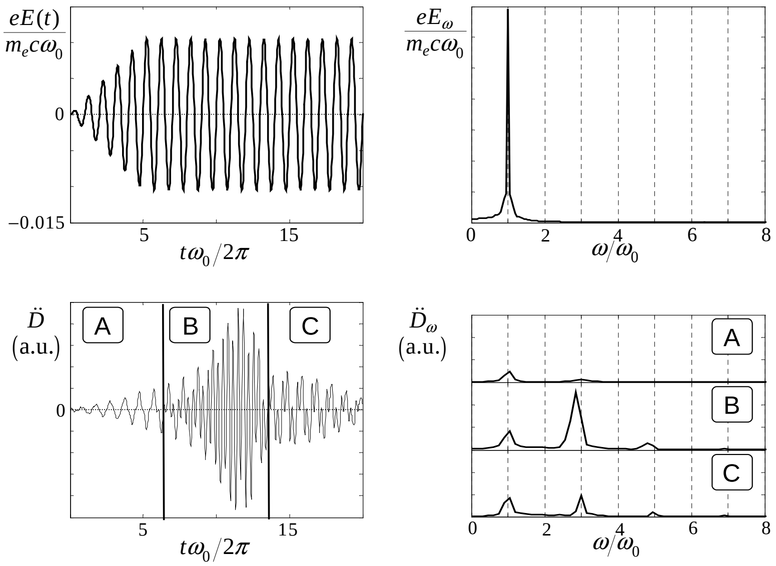

Figure 4.3: Enhancement of the third harmonic during expansion of a cluster with artificially heavy ions ($m_i = 50000m_e$). Initial cluster consists of a cold electron core inside an uncompensated ion shell. The core oscillates inside the expanding cluster. The enhancement happens when the core eigenfrequency matches the third harmonic of the laser frequency. The upper graphs show the incident laser field as a function of time and its spectrum. The lower left graph shows the time evolution of the second time derivative $\ddot{D}$ of the cluster dipole moment D. The three lower right graphs show the spectra of $\ddot{D}$ corresponding to the time intervals A, B, and C shown on the lower left graph.

pulse.

b) As the cluster expands and the resonance frequency matches the third harmonic frequency, significant energy goes into the third harmonic.

c) The third harmonic is still present later in time, but it is not as strong as during resonant enhancement.

Next, we take the parameters close to the real experiments [53]: $\lambda = 1\mu$, $\omega_p/\omega_0 = 6.6$ and $m_i = 4000m_e$. This corresponds to a deuterium cluster with the density of $N_0 = 4.85 \times 10^{22}\text{cm}^{-3}$. The cluster radius is $R = 4.6\text{nm}$, the core radius is $R_e = 2.5\text{nm}$. The field amplitude is $eE_0/m_e c\omega_0 = 0.0315$, which

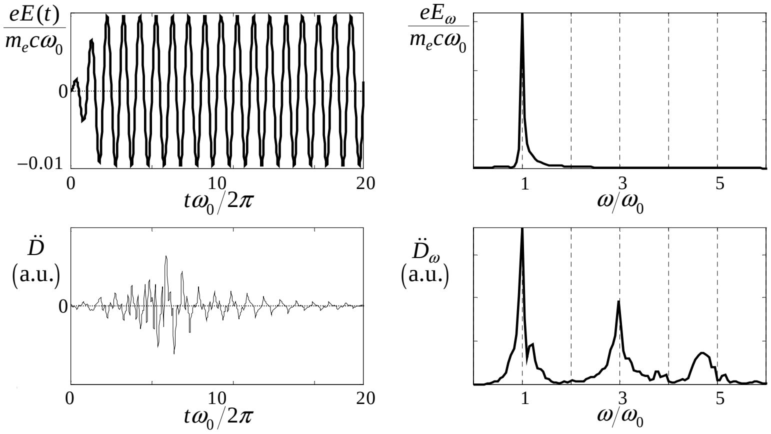

Figure 4.4: The third harmonic generation in an expanding Deuterium cluster. Initial cluster consists of a cold electron core inside an uncompensated ion shell. The upper graphs show the incident laser field as a function of time and its spectrum. The lower graphs show the time evolution of the second time derivative $\ddot{D}$ of the cluster dipole moment D and the corresponding spectrum. As the cluster expands the electrons leak out from the core, which explains the decay of the cluster response in the left bottom graph

corresponds to the core displacement $d = 0.16$nm and the extracted electron excursion $\zeta = 2.4$nm. The result of the simulation is shown in Fig. 4.4. A new element that we observe in this simulation is the electron leakage through the ion shell during the relatively fast expansion of the shell. It takes only 15 laser periods for all electrons to leave the expanding cluster, which is evident from the signal depletion in Fig. 4.4.

4.5 Role of hot electrons

How will the situation change if there is no ion shell preventing electrons from leaving the cluster? In order to answer this question, we do another simulation with the same parameters as in section 4.4.2, but setting the initial radius of the ion sphere R equal to the radius of the electron core R_e, so that the cluster is initially neutral. Here we take $m_i = 50000m_e$ in order to suppress cluster expansion early in time. The result of this simulation is presented in Fig. 4.5. In comparison with the previous case (Fig. 4.3), we now observe third harmonic generation at the early stage of the interaction. The underlying reason is that the extracted electrons excite the third harmonic transiently as they move back and forth across the edge, before leaving the cluster for good.

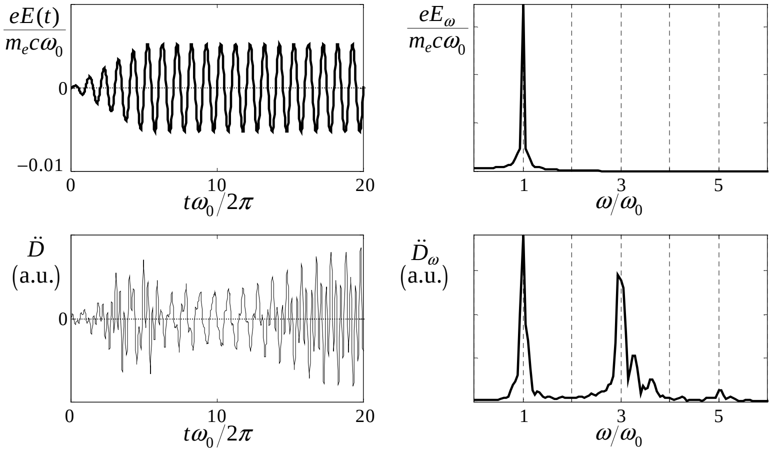

Figure 4.5: The third harmonic generation during expansion of initially neutral cluster with artificially heavy ions ($m_i = 50000m_e$). The upper graphs show the incident laser field as a function of time and its spectrum. The lower graphs show the time evolution of the second time derivative $\ddot{D}$ of the cluster dipole moment D and the corresponding spectrum. The harmonic generation at early time is caused by the extracted electrons. After the extracted electrons leave, the third harmonic disappears. Later in time the third harmonic emerges again when its frequency matches the core eigenfrequency.

Figure 4.6 shows that there are electrons that are not confined inside the cluster after 7 laser periods. The ion density is still very close to uniform at this moment. It appears that mostly the extracted electrons produce the nonlinear response at the early stage. Later in time, the extracted particles are nearly gone, but the ion density profile becomes strongly nonuniform because of the cluster expansion. At this stage, the mechanism for harmonic generation is the sam

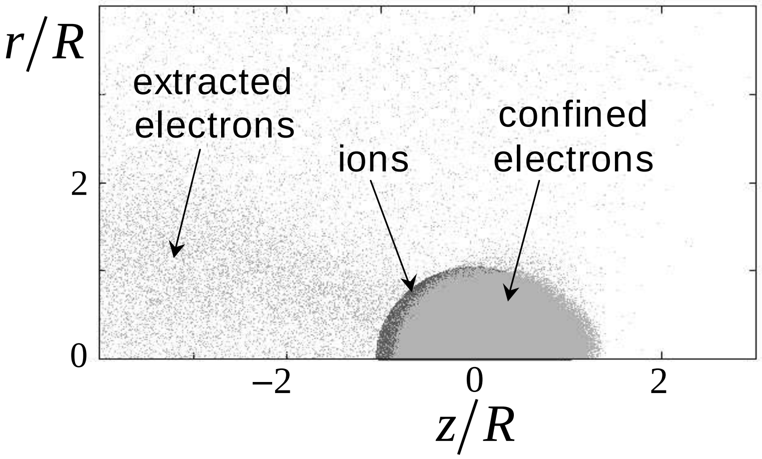

Figure 4.6: Configuration of initially neutral cluster with artificially heavy ions ($m_i = 50000m_e$) after approximately 7 laser periods.

In order to verify this interpretation, we perform another simulation with the same parameters, except that we freeze the ions to keep their density uniform. Figure 4.7 shows that, in this case, the third harmonic arises at the early stage only (due to the extracted electrons).

Figure 4.8 shows partial contributions of the two electron populations to the oscillating dipole moment of the cluster. Early in time, the electron response is linear. As the laser heats more electrons, the response exhibits nonlinearity. The spectrum indicates the presence of the third harmonic. One may think that the third harmonic stems from the stochastic motion of the hot electrons. A more detailed analysis shows that this is not the case. Although there is third harmonic component in the hot electron dipole moment, it is significantly smaller than that of the core electrons. The motion of the core

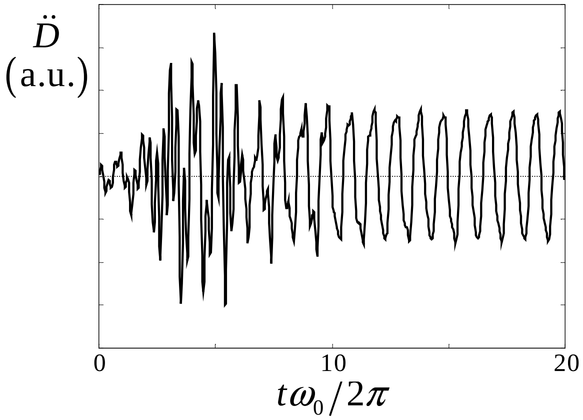

Figure 4.7: Transient generation of the third harmonic by the extracted electrons in an initially neutral and uniform cluster with immobile ions. As the extracted electrons leave, the third harmonic disappears.

electrons appears to be affected by the nonuniform space-charge of the hot electron halo and it is no longer harmonic as it would be in the absence of the hot population.

4.6 Summary

The underlying premise of this chapter is that a laser-irradiated cluster generally contains two electron populations, the cold core and the heated halo. Electrons in the core move collectively in step with the applied laser field. On the other hand, the stochastically heated halo electrons move in a chaotic manner.

Our analytic model deals with the oscillatory motion of the core in a potential well provided by the ions of the cluster. The nonlinear response of the core is due to nonuniformity of the ion density, which could be due to some intrinsic nonuniformity or may arise naturally in the process of cluster

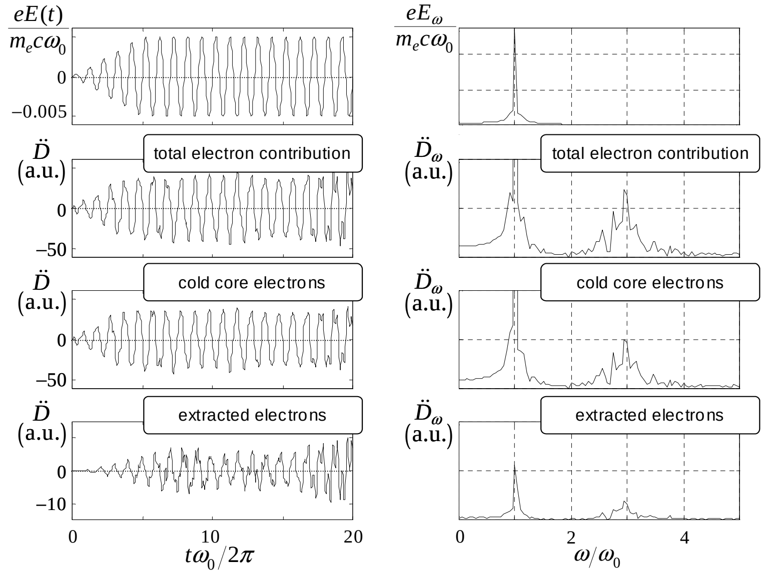

Figure 4.8: Harmonic generation in the presence of the hot electron halo. The left column shows the time dependence of the laser field, the second time derivative $\ddot{D}$ of the cluster dipole moment and the contribution to $\ddot{D}$ from the cold and hot electrons. The right column shows the corresponding spectra.

expansion. When the third harmonic of the laser frequency is in resonance with the Mie frequency, which is the experimentally relevant case, the cluster exhibits enhancement of third harmonic generation. In the present work, this resonant enhancement has been confirmed through PIC simulations.

Our simulation work also confirms the presence of the halo electrons (see Chapter 2, Sec. 2.4). Here the vacuum heating mechanism is operative. The characteristic energy of halo electrons increases in time due to vacuum heating and the number of halo electrons increases as well. Since the halo is less dense than the cold core and its motion is incoherent albeit nonlinear, the halo contributes less than the core to the third harmonic signal. Also, the timing of the halo response is different.

It remains to be a challenge to observe such two-component electron dynamics experimentally and to quantitatively compare our description of enhanced harmonic generation with experimental data.

Chapter 5

Axisymmetric electrostatic particle-in-cell code

5.1 Model and assumptions

We use particle-in-cell code to simulate electron and ion dynamics self-consistently. The assumptions that the laser wavelength is much larger than the cluster size and that the motion of the particles is non-relativistic make the problem electrostatic. The laser electric field is introduced in the simulation as a spatially uniform function of time; the magnetic field is neglected. We assume that the laser is linearly polarized and that the cluster is axisymmetric with the axis of symmetry along the laser electric field. The code employs cylindrical coordinates with axial symmetry.

Our numerical model has three important distinctions from earlier 2D simulations performed in Cartesian coordinates [12]. First, we address a 3D physical problem that is relevant to spherical clusters as opposed to rod-like clusters. The electrostatic potential falls off faster with distance for a spherical cluster, which changes the behavior of the extracted electrons significantly. Also, the electron eigenmodes are different for spherical and rod-like clusters. Second, the electrostatic approximation makes our code faster than the earlier electromagnetic code since the size of our simulation box is only a small fraction of the laser wavelength. In experiments, the clusters are about 100 times smaller than the wavelength [10]. Our simulation box is typically five times larger than the cluster radius, which saves computation time while capturing most of relevant physics. Third, our code does not impose periodic boundary conditions, which is convenient for modeling isolated clusters.

The macro-particles in our axisymmetric code represent charged rings. Each particle has only radial and axial components of the velocity. The azimuthal velocity is zero because of the axial symmetry. The electric field consists of two parts: the external (laser) field, which is a given function of time, and the Coulomb part. The Coulomb electric field is calculated by transferring the charge density onto the grid and then solving the Poisson's equation using the multigrid method [54, 55]. The boundary condition for an isolated cluster is such that the electrostatic potential vanishes at infinity. Since our simulation box is finite, we need to precalculate the value of the potential at the edge of the simulation box in order to formulate the boundary value problem for Poisson's equation. Since the box is larger than the size of the cluster, we use the total charge and the dipole moment of the particles in the box to find the potential at the boundary. By doing so, we reduce the error in the boundary condition from the order of R/L to the order of $(R/L)^3$, where L is the size of the box and R is the cluster radius.

We assume that the cluster is fully ionized and located at the center of

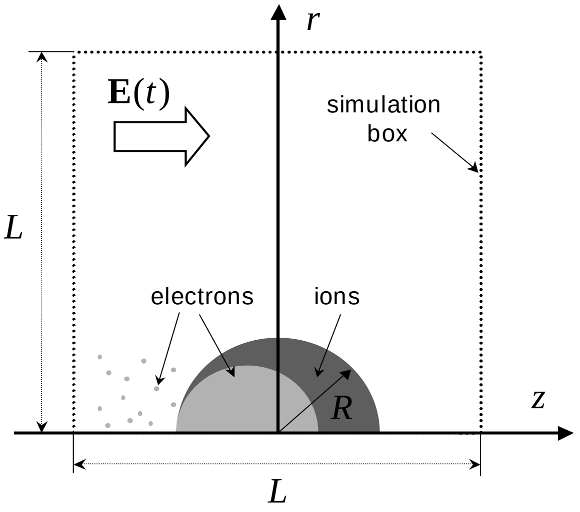

Figure 5.1: Simulation setup.

the simulation box (see Fig. 5.1). If an extracted electron reaches the edge of the simulation box, we remove it from the simulation. A macroparticle away from the axis represents more real particles than a macroparticle in the central region. When a large macroparticle moves close to the axis, we split it into several macroparticles in order to keep the number of macroparticles per cell much larger than unity.

In most of our simulations, 12000 grid points correspond to one laser wavelength e.g. 800nm. The initial cluster radius in a typical run is 30-50 grid points. Electron core can have a smaller radius than the ion background. A typical size of the simulation box is 256×256 grid points. The total number of particles during a run varies from hundreds of thousands to several millions. The simulation of 10-20 laser periods takes less than half an hour on a 2.8 GHz Pentium 4 PC.

5.1.1 Limits of applicability

Absence of magnetic field

Clearly, the presence of magnetic field would break the symmetry of the problem. The legitimate question is how well our approximation describes the real laser-cluster interaction and when the magnetic field changes the particle dynamics? The condition for the escaped electrons is the same as that for a free electron: $eE_{\text{laser}}/mc\omega_0 \ll 1$. A more interesting question is under what condition the inner electrons are affected by the presence of the magnetic field? The motion of such electrons is described by

$$\ddot{\mathbf{r}}m = -e\left(\mathbf{E_{in}} + \frac{\dot{\mathbf{r}}}{c} \times \mathbf{B}\right), \tag{5.1}$$

where $E_{in} \approx 3\frac{\omega_0^2}{\omega_p^2}E_{\text{laser}}$ is the electric field inside the cluster [see Eq. (2.25)], B is the laser magnetic field, $\dot{r} = v_{\text{core}} \approx 3c\frac{\omega_0^2}{\omega_p^2}\frac{eE_{\text{laser}}}{mc\omega_0}$ [see Eq. (2.29)]. The magnetic field can be neglected when the ratio of the magnetic force to the electric force in Eq. (5.1) is small:

$$\frac{eE_{\text{laser}}}{mc\omega_0} \ll 1. \tag{5.2}$$

Note that although electron motion inside the cluster is always sub-relativistic, the condition for neglecting the magnetic field is the same as for a free electron in vacuum.

Collisionlessness

The particles-in-cell algorithm suppresses binary collisions. In the real experiment the ion-electron collisions may lead to electron heating. The characteristic time of the heating is given by [17]

$$\tau_H = \frac{1}{\nu_{ie}(\epsilon^*)}\frac{\omega_p^2}{\omega^2}$$

where $\epsilon^* = \frac{m_e}{2}\left(\frac{eE}{m_e\omega_p}\right)$ is the characteristic energy of the electron in the electromagnetic field, ν_{ie} is the ion-electron collision frequency. As long as the simulation time is shorter than this time, the effects of the collisional heating are not important and the model is valid.

Ionization

For light atoms, such as hydrogen, the ionization threshold is very low ($\sim 10^{14}\mathrm{W/cm}^2$) compared to the typical laser intensities $10^{15} - 10^{17}\mathrm{W/cm}^2$ in cluster experiments. As a result, the atoms in the cluster are completely ionized by the time the main part of the pulse reaches the cluster. Heavy atoms may be partially ionized during the interaction. This may lead to nonuniform ionization [16] and other interesting changes in the cluster dynamics, which goes beyond the scope of this thesis.

5.2 Geometry, equations, and boundary conditions

Our code employs cylindrical coordinates (r, z), with a simulation box determined by $0 < r < R_{\mathrm{box}}$ and $-L_{\mathrm{box}}/2 < z < L_{\mathrm{box}}/2$. The size of the simulation box is typically several times larger than the cluster radius R and smaller than the laser wavelength λ. Since the laser wavelength λ is much larger than the size of the cluster R, the laser field in the simulation box is set to be a spatially uniform function of time. We assume that the laser pulse is linearly polarized in z direction and has subrelativistic intensity with normalized vector potential $a_0 = eE_0/mc\omega_0 \ll 1$. This allows us to neglect the effects of the magnetic field and makes both electron and ion response to the laser field axisymmetric.

The cluster can have any axisymmetric shape. In the code each macroparticle represents a charged ring. Suppose, we want to simulate a cylindrically symmetric neutral cluster, for example, a spherical cluster. We then construct the corresponding initial mass-charge distribution from positively and negatively charged rings. The rings may have the same charge (and mass) or be uniformly distributed in (r, z) but have different masses and charges to form the desired density profile. The first representation requires more memory and CPU operations, since the the number of particles per cell increases proportionally to r. The second representation is more efficient but it is problematic if the particle layers cross. In this case, "heavy" particles from the areas with large r may reach the small volume cells in the region of small r and lead to significant numerical noise. We resolve this problem by splitting a heavy particle in half if its mass exceeds 10% of the cell volume times the initial density. One would want to use the first type of particles to represent hot electrons, and the second type of particles to represent ions. Every ring is characterized by its position (r^k, z^k), momentum (p_r^k, p_z^k), charge q^k, and mass m^k. The equations of motion then are:

$$\begin{aligned} \frac{dp_r^k}{dt} &= q^k E_r(r^k, z^k) \\ \frac{dp_z^k}{dt} &= q^k E_z(r^k, z^k) \\ \frac{dr^k}{dt} &= \frac{p_r^k}{m^k} \\ \frac{dz^k}{dt} &= \frac{p_z^k}{m^k} \end{aligned} \tag{5.3}$$

At $r = 0$ we use "mirror" boundary condition for particles. If r^k turns out to be negative after advancing a particle position, we change its sign and reverse the radial component of the particle's momentum p_r^k as well. If an electron escapes from the cluster and reaches the edge of the simulation box, that is $r^k > R_{box}$ or $|z^k| > Z_{box}/2$, then the particle is removed from the simulation. The underlying reason is that since the particle is no longer bound to the cluster potential and is unlikely to return back. On the other hand the contribution of such particles to the field inside or near the cluster is also negligible. This is specific property to 3D geometry, where the potential drops as $1/r$, In 1D and 2D geometries the particles are always bound to the cluster.

The electric field consists of two parts. The first one is the external laser field, the second one is the self-consistent field $-\nabla\phi$, caused by space-charge separation, where

$$\begin{cases} \nabla^2\phi = -4\pi\rho \\ \partial_r\phi|_{r=0} = 0 \\ \phi|_{r=\infty} = 0 \\ \phi|_{z=\pm\infty} = 0 \end{cases} \tag{5.4}$$

and the charge density ρ is calculated from the particle distribution.

5.3 Numerical implementation

The simulation box of the size $R_{box} \times H_{box}$ is divided into $N \times N - 1$ cells of equal hight and width Δ, where $N = 2^k$ for some integer k. The boundaries of the cells are planes $z_j = j$ and cylinders with $r_i = 0.5 + i$ for integer i and j. The distance between grid points serves as a unit of length in the code. The unit of time is inverse plasma frequency ω_p^{-1}, where $\omega_p^2 = 4\pi n_0 e^2/m_e$. The density is in the units of n_0. For example, the "frequency" of the electron dipole mode in a cluster of ”density” 1 in the code would be $1/\sqrt{3}$. The unit of momentum is mc, where m is the particle mass.

5.3.1 Density calculation

All macroscopic quantities such as electrostatic potential, charge density and electric field are evaluated at the grid points which are located at the centers of the cells, that is at points with $r_i = i$ and $z_j = j + 0.5$ for integer i and j. Knowing the positions of all the particles, we compute the charge density at the grid point. This is done by using the following 4-point weighing scheme. Let the position of the k^{th} particle be given by $r = r_i + dr$ and $z = z_j + dz$, where (r_i, z_j) is the coordinate of a grid point and $0 \leq dr < 1$, $0 \leq dz < 1$. Then the contribution to the density from k^{th} particle is:

$q^k dr \cdot dz/V_{i,j}$ at point grid point (i, j),

$q^k(1 - dx) \cdot dy/V_{i+1,j}$ at point grid point $(i + 1, j)$,

$q^k dx \cdot (1 - dy)/V_{i,j+1}$ at point grid point $(i, j + 1)$,

$q^k(1 - dx)(1 - dy)/V_{i+1,j+1}$ at point grid point $(i + 1, j + 1)$,

where $V_{i,j}$ is the volume of cell (i, j).

5.3.2 Calculation of the fields

Having the charge density at the grid points we solve Poisson equation to find the electrostatic potential.

$$\nabla^2\phi = -4\pi\rho$$

In order to implement the boundary condition $\phi|_\infty = 0$, we take the simulation box a few times larger than the characteristic size of the cluster and we approximate the value of the potential at the boundary of the box using multipole expansion up to the dipole moment. Therefore, the error in the boundary condition for the potential is of the order of $(R/L_{\text{box}})^3$, where R is the characteristic size of the cluster and L_{box} is the size of the simulation box. The boundary condition at the axis of symmetry is $\partial_r\phi|_{r=0} = 0$.

We use time-efficient multigrid method, which has the complexity of $O(N^2)$, where N^2 is the total number of the grid points. The numerical version of the Poisson equation in cylindrical coordinates is

$$\nabla^2\phi^{j,i} = \phi^{i,j}_{rr} + \frac{1}{r}\phi^{i,j}_{r} + \phi^{i,j}_{zz} = -4\pi\rho^{i,j}, \tag{5.5}$$

where

$$\begin{aligned} \phi^{i,j}_{rr} &= \tfrac{\phi^{i+1,j}-2\phi^{i,j}+\phi^{i-1,j}}{\Delta^2}, \\ \phi^{i,j}_{zz} &= \tfrac{\phi^{i,j+1}-2\phi^{i,j}+\phi^{i,j-1}}{\Delta^2}, \\ \phi^{i,j}_{r} &= \tfrac{\phi^{i+1,j}-\phi^{i-1,j}}{2\Delta}; \end{aligned}$$

and Δ is the distance between grid points. We start with some approximate solution $\phi^{i,j}_0$ to discrete equation (5.5) on the grid $N \times N - 1$, where $N = 2^k$. Then we perform several Gauss-Seidel iterations, also known as relaxation method:

$$\phi^{i,j}_{k+1} = \phi^{i,j}_{k} + dt(\nabla^2\phi^{i,j} + 4\pi\rho^{i,j}) = \phi^{i,j}_{k} + dtL\phi^{i,j},$$

where $dt = \Delta^2/4$. These iterations smooth the residue $u^{i,j} = L\phi^{i,j}$, this means that the high order harmonics of the descrete Fourier transform of $u^{i,j}$ quickly converge to zero during these iterations. In order to eliminate low order components of the residue $u^{i,j}$, we transform the equations onto a coarser grid $N_1 \times N_1 - 1$, where $N_1 = 2^{k-1}$. On this grid we solve the equation

$$L\delta\phi^{I,J} = -u^{I,J} \tag{5.6}$$

where $\delta\phi^{I,J}$ is the correction to $\phi^{i,j}$ such that $L(\phi+\delta\phi) = 0$. After finding $\delta\phi^{I,J}$, we interpolate it back to the fine grid using 2D linear interpolation getting

$\delta\phi^{i,j}$. The new approximation to the solution of equation (5.5) is $\phi^{i,j} + \delta\phi^{i,j}$. After that, we perform several Gauss-Seidel iterations again to smooth the residue. The whole cycle is then repeated until we get the required precision, i.e., until the absolute value of the residue $u^{i,j}$ becomes much smaller than unity. The equation (5.6) is a Poisson equation on the coarser grid. Therefore, we solve it the same way, using Gauss-Seidel iterations, going to even coarser grid and back and doing Gauss-Seidel iterations again. The process of going to the coarser grid is repeated recursively until we reach a grid of the size 2×1, where the equations can be solved explicitly. During the transformation of the equations from one grid to another, we need to transform both the discrete functions, such as ϕ, ρ, and u, and the boundary conditions. In the case of the cylindrical geometry it is convenient to do it if we use the grid size of $2^k \times 2^k - 1$. In this case in order to go to the coarser grid we just through away every second row and column on our grid as shown in Fig. 5.2. The circles indicate the grid points, the squares indicate the points at which the boundary conditions are specified. When we change to a coarse grid only the grid points marked with the white dots remain.

From the particle distribution we calculate the charge density $\rho^{i,j}$ and the boundary vales of the electrostatic potential $\phi^{i,0}$, $\phi^{i,N-1}$, and $\phi^{N-1,j}$ on the finest grid, where $i = 0..N-1$, $j = 0..N-2$. The transition to the coarse grid is done according to the formulas:

$$\begin{aligned}
\rho^{I,J} &= \frac{1}{4}\rho^{i,j} + \frac{1}{8}(\rho^{i-1,j} + \rho^{i+1,j} + \rho^{i,j-1} + \rho^{i,j+1}) + \\
&\quad \frac{1}{16}(\rho^{i-1,j-1} + \rho^{i-1,j+1} + \rho^{i+1,j-1} + \rho^{i+1,j+1}) \\
\phi^{I,0} &= \frac{1}{2}\phi^{i,0} + \frac{1}{4}(\phi^{i-1,0} + \phi^{i+1,0}) \qquad (5.7)
\end{aligned}$$

$$\begin{aligned}\phi^{I,N/2-2} &= \frac{1}{2}\phi^{i,N-2} + \frac{1}{4}(\phi^{i-1,N-2} + \phi^{i+1,N-2}) \\ \phi^{N/2-1,J} &= \frac{1}{2}\phi^{N-1,j} + \frac{1}{4}(\phi^{N-1,j-1} + \phi^{N-1,j+1})\end{aligned}$$

where $i = 2I$ and $j = 2J$.

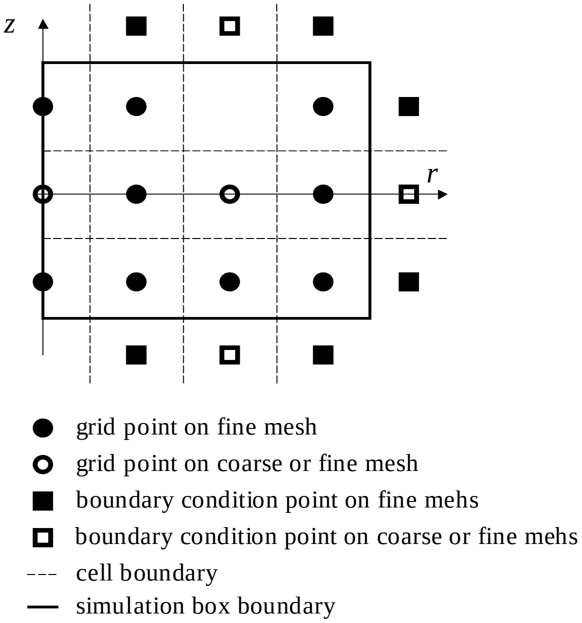

Figure 5.2: Multigrid implementation

In order to start the iterations of any iterative algorithm, such as Gauss-Seidel we need some initial approximation to the solution. Any initial approximation will converge, however, if it is not very close to the real solution it will require more iterations. We implement the so-called **full multigrid** method. This means that before starting iterations, we first solve the problem on the coarsest grid. Next, we interpolate this solution onto the finer grid and use the result as the first approximation for this grid. Then refine the grid again, until we get the approximate solution on the grid of interest. Finally, the iterative multigrid method described above is used to further reduce the error.

5.3.3 Numerical frequency shift in leap-frog method

In our code particle coordinates and fields are specified at integer time point, whereas velocities are specified at semi-integer points. Core oscillation in a uniform cluster are equivalent to the following discrete equations (this method is known as leap-frog scheme):

$$\begin{cases} x_{n+1} & = x_n + v_{n+1/2}\Delta t, \\ v_{n+3/2} & = v_{n+1/2} - \Omega_0^2 x_{n+1} \Delta t. \end{cases} \tag{5.8}$$

We look for a periodic solution in the form:

$$x_n = A e^{\jmath \Omega n \Delta t}. \tag{5.9}$$

Then

$$v_{n+1/2} = \frac{x_{n+1} - x_n}{\Delta t} = \frac{A}{\Delta t} e^{\jmath \Omega_n \Delta t} \left(e^{\jmath \Omega \Delta t} - 1 \right) \tag{5.10}$$

Combining this equation with Eqs. (5.8) and (5.9) yields

$$\frac{A}{\Delta t} e^{\jmath \Omega (n+1) \Delta t} \left(e^{\jmath \Omega \Delta t} - 1 \right) - \frac{A}{\Delta t} e^{\jmath \Omega n \Delta t} \left(e^{\jmath \Omega \Delta t} - 1 \right) = -\Omega_0^2 A e^{\jmath \Omega (n+1) \Delta t}. \tag{5.11}$$

This expression can be simplified to

$$\frac{\Omega_0 \Delta t}{2} = \sin(\Omega \Delta t / 2) \tag{5.12}$$

By expanding sin() in the RHS into Taylor series up to the third order and substituting $\Omega = \Omega_0 + \delta\Omega_{\mathrm{num}}$, we obtain the following expression for the numerical frequency shift:

$$\frac{\delta\Omega_{\mathrm{num}}}{\Omega_0} = \frac{(\Omega_0 \Delta t)^2}{24}. \tag{5.13}$$

Part II

Raman Seeded Laser Wakefield Acceleration

Chapter 6

Motivation

Because electrostatic fields in a relativistic plasma wave can exceed those in radio-frequency linear accelerators by 3 orders of magnitude, plasma based accelerators can potentially provide a compact source of high energy electron bunches [56]. Of the various methods of driving large-amplitude plasma waves [2], the Self-Modulated Laser Wakefield Accelerator (SM-LWFA) [24, 25, 26] has so far yielded electron bunches of the highest energy (tails to >200 MeV [27, 57]), charge (> 1 nC/bunch [28, 29]) and collimation (transverse emittance $\epsilon_\perp < 0.1\pi$ mm $\cdot$ mrad [30]). In the SM-LWFA, the plasma density n_e is chosen such that the duration τ_{pulse} of the driving pulse (typically 0.1 ps$< \tau_{pulse} < 1$ ps) significantly exceeds the plasma period $\omega_p^{-1} = (4\pi n_e e^2/m)^{-\frac{1}{2}}$ (typically 10^{19} cm$^{-3} < n_e < 10^{20}$ cm^{-3} or 2 fs$< \omega_p^{-1} < 6$ fs). Such pulses are subject to envelope modulation due to Forward Raman Scattering (FRS) and Envelope Self-Modulation (ESM) instability, also called Resonance Modulation Instabilities (RMI) [40]. Modulation breaks the long pulse into short subpulses of duration equal to the plasma period, which resonantly excite a high amplitude plasma wave. Under these conditions, a collimated beam of multi-MeV electrons, resulting from capture and acceleration of electrons from the surrounding plasma by the plasma wave, has been observed in several laboratories [28, 29, 31, 32, 33, 27]. The beam properties achieved in recent work are favorable enough that near-term applications of the SM-LWFA - including table-top nuclear activation of rare isotopes [29], injectors for conventional high-energy physics (HEP) accelerators, and radiation oncology [34, 35, 36] - are gradually emerging.

A disadvantage of the SM-LWFA is the high peak power of the driving laser pulses, which is required to achieve the necessary beam energy, collimation, and peak current for practical applications. This restricts laser repetition rate to a few Hertz, and average current to nano-amp levels. Most demonstrations of SM-LWFA have, in fact, been essentially single-shot ($\ll 1$ Hz) [31, 32, 28, 33]. Only recently has high quality SM-LWFA been achieved at repetition rates as high as 10 Hz [29]. However, kilohertz repetition rates (micro-amp average currents) are desirable for most applications. Recently laser systems capable of delivering pulses approaching $\sim$1 TW at $\sim$1 kHz repetition rate have indeed been developed [58]. However, these pulses currently fall short of the threshold required for efficient SM-LWFA. Therefore, it is timely to investigate schemes for "seeding" the growth of RMI that have the potential to reduce the threshold energy for SM-LWFA to levels achievable by kHz laser systems, while retaining the favorable beam characteristics (high peak current, collimation, energy).

Here we investigate through 1D and 2D particle-in-cell (PIC) simulations a Raman-seeding mechanism [59, 38, 39], in which a driving pulse with frequency ω is "seeded" by a co-propagating superposed pulse of a substantially lower intensity and with a frequency $\omega_{seed} \approx \omega - \omega_p$. The presence of this seed pulse greatly enhances RMI compared to the unseeded case. Recent demonstration of experimental schemes for generating Raman-shifted seed pulses by chirped-pulse stimulated Raman scattering in Raman-active crystals [60] has further motivated the present study.

Our regime of interest must be distinguished from previous studies of plasma beat-wave acceleration (PBWA), in which, although two incident pulses that differed in frequency by ω_p were also used, the plasma density was much lower (typically $n_e < 5 \times 10^{16}$ cm^{-3}) [61, 62, 63] than the density considered here. In the PBW regime, the wakefield generation is inefficient unless the two pulses are comparable (i.e. within one order of magnitude) in intensity. In addition, in low density PBWA experiments, the two driving pulses were close enough in frequency that they were produced from within the spectral bandwidth of the same parent laser – e.g. by using neighboring spectral lines of a CO_2 laser [61, 62], or by dividing the bandwidth of a Ti:S laser using etalons [64] or frequency masks [65] – and could thus easily be rendered comparable in intensity. Moreover, from a theoretical standpoint, the physics of PBWA differs in two important respects from the case we consider. First, electron pickup from the background plasma does not occur because the accelerating fields are smaller, and Backward Raman Scattering (BRS), which is an important mechanism for pre-accelerating electrons to the capture threshold, produces less energetic electrons than at higher density. Second, the laser-plasma interaction at low density consists almost entirely of the action of the linear ponderomotive force on the plasma electrons.

By contrast, in the high density SM-LWFA regime, the sideband pulse would, in practice, have to be generated outside the bandwidth of most available high intensity laser systems. For this reason, it is more appropriate to refer to the sideband generation as “Raman shifting”. This process is inevitably inefficient, so there is little practical interest in considering the case of comparable intensities. A Raman-shifted pulse 100 times less intense than the parent driving pulse can, in sharp contrast to the PBWA regime, critically influence the production of a high amplitude plasma wave by creating a favorable initial condition, or “seed”, for the growth of RMI. For this reason, it is appropriate to refer to the sideband as a “Raman seed” in the high density regime. The subsequent physics also differs qualitatively from the PBWA regime. In high density regime, BRS excites a short-scale plasma wave, which easily breaks, proving enough momentum for electrons to get injected into the accelerating phase of the large-scale wakefield. Therefore, electron pickup from the background plasma becomes important, and can be as efficient as in conventional SM-LWFA. Moreover, other 1D and 2D laser-plasma nonlinearities such as relativistic self-focusing and RMI, etc. – that are negligible at lower density, influence the interaction strongly at high density, and must be taken into account. However, unlike SM-LWFA, Raman seeding allows wakefield excitation and particle acceleration in the low pulse amplitude regime, where the pulse is less subjects to undesirable instabilities such as self-focusing and RMI can be controlled with the seed parameters (see Chapter 8).

In view of recent demonstrations of high quality SM-LWFA beams, kHz TW laser systems, Raman-shifted seed pulses, and potential applications that could benefit from reduced threshold, it is imperative to examine the quantitative 1D and 2D simulation features of Raman-seeded laser-wakefield acceleration (RS-LWFA) explicitly. Here are several important points of interest. Since the seeded pulse is introduced externally, we would like to investigate how the variations of seed parameters control wakefield excitations. Up to now electron production in SM regime in experiments has been associated with high intensity pulses, where the power of the laser pulse is greater than the critical power for relativistic self-focusing, i.e. $P > P_c$, where

$$P_c = 17\frac{\omega^2}{\omega_p^2}\mathrm{GW}.$$

In this work, we investigate the possibility of utilizing Raman seed for electron production by pulses in the sub-critical power domain. In this domain, we also investigate how channeling further lowers the production threshold.

Chapter 7

Resonance Modulation Instability and seeding

7.1 1D and 3D regimes of the modulation

There are several different regimes of Resonance Modulational Instability (RMI) [40, 66]. When $16(\omega/\omega_p)^2/(k_p\sigma_\perp)^2 < 1$, where $k_p = \omega_p/c$, $\sigma_\perp$ is the spot-size, the modulation is caused by 1D RMI known as Forward Raman Scattering (FRS). When $\sigma_\perp k_p < \omega/\omega_p$, the problem becomes essentially three-dimensional and the dominant modulation mechanism is Envelope Self-Modulation (ESM). For the parameters of interest (low energy pulses with the interaction length limited by diffraction or dephasing), the 4-wave FRS and ESM are important. For the detailed classification of RMI regimes, see Ref. [40].

At early times, the main mechanism of the pulse modulation in the self-modulation regime is FRS [66, 67]. It begins with the leading edge of the incident pulse (or some other perturbation) exciting a plasma wave with frequency ω_p. The rest of the pulse scatters on this wave into the Stokes and anti-Stokes waves. The beating of the fundamental and scattered waves creates modulation with spacing $\lambda_p = 2\pi c/\omega_p$. Each period of the modulation further excites the plasma wave resonantly, leading to even more scattering, thus creating a positive feedback. The pulse modulation is stronger at the tail of the pulse, since the tail is scattered on the wave created by the entire pulse. The modulation grows in time until saturation, caused by scattering of the Stokes and anti-Stokes waves, which lead to appearance of the higher order Fourier components ($\omega_0 \pm k\omega_p$) and degradation of the modulation structure. Another process leading to saturation is wavebreaking of the plasma wave (see Chapter 9). Before saturation the solution for the growth of the wakefield $\chi = \delta n/n_0 - a_0^2/4$ associated with 4-wave Raman instability is given by [67]:

$$\chi_s = \chi_{s0} \sum_{n=0}^{\infty} \left(\frac{\psi/c}{t - \psi/c} \right)^n I_{2n}(\Gamma) \rightarrow \chi_{s0} \frac{\exp \Gamma}{\sqrt{2\pi\Gamma}}, \tag{7.1}$$

where gain

$$\Gamma_{1D1} = \frac{a_0}{2} \frac{\omega_p^2}{\omega_0} \sqrt{(t - \psi/c)\psi/c} \tag{7.2}$$

is the number of the e-fold magnifications of the original perturbation χ_{s0}, n_0 is the plasma density, δn is the plasma density perturbation, $a_0 = eA/mc^2$ is the normalized vector potential, t is the interaction time during which the laser pulse passes through the gas jet, and ψ is the distance from the head of the pulse. The last expression is the asymptotic form for large values of Γ.

For pulses of small spotsize 3D ESMI quickly becomes dominant [40, 66]. In this process, the excited plasma wave modulates the pulse envelope by forming a periodic refractive structure. The regions with positive density perturbation act as diverging lenses, whereas the regions with negative density perturbation form converging lenses. As a result, the longitudinal profile of the spotsize and, therefore, the amplitude envelope becomes modulated, which causes stronger wakefield excitation. The growth of the modulation can be characterized by the corresponding gain:

$$\Gamma_{3D1} = \frac{3\sqrt{3}}{4}\left(2k_p\psi\right)^{1/3}\left(\frac{a_0 ct}{\sigma_\perp}\right)^{2/3}, \tag{7.3}$$

where $\sigma_\perp$ is the spotsize.

The transition from 1D to 3D regime occurs when Γ_{3D1} becomes larger than Γ_{1D1}. For the parameters used in our 2D simulation, this transition happens at the very beginning of the interaction, which means that ESM dominates most of the time. In 1D simulations only FRS is present.

Putting ψ to be half of the pulse length and neglecting the length of the pulse compared to the interaction length, we can rewrite Eq. (7.2) and Eq. (7.3) in the following form:

$$\Gamma_{1D1} = 21\tfrac{\omega_p^2}{\omega^2}\left(\tfrac{t}{T_R}\right)^{1/2}\left(\tfrac{\varepsilon[\mathrm{mJ}]}{\lambda[\mu]}\right)^{1/2}, \tag{7.4}$$

$$\Gamma_{3D1} = 12.5\tfrac{\omega_p}{\omega}\left(\tfrac{t}{T_R}\right)^{2/3}\left(\tfrac{\varepsilon[\mathrm{mJ}]}{\lambda[\mu]}\right)^{1/3}; \tag{7.5}$$

where ε is the pulse energy, λ is the laser wavelength, $T_R = \pi\sigma_\perp^2/\lambda c$ is the Rayleigh time. Assuming $\omega/\omega_p = 6$ and $\lambda = 0.8\ \mu$ (parameters used in the simulations) the expressions for the gains become:

$$\Gamma_{1D1} = \left(\tfrac{t}{T_R}\right)^{1/2}\left(\tfrac{\varepsilon}{2.4\mathrm{mJ}}\right)^{1/2}, \tag{7.6}$$

$$\Gamma_{3D1} = \left(\tfrac{t}{T_R}\right)^{2/3}\left(\tfrac{\varepsilon}{0.1\mathrm{mJ}}\right)^{1/3}. \tag{7.7}$$

7.2 Relevant regime for Raman seeding

Depending on the value of Γ, the following regimes of modulation can be distinguished:

- $\Gamma \gg 1$ - the modulation quickly develops from any perturbation and saturates almost instantaneously.
- $\Gamma > 1$ - the modulation growth depends strongly on the initial perturbation.
- $\Gamma \leq 1$ - the modulation fails to develop during the interaction time regardless of initial conditions.

The intermediate regime with $\Gamma > 1$ is the main focus of this work. There are two reasons for this.

First, by introducing a finite amplitude external perturbation with Raman seed, we can reduce the energy threshold for modulation and strong wakefield excitation to the low mJ range (see Eq. (7.6) and Eq. (7.7)). Since pulsed laser systems can typically produce ∼10 W average power, repetition rate approaching 1 kHz may be within reach. However, modulation growth and electron production depends critically on additional seeding.

Second, since in this regime the seed is critical, new opportunities arise to control the phase of the generated wakefield and the rate of particle production through manipulation with the seed pulse (see section 8.1).

Note that Eqs. (7.1-7.7) should be applied only for qualitative estimates of the modulation amplification, because for small values of Γ the asymptotic solution is not accurate, whereas for large values of Γ other effects lead to saturation.

7.3 Raman seed amplitude

In the absence of external perturbation or "seed", the Raman Forward Instability may develop from different noise sources for a sufficiently energetic pulse. For example, the leading edge of the laser pulse with finite length can excite a plasma wave [67]. The ionization front of the laser pulse may be considered as a delta function ponderomotive driver that can also create an initial plasma wave [38, 68]. Finally, BRS perturbs the pulse envelope as well as creates noises in the plasma, which can seed RMI [69].

If the energy of the pulse is relatively small, then the number of e-foldings may not be enough to produce a wave of sufficient amplitude from a small perturbation during the interaction time. In this case it is reasonable to introduce a seed - an external perturbation either in plasma or in the pulse envelope - which after amplification might be larger than the natural seeds and produce modulation structure capable of exciting large amplitude waves and accelerating particles. Several seeding mechanisms have been suggested, for example, Raman seed [37, 38] and resonant pre-pulse [70].

Although there is no fundamental difference among the different types of seeds to use, because all approaches serve the same purpose of creating an initial perturbation from which the modulation develops, we use a slightly modified Raman seed in all our numerical simulations. The reason for choosing Raman seed is that it is relatively easy to control and, unlike resonant pulses, suitable for high-density self-modulation regime. Since the instability develops faster at the tail of the pulse we put the seed pulse closer to the head of the main pulse. As a result, the head of the pulse will be pre-modulated at the very beginning. As the tail starts to experience modulation, the whole pulse becomes almost uniformly modulated.

Although the coefficient χ_{s0} from Eq. (7.1) may be associated with various noise sources in the laser-plasma system, the finite length of the pulse is the major contribution to χ_{s0} [67]. To estimate the effect due to the shortness of the pulse, one would proceed to solve the differential equation

$$\left(\frac{\partial^2}{\partial\psi^2} + k_p^2\right)\chi_s = \nabla^2\frac{a^2}{2}. \tag{7.8}$$

Using the standard Green's function method, the solution takes on the general form

$$\chi_s(\psi) = \int_{-\infty}^{\psi} d\xi \nabla^2 \left(\frac{a_0^2(\xi)}{2}\right) G(\psi - \xi). \tag{7.9}$$

In Eq. (7.9), $G(x) = -\frac{1}{k_p}\sin k_p x$, for $x \leq 0$, and 0 elsewhere. To obtain an analytic dependence of χ_{s0} on laser pulse parameters such as the intensity and the pulse-length, used the following pulse-envelope was used in Ref. [67]:

$$a(\xi) = a_0 \sin\frac{\pi\xi}{L}, \text{ for } 0 < \xi < L, \tag{7.10}$$

and $a(\xi) = 0$ elsewhere. This leads to

$$\chi_s = \chi_{s0}\cos\left(k_0\psi - \Theta_0\right), \text{ where } \chi_{s0} = \chi_{s0}^{upperbound}\sin\frac{k_pL}{2}, \tag{7.11}$$

with the upper bound and the rms-average value

$$\chi_{s0}^{upperbound} = \frac{1}{(L/\lambda_p)^2 - 1}\left(\frac{a_0^2}{4}\right), \tag{7.12}$$

$$\chi_{s0}^{avg} \approx \frac{\chi_{s0}^{upperbound}}{\sqrt{2}} \approx \frac{1}{\sqrt{2}}\frac{\lambda_p^2}{L^2}\left(\frac{a_0^2}{4}\right). \tag{7.13}$$

For the Raman seeding case, we parameterize the incident laser field in the region $0 < \xi < L$ by

$$a_{total} = a + a_{seed} = a_0 \sin\left(\frac{\pi\xi}{L}\right)\left[\sin k_0\xi + \frac{a_{0seed}}{a_0}\sin\left((k_0 - k_p)\xi\right)\right], \tag{7.14}$$

where a_{0seed} is the seed amplitude . In the integrand of Eq. (7.9), replacing the function $a_{total}(\xi)^2$ by $2a(\xi)a_{seed}(\xi)$ we obtain

$$\chi_{seed} = \chi_{s0}^{seed} \sin k_p\psi, \text{ with} \tag{7.15}$$

$$\chi_{s0}^{seed} = \pi \left(\frac{L}{\lambda_p}\right) \left(\frac{a_{0seed}}{a_0}\right) \left(\frac{a_0^2}{4}\right). \tag{7.16}$$

The ratio of χ_{s0}^{avg} to χ_{s0}^{seed} characterizes the relative importance of the seed in the modulation development:

$$\frac{\chi_{s0}^{avg}}{\chi_{s0}^{seed}} = \frac{1}{\sqrt{2}\pi} \frac{\lambda_p^3}{L^3} \frac{a_0}{a_{0seed}}. \tag{7.17}$$

The seed becomes important when

$$\frac{a_{0seed}}{a_0} > \frac{1}{\sqrt{2}\pi} \frac{\lambda_p^3}{L^3}. \tag{7.18}$$

Figure 7.1 shows the result of 1D PIC simulations for different values of a_{0seed}/a_0. The graph shows the amplitude of the wakefield at $t = 100\omega_p^{-1}$ for a 100 fs laser pulse with $a_0 = 0.5$ and $\omega/\omega_p = 6$. The point $a_{0seed}/a_0 = 0.015$ at which the wakefield amplitude begins to grow corresponds to $\frac{1}{\sqrt{2}\pi} \frac{\lambda_p^3}{L^3} \frac{a_0}{a_{0seed}} = 1$, thus confirming Eq. (7.18).

Since the process of Raman shifting is not very efficient ($\sim$ 30% in energy) [60], it makes sense to use only a small portion of the laser energy for creation of the seed. For example, production of seed with $a_{0seed}/a_0 = 0.1$ would require splitting approximately 3% of the laser energy for Raman shifting.

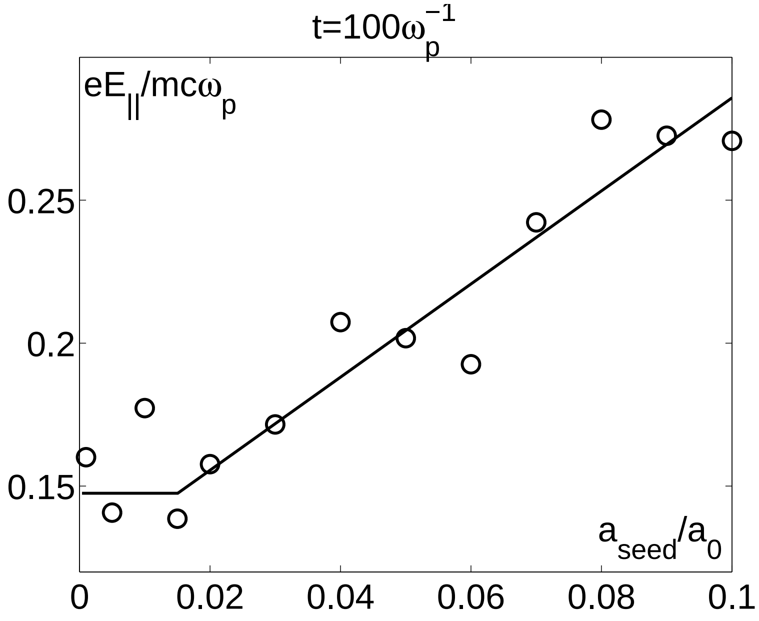

Figure 7.1: Wakefield amplitude at $t = 100\omega_p^{-1}$ as a function of seed amplitude. At $a_{seed}/a_0 = 0.015$ the contribution to χ_{s0} from the seed is equal to the contribution from the leading edge of the pulse.

Chapter 8

Effect of seed parameters on LWFA

8.1 Coherent control with Raman seed

A Raman seed allows us to control the generation of the wakefield by changing the parameters of the seed pulse. Here we present several examples of coherent control of the excited wave.

In Fig. 8.1 we show the results of 1D PIC simulations for different amplitudes of seed pulse ranging from $a_{0seed}/a_0 = 0.0001$ to 0.1. The normalized vector potential in the simulation is $a_0 = 0.5$, laser to plasma frequency ratio is $\omega_0/\omega_p = 6$. Although 1D simulation does not take into account important transverse effects such as diffraction, self-focusing, transverse bunching and transverse wavebreaking, it correctly describes FRS and can be applied for qualitative investigation of pulse and wakefield dynamics at early times. For example, for a spot size of 10 μ and $\lambda = 0.8$ μ the Rayleigh length in the units

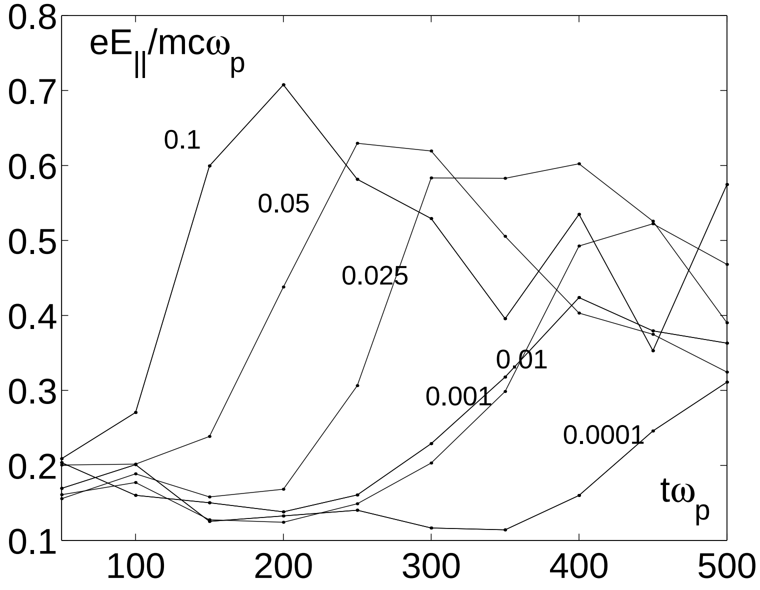

Figure 8.1: Wakefield amplitude for different values of seed as a function of the interaction time.

on the graph would be around 500. Figure 8.1 shows that by changing the amplitude of the seed one can change the time it takes for the wakefield to reach significant value as well as the maximum amplitude of the wakefield and saturation time. On the other hand when seed intensity becomes very small, the effects from the seed are virtually negligible compared to the effects due to the leading edge of the pulse and numerical noise. For example, the value of the wakefield at $t = 250\omega_p^{-1}$ does not vary much for $a_{0seed} \leq 0.01a_0$ (in good agreement with Eq. (7.18)).

Controlling the phase of the wakefield is important if RS LWFA is used as an injector. Since the most energetic electrons are localized around certain phase of the plasma wave, this can be used to synchronize these electrons with

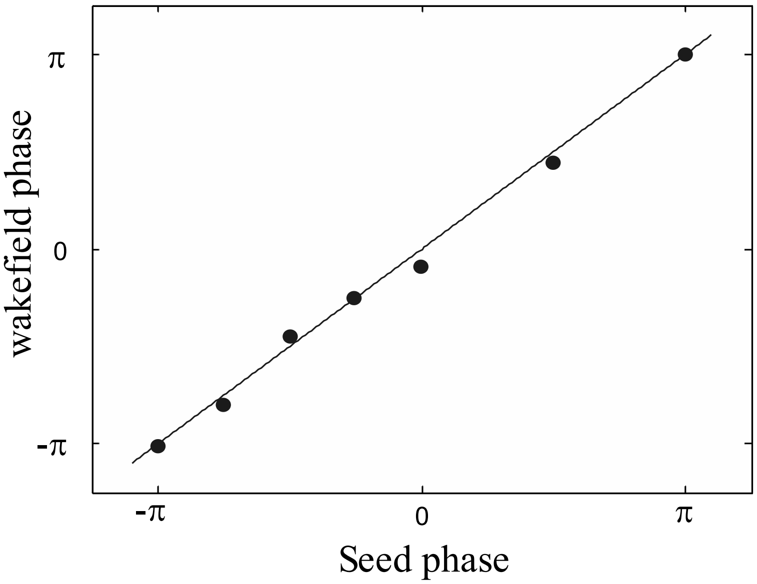

Figure 8.2: Wakefield phase vs. seed phase, $a_0 = 0.5$, $t = 200\omega_p^{-1}$, $a_{0seed}/a_0 = 0.1$. Raman seeding enables control of the phase of the excited plasma wave.

the accelerating structure in the second stage of the acceleration.

Moreover, although in the 2D simulations presented in this work the excited plasma wave amplitude is large enough to trap the background electrons, which have been preheated by BRS (see Chapter 9), lower amplitude pulses are capable of exciting plasma waves without particle trapping. Such wakefields can be used to accelerate externally injected particles or in multistage accelerators. In this regime Raman seed not only enhances the modulation but also can be used to control the phase of the excited wakefield.

Figure 8.2 shows the phase of the plasma wave as a function of the phase difference between the main pulse and the seed pulse. This dependence is virtually linear, in contrast to SM-LWFA, where the modulation grows from the noise, which results in indeterminate phase with random shot-to-shot fluctuations. Suppose, we would like to make a two stage accelerator and for this purpose we take two laser pulses with a fixed phase difference and send them into two consecutive gas jets. After electrons are accelerated by the wakefield in the first jet, they enter into the second one. In order to control the phase difference between the wakefields in the two jets we split a small fraction of one of the pulses and Raman shift it in a Raman active crystal. Then we split the shifted pulse again into two seed pulses and combine each of them with one of the main pulses. Although, the phase of the shifted light is random with respect to the phase of the main pulses, the difference between the beating and, therefore, the wakefield phases in the two jets will be a controlled parameter.

8.2 Sensitivity of Raman seeding to frequency mismatch

In the beat-wave accelerator the pulses with frequencies ω_0 and $\omega_0 - \omega_p$ have comparable amplitudes. The superposition of the two waves creates a beating pattern, which may be viewed as a train of resonant pulses. In the Raman seeded LWFA, on the other hand, $a_{0seed} \ll a_0$ and the modulation structure develops by a self-organizing process of Raman scattering. Consider two laser pulses with a relative frequency difference not exactly equal to ω_p. In the seeding case, only those components of the initial perturbation will be amplified which have the correct phase. For the beat-wave case the wakefield excited is

$$\phi = -\frac{(k_1 - k_2)^2}{4k_p}\psi\frac{\sin\left((k_1 - k_2 - k_p)\psi/2\right)}{(k_1 - k_2 - k_p)\psi/2}\sin\left((k_1 - k_2 + k_p)\psi/2\right), \qquad (8.1)$$

where k_1 and k_2 are the wave number of the two pulses. Here we assumed a rectangular envelope for the pulses. The growth of the wakefield amplitude is sensitive to the phase mismatch, which will increase with the length of the pulse and is given by:

$$\Delta\varphi = (k_1 - k_2 - k_p)L, \tag{8.2}$$

where L is the length of the pulse. The amplitude of the wakefield grows linearly with ψ if $\Delta\varphi \ll 1$. Otherwise, the wakefield excited by different parts of the pulse will be out of phase and will partially cancel each other.

In order to demonstrate the effect of the frequency mismatch on the particle acceleration, we perform a series of 1D particle-in-cell simulations with different frequencies of the second pulse. In the seeded case the main pulse has $a_0 = 0.5$, the seed pulse has $a_{0seed}/a_0 = 0.1$. The pulses in the beatwave case have equal intensity and their combined energy is equal to the energy of the main pulse in the seeded case, i.e. $a_0' = a_0'' = 0.35$. The interaction time is $500\omega_p^{-1}$. Figure 8.3 shows the dependence of the maximum particle energy on the mismatch for the case of the Raman seeded and beatwave LWFA. Note that Raman seeded wakefield acceleration is less sensitive to the frequency mismatch.

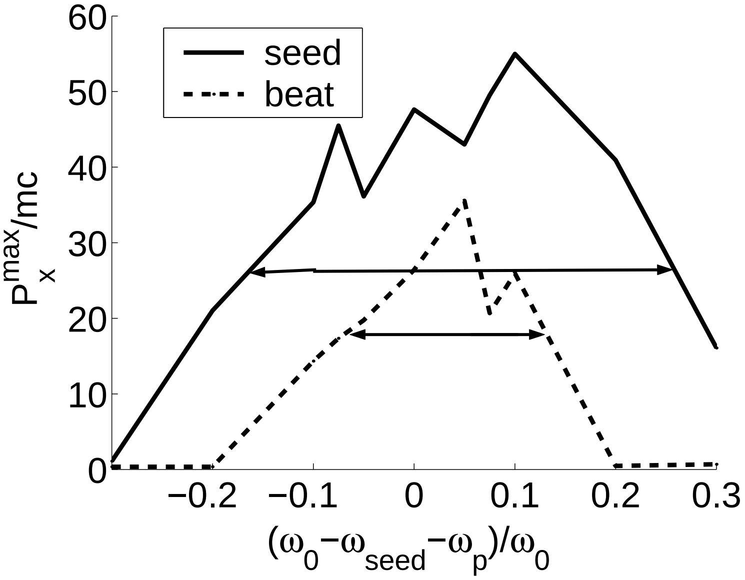

Figure 8.3: Maximum electron longitudinal momentum as a function of frequency mismatch for Raman seeded (solid line) and beatwave (dashed line) cases.

Chapter 9

Particle production in RS and SM LWFA

The results of 1D and 2D simulations indicate the presence of particle trapping and acceleration by a plasma wave, which is far from cold plasma wavebreaking, when the normalized electrostatic potential is $\phi = e\Phi/mc^2 \sim 0.5$. A 1D nonlinear plasma wave breaks when [71] $\phi = (\gamma_p^2 - 1)/\gamma_p \gg 1$, where $\gamma_p = \omega/\omega_p$ is the relativistic factor of a particle resonant with the wave. It is noteworthy that a 2D or 3D plasma wave eventually breaks at any wave amplitude [72]. However, in our simulations we observe particle trapping in 1D. This indicates that the mechanism of injection of the particles into the acceleration phase is different from transverse wavebreaking. It turns out that the appearance of the particles that are coherent with the plasma wave is the result of the fine-scale wavebreaking caused by Backward Raman Scattering (BRS) [73, 74, 75]. During this process, a wave (ω, k) decays into a scattered wave ($\omega - \omega_p$, $-k$) and a plasma wave (ω_p, $2k$) [2]. Since this process is unstable, the amplitude of the short-scale plasma wave grows fast until wavebreaking, which occurs at significantly lower amplitude $\phi = 1/2\gamma_p$ than the long-scale wakefield with wavenumber $k_p \approx \omega_p/c$. The electrons, which lose the coherence with the wave due to wavebreaking, have characteristic velocity equal to the phase velocity of the short-scale plasma wave $v_{\rm ph} = \omega_p/2k = c/2\gamma_p = 0.08c$. The simulations show that the actual momentum spread resulting from this wavebreaking can be several times this number (see Fig. 9.1). Wavebreaking leads to plasma heating. When the Debye length becomes comparable to the wavelength of the excited plasma wave, the plasma wave is then strongly damped, and the process of BRS is suppressed.

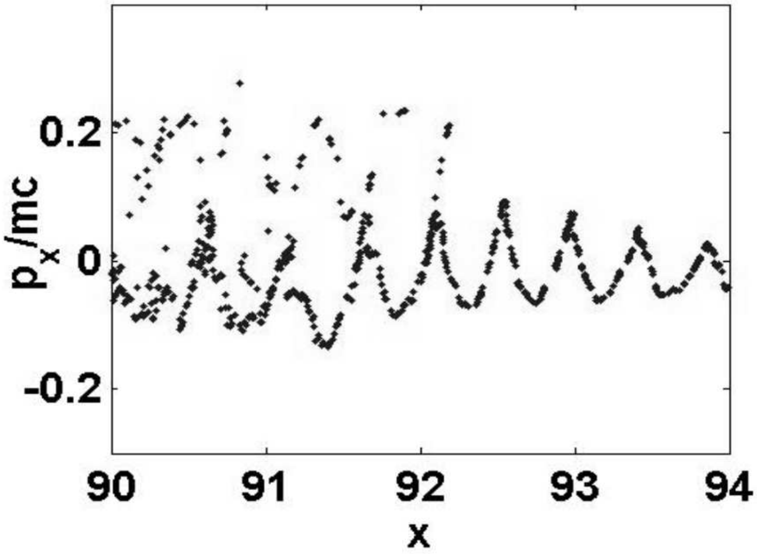

Figure 9.1: Wavebreaking due to Backward Raman Scattering. 1D simulation with $a_0 = 0.35$ and no seed. The graph shows the longitudinal projection of the phasespace. For lower values of x, the wave gets completely destroyed and the particle momenta reach the values of $\sim 0.4mc$.

The trapping mechanism must be explained in terms of the particle dynamics in the long-scale plasma wave. A motion of a particle in a cold plasma wave is described by a Hamiltonian [71]:

$$H(\beta, \psi) = \gamma(1 - \beta\beta_p) - \phi(\psi), \tag{9.1}$$

where $\psi = x - v_g t$, v_g is phase velocity of the long-scale plasma wave (approximately equal to the group velocity of the laser pulse), $\beta_p = v_g/c$, β is the normalized particle velocity, γ is the particle relativistic factor. H is normalized electron energy in the wave frame. The trajectory of the particle in the cold wave is determined by the condition, that at the turning point of the oscillation ($\beta = 0$) the restoring force on the particle is maximum. This condition can be written as

$$\begin{cases} H(\beta, \psi) = 1 - \phi(\psi^*), \\ \phi''(\psi^*) = 0. \end{cases} \tag{9.2}$$

The trajectories of the particle, which are trapped in the wave are separated from the rest of the particles by the separatrix, which is determined by the condition that at the maximum of the potential energy $-\phi$ there is a unique solution for β or

$$H(\beta, \psi) = \gamma_p^{-1} - \phi_{min} \tag{9.3}$$

For simplicity, we assume that the potential is sinusoidal. Figure 9.2 shows the trajectories in the (ψ, p_x) phasespace given by Eqs. (9.2) and (9.3) with the amplitude $\phi_0 = 0.5$. Figure 9.3 shows the minimum of the difference between the two curves as a function of the wakefield amplitude. The trapping occurs when the momentum spread provided by short-scale wavebraking is sufficient for transferring a particle from the wave into the trapped region.

Note, that the wave is sinusoidal only in the low amplitude region $\phi_0 \ll 1$. For large values of ϕ_0 the differential equation for a nonlinear plasma wave must be solved [2]. Still the present analysis gives a qualitative understanding of the electron trapping at low values of ϕ_0.

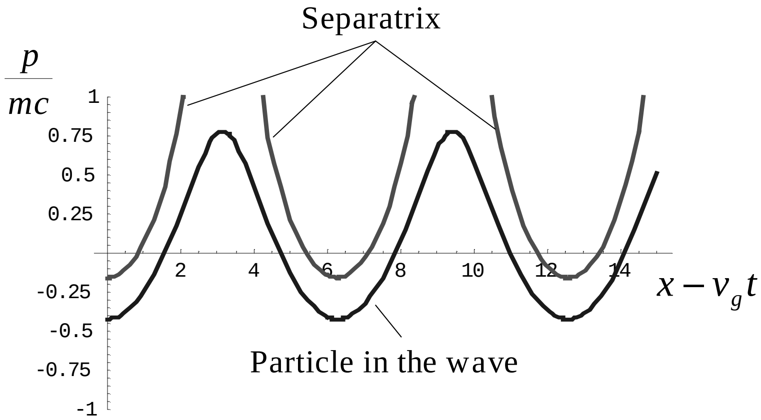

Figure 9.2: Trajectory in the phase space of a particle in the wave given by $\phi = 0.5\cos(k_p x - \omega_p t)$ and the particle on the separatrix. Preheating caused by Backward Raman Scattering perturbes the trajectories of the particles in the wave and allows them to reach the separatrix (become trapped).

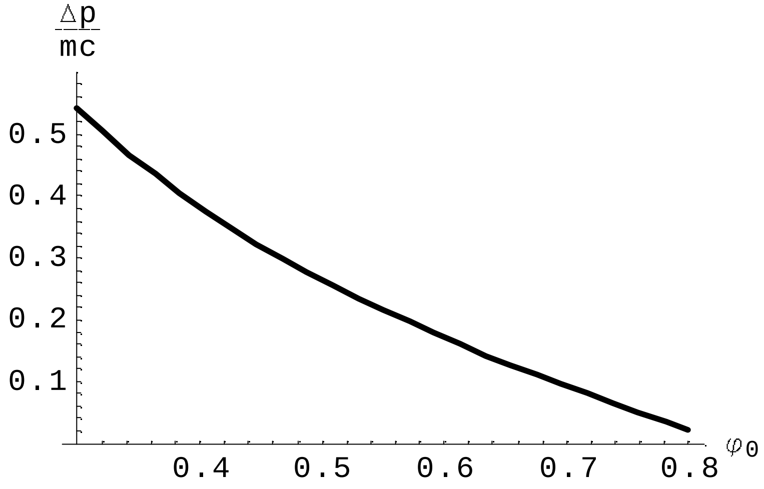

Figure 9.3: The minimum difference between momenta given by Eqs. (9.2) and (9.3) as a function of the wakefield amplitude.

Chapter 10

2D PIC simulations

In this chapter, we study wakefield creation and particle acceleration using Raman seed and self-modulation for relatively low energy pulses. Low energy pulses require a very tight focus in order to obtain relativistic intensities. Proper treatment of two dimensional effects, such as diffraction, relativistic self-focusing, transverse modulation, and transverse wavebreaking is needed for quantitative description of LWFA. The standard tool suitable for treating 2D effects is a 2D particle-in-cell (PIC) code. Our simulations are done in slab geometry, i.e., the plasma and the laser filed is uniform in the direction along the laser magnetic field. We use versatile VORPAL code [43, 44, 45] in the particle-in-cell mode (the code also supports fluid and Vlasov description of plasma). In the simulation, the pulse enters the plasma from the right boundary. When it reaches the middle of the simulation box, the simulation window is switched to the pulse frame. This reduces the simulation time, since only the plasma in the region of the laser pulse is simulated. The plasma behind the laser pulse is removed and the new plasma in front of the pulse is added as time progresses.

10.1 Raman seeded wakefield acceleration

Experiments indicate that energetic electron production for SM-LWFA occurs only when the laser power exceeds the critical power $P > P_c$ [29]. We will first simulate unseeded LWFA at the critical power to demonstrate the importance of self-focusing in SM regime. Then we will show how the introduction of the Raman seed enhances the modulation and leads to particle production.

Consider a smooth laser pulse of amplitude $a_0 = 0.5$, spot size $w = 6\ \mu$, wavelength $\lambda = 0.8\ \mu$, and duration $\tau = 125$ fs. This pulse is at critical power $P \approx P_c$ for $\omega/\omega_p = 6$ so the effects of diffraction is compensated by relativistic self-focusing.

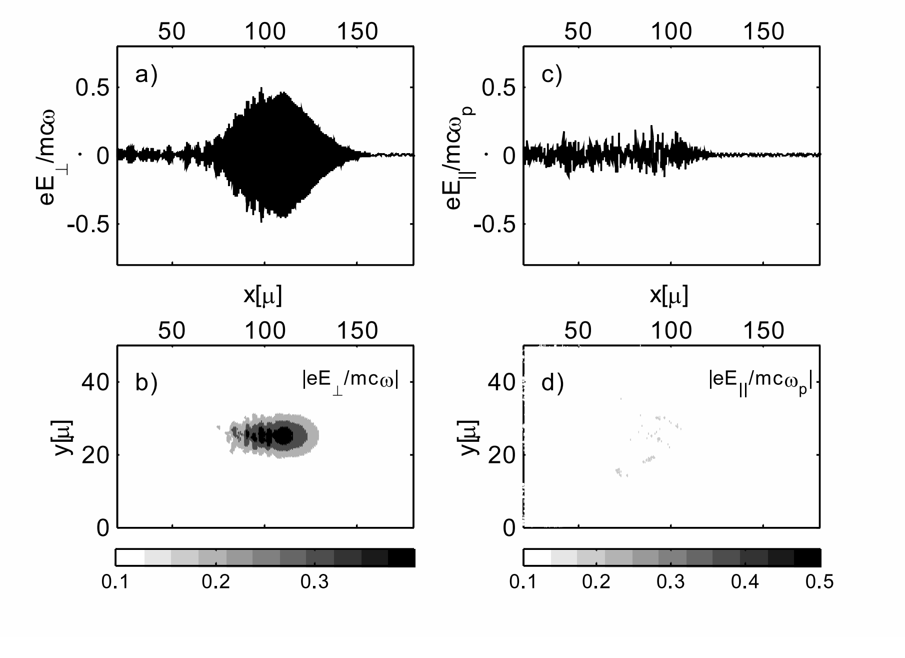

Figure 10.1: No seed, $a_0 = 0.5$, $t = 200\omega_p^{-1} = T_R$. Graphs a and b show the pulse amplitude. Graphs c and d show the wakefield.

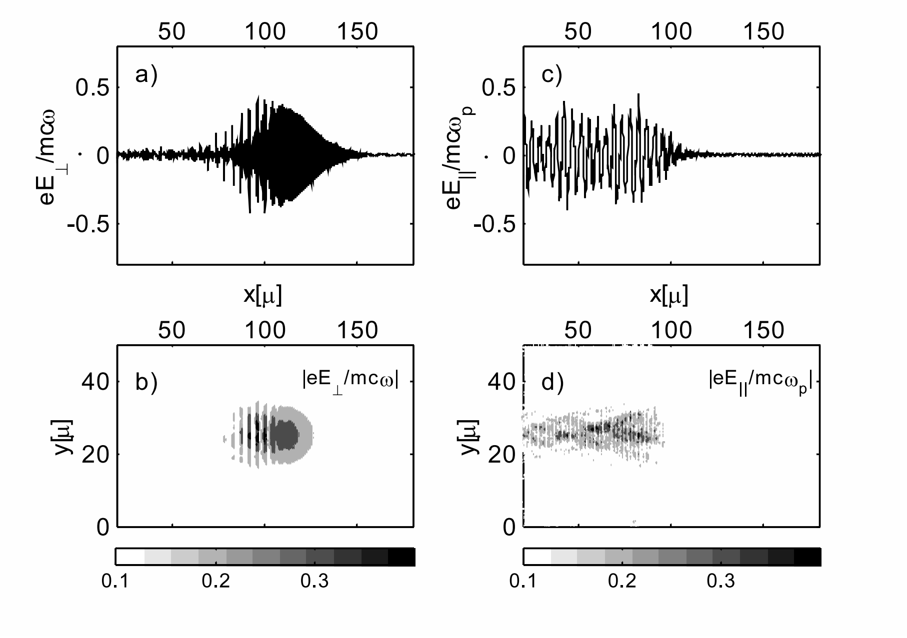

Figure 10.2: No seed, $a_0 = 0.5$, $t = 400\omega_p^{-1} = 2T_R$. Graphs a and b show the pulse amplitude. Graphs c and d show the wakefield.

From Eq. (7.3) we find that after one Rayleigh length $\Gamma \approx 7$ and $e^{\Gamma_{3D1}} \approx 1000$. This gain is not enough to develop significant modulation for a smooth noiseless pulse. Fig. 10.1 shows the results of 2D PIC simulation for such a pulse at $t = T_R$, i.e. after the pulse has traversed 1 Rayleigh length in plasma. Figure 10.1a shows the pulse-field along the propagation axis, i.e. at $y = 25\ \mu$. Notice that for this no-seed case, there is very little modulation. The contour plot showing $x-y$ dependence of the pulse-field is presented in Fig. 10.1b. The corresponding wakefield E_x is shown in Fig. 10.1c and Fig. 10.1d. As expected, due to the lack of pulse modulation, there is very little wakefield excitation, and no accelerated electrons. Figure 10.2 shows the corresponding pulse and wakefield at $t = 2T_R$ ($e^{\Gamma_{3D1}} \sim 10^4$). A comparison between Fig. 10.1a and

Fig. 10.2a indicates that after having covered the second Rayleigh length, the pulse has acquired noticeable modulation near the end of the pulse, i.e. in the range $x \sim 70 - 100\ \mu$, which leads to the generation of wakefield as illustrated in Fig. 10.2c and Fig. 10.2d. Figure 10.2c shows that the wakefield excitation along the beam axis which begins from the center of the pulse is extending to the small x region with an average amplitude of about ($\sim 0.2\omega_p mc/e$). The wakefield excitation here is not strong enough to accelerate significant number of electrons. Only 0.002nC of hot electrons (with kinetic energy > 1 MeV) per pulse were produced. Figure 10.2d shows that the wakefield has the maximum amplitude at the propagation axis.

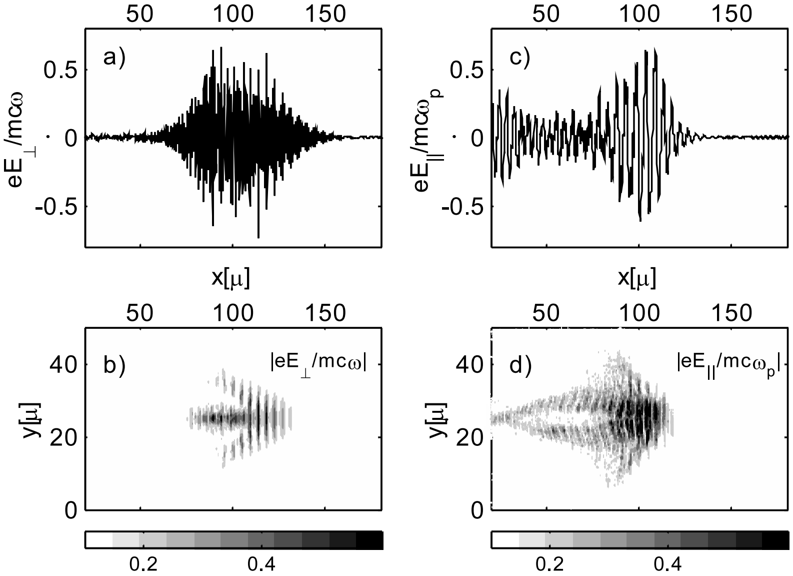

Figure 10.3: Seed, $a_0 = 0.5$, $t = 500\omega_p^{-1} = T_R$. Graphs a and b show the pulse amplitude. Graphs c and d show the wakefield.

Although Γ is not very large in this example, as alluded to in Sec. 7.2, Raman seed makes the initial perturbation finite, which speeds up the process of pulse modulation. For the same parameters as above, we have performed the simulation of the Raman seeded pulse, with seed pulse 1% in intensity of the main pulse. The simulation results at $t = T_R$ are given in Fig. 10.3. Fig. 10.3*a* shows the laser field along the beam axis. The pulse has acquired a significant modulation. Fig 10.3*b* shows that while the main pulse along the beam axis is well focused, a subpulse is developed on each side, which suggests the presence of the filamentation process. The corresponding wakefield excitation is illustrated in Fig. 10.3*c* and 10.3*d*. The wakefield along the propagation axis is shown in Fig. 10.3*c*. Notice the presence of large wakefield excitation with amplitude $\sim 0.6\omega_p mc/e$ which begins near the center of the pulse. This large wakefield is stretched out by about one-third of the pulse length. Then a wavebreak occurs which leads to the destruction of the wakefield. Figure 10.3*d* shows the wakefield excitation is trailing behind the pulse with a "wavebreak" occurring near the beam axis behind the pulse. This is a 2D transverse wavebreaking, which leads to a significant reduction of particle energy of the accelerated electrons compared to that for the 1D case.

At $t = T_R$, the total charge of hot electrons produced is 0.62 nC, which is produced by a Raman-seeded pulse, with pulse energy equal to 38 mJ. This is to be compared to recent experimental results [29] where $\sim$ 1 nC hot electrons is generated by 500 mJ pulse. The properties of the electron bunch are shown in Fig. 10.4. Figure 10.4*a* shows the y-distribution of electrons with kinetic energy greater than 1 MeV. Here the y-deviation defined by $\langle \Delta y \rangle = \sqrt{\bar{y^2} - \bar{y}^2} \approx 4\ \mu$, which is 70% of the spotsize. The outgoing beam is still reasonably well collimated. It turns out as time further increases the y-deviation begins to increase noticeably. At 2-Rayleigh length, the y-

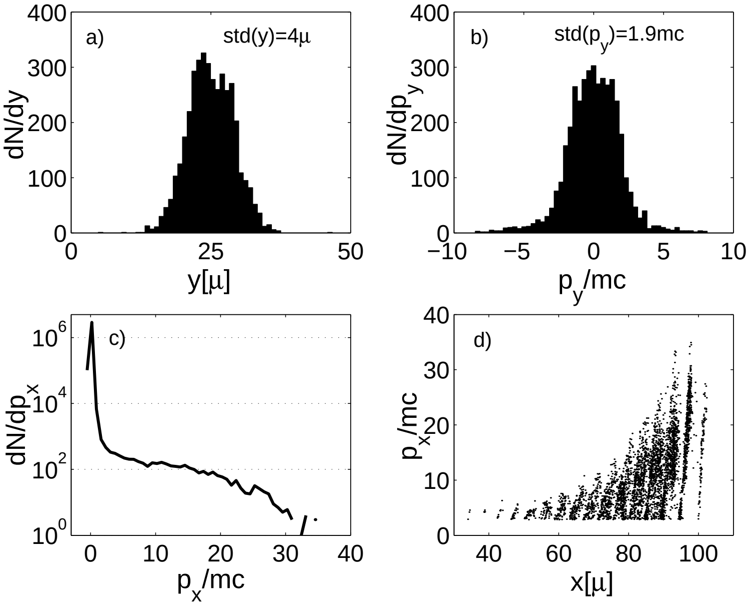

Figure 10.4: Seed, $a_0 = 0.5$, $t = 200\omega_p^{-1} = T_R$. Transverse *a*) spatial and *b*) momentum distribution for electrons with kinetic energy over 1 MeV. *c*) longitudinal momentum distribution and *d*) longitudinal projection of the phase space.

deviation increases to twice the spotsize. Here we will confine our attention to the 1-Rayleigh length case. Figure 10.4*b* shows the y-momentum distribution which leads to an angular deviation of $\langle\theta\rangle \approx 12°$. The longitudinal momentum distribution is shown in Fig. 10.4*c*. There are two distinct features which differ from the corresponding 1D case [35]. First, for the same maximum wakefield amplitude, the maximum value of the longitudinal momentum p_x^{max} obtained here is about half of that of the 1D case. Second, the dN/dp_x plot here has a rapid fall compared to a relatively flat behavior for the 1D case. Both features may be attributed, at least in part, to the occurrence of the aforementioned wavebreaking phenomena which occur in the 2D case we are considering. Other effects affecting the properties of the particle beam in 2D are particle beam defocusing by transverse component of the ponderomotive force of the laser and by the transverse electrostatic field of the wakefield (in the first quarter of the 2D plasma wave the electron beam is both accelerated and focused, whereas in the second half it is accelerated but *defocused*). The x-phase space plot is shown in Fig. 10.4*d*. Notice that the high momentum electrons concentrated in $x = 80 - 100\ \mu$ region are results of the acceleration by the corresponding large wakefield in the same x-region (see Fig. 10.3*c*).

10.2 Raman seeded LWFA in a channel

In this section we investigate the possibility of Raman seeded LWFA for subcritical pulses. The reason for this is that, first, subcritical pulses are less subject to the transverse processes, which lead to the pulse destruction such as filamentation and transverse modulation. This allows higher degree of control compared to the supercritical pulses. Second, low energy pulses are more accessible and can be produced at higher repetition rate.

As we discussed above, SM-LWFA is not possible for subcritical pulses. In the non-seeded example from the previous section, we considered a pulse at critical power. It generated a few relativistic electrons only at $t = 2T_R$. This was possible only because of the relativistic self-focusing. The pulse of a smaller power would neither have modulated within one Rayleigh length nor have enough intensity beyond this because of diffraction.

In order to overcome this problem with low intensity pulses described above, we can utilize another mechanism preventing diffraction instead of relativistic self-focusing, namely plasma channel guiding. We simulate a pulse,

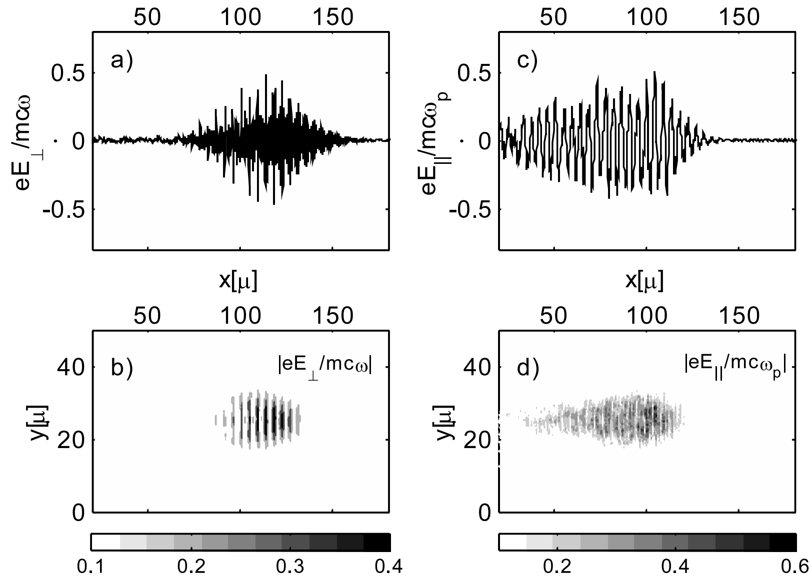

Figure 10.5: Seed, $a_0 = 0.35$, channel, $t = 2.5T_R$. Graphs a and b show the pulse amplitude. Graphs c and d show the wakefield.

which enters the simulation box from the left boundary, after 0.5 Rayleigh lengths it reaches the channel. The channel is chosen such that $1 - P/P_c - \Delta n/\Delta n_c = 0$, where P is the power of the pulse, P_c is the critical power, $\Delta n_c = (\pi r_e r_0^2)^{-1}$ is the critical channel depth, Δn is the channel depth, that is, the density in a channel is given by $n_0 + \Delta n r^2/r_0^2$, and r_0 is the laser spotsize. Under such conditions, the pulse propagates in the channel distortion-free [76]. Figure 10.5 shows the laser field and the wakefield at $t = 2.5T_R$ (two Rayleigh lengths inside the channel) for the Raman-seeded pulse in the channel. Figure 10.5a shows that the pulse acquired significant modulation despite its low intensity. The modulation is almost uniform along the pulse due to the proper placement of the seed pulse. Figure 10.5b shows the the transverse structure

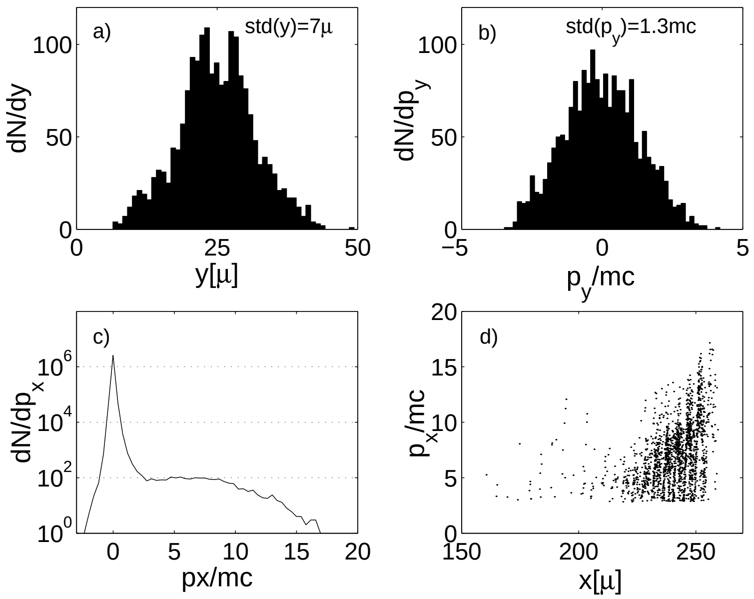

Figure 10.6: Seed, $a_0 = 0.35$, channel, $t = 2.5T_R$. Transverse *a*) spatial and *b*) momentum distribution for electrons with kinetic energy over 1 MeV. *c*) longitudinal momentum distribution and *d*) longitudinal projection of the phase space.

of the pulse is well preserved as well. The reason for this is that the effects of 2D self-modulation and filamentation are greatly reduced when $P < P_c$. Figure 10.5*c* and Fig. 10.5*d* show the corresponding wakefield in the channel. The amplitude of the wakefield is significant. Nevertheless, the wave does not break as in Fig. 10.3*d*. Figure 10.6 shows the properties of the electron bunch of 0.33 nC generated by the seeded pulse in the channel. Figure 10.6*a* and Fig. 10.6*b* show the transverse coordinate and momentum distributions for the particles with kinetic energies greater than 1 MeV. Although the maximum particle energy is lower than in the higher intensity case presented in Fig. 10.4 and the transverse size of the beam is larger, the beam is still collimated and the total charge in the beam is around nC range desirable for practical applications. Figure 10.6c shows the longitudinal momentum distribution of all the particles in the simulation. Figure 10.6d shows the $x - p_x$ projection of the phase space.

As a summary, the Table 10.1 shows the number of relativistic particles produced in different simulations.

Table 10.1: Total charge of electrons with kinetic energy > 1 MeV for three different simulations.

a_0	0.35 channel	0.5 seed	0.5 no seed
$t = T_R$	0	0.62 nC	0
$t = 2T_R$	0.33 nC	0.58 nC	0.002 nC

Chapter 11

Conclusion

We have investigated the possibility of controlled wakefield excitation and particle acceleration by low energy Raman seeded pulse in the self-modulated regime. Our 2D PIC simulations show that significant pulse modulation is possible if the initial perturbation provided by a seed pulse, when multiplied by e^{Γ}, is of the same order as the main pulse; the excited wake then traps and accelerates background electrons to $10-20$ MeV.

Raman seeded acceleration has some distinct advantages over conventional high amplitude self-modulation accelerators. First, the resulting modulation structures and the wakefields turn out to be very clean and can be controlled by seed pulse parameters. The possibility of coherently controlling the wakefield can be especially important for beam shaping or in multistage accelerators, when the external particle injection is used. Second, our simulations indicate that a 38 mJ Raman seeded pulse can excite very strong wakefield that can trap and accelerate 0.6 nC of multi-MeV electrons. With the conservative assumption that the laser system can sustain in average 10 W of radiated power, we conclude that acceleration is possible at $f_{rep} = 260$ Hz.

By contrast, most wakefield experiments in the self-modulation regime were done with single shot $f_{\mathrm{rep}} \ll 1$ Hz, up to the maximum repetition rate 10 Hz. High repetition rate means large average current, which is important in many applications, such as radiation oncology [35] or isotope production [29]. In particular our simulation of a Raman-seeded, channeled laser pulse with only $a_0 = 0.35$ shows that a pulse at half critical power is capable of exciting a plasma wave and accelerating 0.33 nC to relativistic velocities.

Our 2D simulations show that subcritical, controlled Raman-seeded wakefield excitation continues to occur at main pulse intensities even lower than the examples presented above, although, very few particles are trapped during wavebreaking. Nevertheless, external injection might be used in this regime to enable RS-LWFA at even higher repetition rates.

Appendix

Numerical implementation of LEM code

Lase Electromagnetic code is designed for simulation laser propagation through plasma and wakefield excitation. The laser is modeled using quasi-static approximation. The plasma is model as a relativistic fluid. The closed system of equation then is given by [77]

$$\begin{aligned}&\left(1-\tfrac{\nabla_\perp^2}{k_p^2\rho}+(\tfrac{\nabla_\perp\rho}{k_p^2\rho^2})\cdot\nabla_\perp\right)\tfrac{\partial^2\psi}{\partial\xi^2}=\\&\left(1-\tfrac{\nabla_\perp^2}{k_p^2\rho}+(\tfrac{\nabla_\perp\rho}{k_p^2\rho^2})\cdot\nabla_\perp\right)k_p^2\rho u_z+\\&\nabla_\perp\cdot\left(\tfrac{1}{k_p^2}\tfrac{\partial 1/\rho}{\partial\xi}\nabla_\perp\tfrac{\partial\psi}{\partial\xi}+\tfrac{u_z}{\rho}\nabla_\perp\rho\right)\end{aligned} \tag{.1}$$

$$\rho=\frac{1}{1+\psi}(\rho^0+\frac{1}{k_p^2}\nabla_\perp^2\psi) \tag{.2}$$

$$u_z=\gamma-\psi-1 \tag{.3}$$

$$u_\perp = \frac{1}{k_p^2\rho}\frac{\partial}{\partial\xi}(\nabla_\perp\psi) \tag{.4}$$

$$\gamma = 1 + \frac{u_\perp^2 + |\mathbf{a_f}|^2/2 + \psi^2}{2(1+\psi)} \tag{.5}$$

$$\left(\nabla_\perp^2 + \frac{2\imath k}{c}\frac{\partial}{\partial\tau} + \frac{2}{c}\frac{\partial^2}{\partial\xi\partial\tau}\right)\mathbf{a_f} = k_p^2\rho\mathbf{a_f} \tag{.6}$$

In these equations $\psi = \phi - a_z$, where ϕ is normalized scalar potential, a is normalized vector potential, $\mathbf{a_f}$ is an envelope of the laser pulse, $\mathbf{u}$ is normalized momentum, $\rho = n/n_0\gamma$ is normalized density, $\gamma = \sqrt{1+|\mathbf{u}|^2}$ is relativistic factor.

To solve equations .1-.6 numerically lets put take unit of length $\frac{1}{k_p}$ and make substitutions:

$$V = \frac{1}{\rho} \tag{.7}$$

$$\Gamma = \frac{\partial^2\psi}{\partial^2\xi} \tag{.8}$$

$$A = k_p^2\rho u_z \tag{.9}$$

$$B = \frac{1}{k_p^2}\frac{\partial 1/\rho}{\partial\xi}\nabla_\perp\frac{\partial\psi}{\partial\xi} + \frac{u_z}{\rho}\nabla_\perp\rho \tag{.10}$$

Then equations become

$$\left(1 + V\nabla_\perp^2 - (\nabla_\perp V)\cdot\nabla_\perp\right)(\Gamma - A) = \nabla_\perp \cdot B \tag{.11}$$

$$\Gamma = \frac{\partial^2\psi}{\partial^2\xi} \tag{.12}$$

$$A = \frac{V^2(\frac{\partial}{\partial\xi}\nabla_\perp\psi)^2 + |\mathbf{a_f}|^2/2 - 2\psi - \psi^2}{2V(1+\psi)} \tag{.13}$$

$$B = \frac{\partial V}{\partial\xi}\nabla_\perp\frac{\partial\psi}{\partial\xi} - A\nabla_\perp V \tag{.14}$$

For cartesian coordinates equations look like

$$\Gamma + V\Gamma_{xx} - V_x\Gamma_x = A + VA_{xx} - V_xA_x + B_x \tag{.15}$$

$$\Gamma = \frac{\partial^2\psi}{\partial^2\xi} \tag{.16}$$

$$A = \frac{V^2\psi_{x\xi}^2 + |\mathbf{a_f}|^2/2 - 2 - \psi^2}{2V(1+\psi)} \tag{.17}$$

$$B = V_\xi\psi_{x\xi} - AV_x \tag{.18}$$

$$V = \frac{1+\psi}{\rho^0 + \psi_{xx}} \tag{.19}$$

$$\left(\nabla_\perp^2 + 2\imath\gamma_p\frac{\partial}{\partial\tau} + 2\frac{\partial^2}{\partial\xi\partial\tau}\right)\mathbf{a_f} = \frac{\mathbf{a_f}}{V} \tag{.20}$$

Initial conditions

Initial conditions are the following:

$$\mathbf{a_f}(t=0) = a_0 e^{-\frac{(\xi-\xi_0)^2}{2\sigma_\xi^2}} e^{-\frac{x^2}{2\sigma_x^2}}$$

$$V(t=0) = \frac{1}{\rho^0}$$

Boundary conditions imposed are:

$$\psi(\xi=0) = 0$$

$$\frac{\partial\psi}{\partial\xi}(\xi=0) = 0$$

For x either periodic or mirror boundary conditions are assumed.

Finding ψ

Index i corresponds to x, index j to ξ. We start at $\xi = 0$ since we can take advantage of boundary condition. At $j = 0$ and $j = 1$ ψ is equal to 0. We start with $j = 1$, all quantities at j and $j-1$ are known. So we can find Γ for all i-s. Then integrate in ξ to find ψ and increase j.

For given j

$$(\psi_{x\xi})^i_j = \frac{\psi^{i+1}_j + \psi^{i-1}_{j-1} - \psi^{i-1}_j - \psi^{i+1}_{j-1}}{2\delta x \delta \xi} \tag{.21}$$

$$A^i_j = \frac{(V^i_j)^2((\psi_{x\xi})^i_j)^2 + |\mathbf{a_f}{}^i_j|^2/2 - 2 - (\psi^i_j)^2}{2V(1+\psi^i_j)} \tag{.22}$$

$$(V_x)^i_j = \frac{V^{i+1}_j - V^{i-1}_j}{2\delta x} \tag{.23}$$

$$(V_\xi)^i_j = \frac{V^i_j - V^i_{j-1}}{\delta x} \tag{.24}$$

$$B^i_j = (V_\xi)^i_j(\psi_{x\xi})^i_j - A^i_j(V_x)^i_j \tag{.25}$$

Equation .15 can be solved using tridiagonal sparse matrix solver routine

$$\Gamma^{i+1}a^i_1 + \Gamma^i a^i_0 + \Gamma^{i-1}a^i_{-1} = A^{i+1}a^i_1 + A^i a^i_0 + A^{i-1}a^i_{-1} + B^i_x \tag{.26}$$

where

$$a^i_1 = -\frac{V^i}{\delta x^2} - \frac{V^i_x}{2\delta x} \tag{.27}$$

$$a^i_0 = 1 + \frac{2V^i}{\delta x^2} \tag{.28}$$

$$a^i_{-1} = -\frac{V^i}{\delta x^2} + \frac{V^i_x}{2\delta x} \tag{.29}$$

Now knowing Γ we can find ψ at $j+1$

$$\psi_{j+1}^{i} = 2\psi_{j}^{i} - \psi_{j-1}^{i} + \Gamma_{j}^{i}\Delta y^{2} \tag{.30}$$

Finding V

$$V_{j}^{i} = \frac{1+\psi_{j}^{i}}{\rho^{0} + \frac{\psi_{j}^{i+1} - 2\psi_{j}^{i} + \psi_{j}^{i-1}}{\delta x^{2}}} \tag{.31}$$

Envelope evolution

Lets transform everything to fourier space using FFT. Let $\mathbf{a_f} = a e^{\imath(k\cdot r - \omega t)}$. Then equation .6 becomes

$$\left(-k_{\perp}^{2} + 2\imath(\gamma_p + k_{\parallel})\frac{\partial}{\partial t}\right) a = R \tag{.32}$$

where $R(x,z) = \frac{a(x,z)}{V(x,z)}$.

Thus explicit formula for time integration of the envelope is:

$$\frac{\partial a}{\partial t} = -\imath \frac{R + k_{\perp}^{2} a}{2(\gamma_p + k_{\parallel})} \tag{.33}$$

Bibliography

[1] G. Mourou and D. Umstadter. Development and applications of compact high-intensity lasers. *Phys. Fluids B*, 4(7), 1992.

[2] E. Esarey, P. Sprangle, J. Krall, and A. Ting. Overview of plasma-based accelerator concepts. *IEEE Trans. Plasma Science*, 24:252–288, 1996.

[3] T. Ditmire, J. Zweiback, V. P. Yanovsky, T. E. Cowan, G. Hays, and K. B. Wharton. Nuclear fusion from esplosions of femtosecond laser-heated deuterium clusters. *Nature*, 398:489–492, 1999.

[4] R. Lichters, J. Meyer ter Vehn, and A. Pukhov. Short-pulse laser harmonics from oscillating plasma surface driven at relativistic intensity. *Phys. of Plasmas*, 3(9):3425, 1996.

[5] P. Gibon. High-order deneration in plasmas. *IEEE J. of Quant. Elec.*, 33(11):1915, 1997.

[6] S. V. Bulanov, N. M. Naumova, and F. Pegoraro. Interaction of an ultra-short, relativistically strong laser pulses with an overdense plasma. *Phys. of Plasmas*, 1(3):745, 1994.

[7] K. Nakajima, J. K. Koga, and K. Nakagawa. Relativistic ion acceleration by ultraintense laser interactions. *Adv. Accel. Concepts*, 569:97–104, 2000.

[8] A. Maksimchuk, S. Gu, K. Flippo, and D. Umstadter. Forward ion acceleration in thin films driven by a high-intensity laser. *Phys. Rev. Lett.*, 84(18):4108, 2000.

[9] The national ignition facility:an overview. *Energy&Technology Review*, 1994.

[10] T. Ditmire. *Contemporary Physics*, 38:315, 1997.

[11] T. Ditmire, T. Donnelly, A. M. Rubenchik, R. W. Falcone, and M. D. Perry. Interaction of intense laser pulses with atomic clusters. *Phys. Rev. A*, 53:3379–3402, 1996.

[12] Y. Kishimoto, T. Masaki, and T. Tajima. *Physics of Plasmas*, 9:589, 2002.

[13] T. Ditmire, E. Springate, J. W. G. Tisch, Y. L. Shao, M. B. Mason, N. Hay, J. P. Marangos, and M. H. R. Hutchinson. Explosion of atomic clusters heated by high-intensity femtosecond laser pulses. *Phys. Rev. A*, 57(1):369, 1998.

[14] A. McPherson, B. D. Thompson, A. B. Borisov, and C. K. Rhodes. Multiphoton induced x-ray emission at 4-5kev from xe atoms with multiple core vacancies. *Nature*, 370:631–634, 1994.

[15] S Ter-Avetisyan, M. Schnürer, H. Stiel, U. Vogt, W. Karpov, W. Sandner, and P. V. Nickles. Absolute extreme ultraviolet yield from femtosecond-laser-excited xe clusters. *Phys. Rev. E.*, 64:036404, 2001.

[16] V. Krainov and M. Smirnov. *Physics Reports*, 370:237, 2002.

[17] B. Breizman and A. Arefiev. *Plasma Physics Reports*, 29:642, 2003.

[18] M. H. Milchberg, S. J. McNaught, and E. Parra. Plasma hydrodynamics of the intense laser-cluster interaction. *Phys. Rev. E*, 64:056402, 2001.

[19] J. Kou, V. Zhakhovskii, S. Sakabe, K. Nishihara, S. Kawato, M. Hashida, K. Shimizu, S. Bulanov, Y. Izawa, Y. Kato, and N. Nakashima. Anisotropic coulomb explosion of c_{60} irradiated with high-intensity femtosecond laser pulse. *J. of Chem. Phys.*, 112(11):5012, 2000.

[20] N Hay, E. Springate, M. B. Mason, J. W. G. Tisch, M. Castillejo, and J. P. Marangos. Explosion of c_{60} irradiated with a high-intensity femtosecond laser pulse. *J. Phys. B*, 32:L17, 1999.

[21] V. Kumarappan, M. Krishnamurthy, and D. Mathur. Asymmetric high-energy ion emission from argon clusters in intense laser fields. *Phys. Rev. Lett.*, 87(8):085005–1, 2001.

[22] B. Shim, G. Hays, M. Downer, and T. Ditmire. *Bull. Am. Phys. Soc.*, 48, 2003.

[23] M. Fomytskyi, B. Breizman, A. Arefiev, and C. Chiu. Harmonic generation in clusters. *Phys. of Plasmas*, 11(7):3349, 2004.

[24] P. Sprangle, E. Esarey, J. Krall, and G. Joyce. *Phys. Rev. Lett.*, 69:2200, 1992.

[25] T. M. Antonsen and P. Mora. *Phys. Rev. Lett.*, 69:2204–2207, 1992.

[26] N. E. Andreev, L. M. Gorbunov, V. I. Kirsanov, A. A. Pogosova, and R. R. Ramazashviki. *JETP Lett.*, 55:571, 1992.

[27] Z. Najmudin, K. Krushelnik, E. L. Clark, S. P. D. Mangles, B. Walton, A. E. Dangor, S. Fritzler, V. Malka, E. Lefebvre, D. Gordon, F. S. Tsung, and C. Joshi. Self-modulated wakefield and forced laser wakefield acceleration of electrons. *Phys. of Plasmas*, 10(5):2071, 2003.

[28] R. Wagner, S. Y. Chen, A. Maksimchuk, and D. Umstadter. Electron acceleration by a laser wakefield in a relativistically self-guided channel. *Phys. Rev. Lett.*, 78:3125–3128, 1997.

[29] W. P. Leemans, D. Rodgers, P. E. Catravas, C. G. R. Geddes, G. Fubiani, E. Esarey, B. A. Shadwick, R. Donahue, and A. Smith. Gamma-neutron activation experiments using laser wakefield accelerators. *Phys. Plasmas*, 8:2510–2516, 2001.

[30] S. Y. Chen M. Krishnan, A. Maksimchuk, R. Wagner, and D. Umstadter. Detailed dynamics of electron beams self-trapped and accelerated in a self-modulated wakefield. *Phys. Plasmas*, 6:4739–4749, 1999.

[31] A. Modena, Z. Najmudin, A. E. Dangor, C. E. Clayton, K. A. Marsh, C. Joshi, V. Malka, C. B. Carrow, C. Danson, D. Neely, and F. N. Walsh. *Nature (London)*, 377:606, 1995.

[32] A. Ting, C. I. Moore, K. Krushelnik, C. Manka, E. Esarey, P. Sprangle, R. Hubbard, H. R. Burris, R. Fischer, and M. Baine. *Phys. Plasmas*, 4:1889, 1997.

[33] G. Malka, E. Lefebvre, and J. L. Miquel. *Phys. Rev. Lett.*, 78:3314, 1997.

[34] T. Tajima. *J. Jpn. Soc. Therap. Rad. Oncol.*, 9:2–5, 1997.

[35] C. Chiu, M. Fomytskyi, F. Grigsby, F. Raischel, M. Downer, and T. Tajima. Laser electron accelerator for radiation medicine: a feasibility study. in press, 2003.

[36] K. K. Kainz, K. R. Hogstrom, J. A. Antolak, P. R. Almond, C. D. Bloch, C. Chiu, M. Fomytskyi, F. Raischel, M. Downer, and T. Tajima. Dose properties of a laser accelerated electron beam and prospects for clinical application. in press, 2003.

[37] N. E. Andreev, V. I. Kirsanov, and L. M. Gorbunov. Stimulated processes and self-modulation of a short intense laser pulse in the laser wake-filed accelerator. *Phys. Plasmas*, 2(6):2573, 1995.

[38] D. L. Fisher and T. Tajima. Enhanced forward raman scattering. *Phys. Rev. E*, 53:1844–1851, 1996.

[39] M. Fomytskyi, C. Chiu, M. Downer, and F. Grigsby. Raman-seeded laser wakefield acceleration. 2004.

[40] N. E. Andreev, L. M. Gorbunovand, V. I. Kirsanov, A. A. Pogosova, and A. S. Sakharov. Theory of the resonance modulational instability of short laser pulses in a homogeneous plasma and plasma channels. *Plasmas Phys. Rep.*, 22(5):419–430, 1996.

[41] J. Dawson. Particle simulation of plasmas. *Rev. of Mod. Phys.*, 55(2):403, 1983.

[42] T. Tajima. *Computational Plasma Physics-with Applications to Fusion and Astrophysics.* Benjamin Frontier Series, Reading, MA, 1989.

[43] J. R. Cary and C. Nieter. Vorpal: an arbitrary dimensional hybrid code for computation of pulse propagation in laser-based advanced acceleration concepts. *Proc. 18th Annual Review of Progress in Applied Computational Electromagnetics (Monterey, CA, ACES)*, pages 549–555, 2002.

[44] C. Nieter and J. R. Cary. Vorpal: a versatile plasma simulation code. *J. Comp. Phys.*, 196:448, 2004.

[45] C. Nieter and J. R. Cary. *VORPAL as a Tool for the Study of Laser Pulse Propagation in LWFA*. Springer-Verlag, London, UK, 2002. p. 334-341.

[46] G. Mie. *Ann. Physik*, 25:377, 1908.

[47] F. Brunel. *Phys. Rev. Lett.*, 59:52, 1987.

[48] M. Fomytskyi, A. Arefiev, and B. Breizman. Explosion of laser-irradiated micro-clusters. In *2003 International Sherwood Fusion Theory Conference*, 2003.

[49] B. Breizman M. Fomytskyi, A. Arefiev, and C. Chiu. Nonlinear physics of laser-irradiated micro-clusters. In *2004 International Sherwood Fusion Theory Conference*, 2004.

[50] S. Fomichev, S. Popruzhenko, D. Zaretsky, and W. Becker. *Jornal of Physics B*, 36:3817, 2003.

[51] S. Fomichev, S. Popruzhenko, D. Zaretsky, and W. Becker. *Optical Express*, 11:2433, 2003.

[52] L. G. Gerchikov, C. Guet, and A. N. Ipatov. *Phys. Rev. A*, 66:053202, 2002.

[53] J. Zwaiback et. al. *Phys. Rev. Lett.*, 84:2634, 2000.

[54] W. H. Press et al. *Numerical Recipes in C++: The Art of Scientific Computing.* Cambridge University Press, 1992.

[55] A. Iserles. *Numerical Analysis of Differential Equations.* Cambridge University Press, 1997.

[56] T. Tajima and J. M. Dawson. Laser electron accelerator. *Phys. Rev. Lett.*, 43:267–270, 1979.

[57] V. Malka, S. Fritzler, E. Lefebvre, M. M. Aleonard, F. Burgy, J. P. Chambaret, J. F. Chemin, K. Krushelnick, G. Malka, S. P. D. Mangles, Z. Najmudin, M. Pittman, J. P. Rousseau, J. N. Scheurer, B. Walton, and A. E. Dangor. Electron acceleration by a wake field forced by an intense ultrashort laser pulse. *Science*, 298:1596, 2002.

[58] V. Bagnoud and F. Salin. Amplifying laser pulses to the terawatt level at a 1-kilohertz repetition rate. *Appl. Phys.*, pages S165–S170, 2000.

[59] N. E. Andreev, L. M. Gorbunov, and V. I. Kirsanov. Self-modulation of laser pulses in plasma and laser acceleration of electrons. *Plasmas Phys. Rep.*, 21(10):872–883, 1995.

[60] N. Zhavoronkov, F. Noack, V. Petrov, V. P. Kalosha, and J. Jerrmann. Chirped-pulse stimulated raman scattering in barium nitrate with subsequent recompression. *Opt. Lett.*, 26:47–49, 2001.

[61] Y. Kitagawa, T. Matsumoto, T. Minamihata, K. Sawai, K. Matsuo, K. Mima, K. Nishihara, H. Azechi, K. A. Tanaka, H. Takabe, and

S. Nakai. Beat-wave excitation of plasma wave and observation of accelerated electrons. *Phys. Rev. Lett.*, 68:48, 1992.

[62] C. E. Clayton, K. A. Marsh, A. Dyson, M. Everett, A. Lal, W. P. Leemans, R. Williams, and C. Joshi. Ultrahigh-gradient acceleration of injected electrons by laser-excited relativistic electron plasma waves. *Phys. Rev. Lett.*, 70:37, 1993.

[63] B. Walton, Z. Najmudin, M. S. Wei, C. Marle, R. J. Kingham, K. Krushelnick, A. E. Dangor, R. J. Clarke, M. J. Poulter, C. Hernandez-Gomez, S. Hawkes, D. Neely, J. L. Collier, C. N. Danson, S. Fritzler, and V. Malka. *Opt. Lett.*, 27:2203, 2002.

[64] A. K. Hankla, A. B. Bullock, W. E. White, J. A. Squier, and C. P. J. Barty. Tunable short-pulsebeat-wave laser source operating at 1mm. *Opt. lett.*, 22:1713, 1997.

[65] D. Neely, J. L. Collier, R. Allott, C. N. Danson, S. Hawkes, Z. Najmudin, R. J. Kingham, K. Krushelnick, and A. E. Dangor. Proposed beatwave experiment at ral with the vulcan cpa laser. *IEEE Trans. Plasma Science*, 28:1116, 2000.

[66] W. B. Mori. *IEEE J. Quant. Elec.*, 33:1942–953, 1997.

[67] C. D. Decker, W. B. Mori, and T. Katsouleas. *Phys. Plasma*, 3:1360, 1996.

[68] V. V. Goloviznin, P. W. van Amersfoort, N. E. Andreev, and V. I. Kirsanov. Self-resonant plasma wake-field excitation by a laser pulse with

a steep leading edge for particle acceleration. *Phys. Rev. E*, 52(5):5327–5332, 1995.

[69] D. Gordon, B. Hafizi, P. Sprangle, R. Hubbard, J. Penano, and W. Mori. Seeding of the forward raman instability by ionization fronts and raman backscatter. *Phys. Rev. E*, 64:046404, 2001.

[70] Z. M. Sheng, K. Mima, Y. Sentoku, K. Nishihara, and J. Zhang. Generation of high-amplitude plasma waves for particle acceleration by cross-modulated laser wake fields. *Physics of Plasmas*, 9:3147, 2002.

[71] E. Esarey and M. Pilloff. Trapping and acceleration in nonlinear plasma waves. *Phys. of Plasmas*, 2:1432, 1995.

[72] J. Dowson. Nonlinear electron oscillations in a cold plasma. *Phys. Rev.*, 113(2):383, 1959.

[73] E. Esarey, B. Hafizi, R. Hubbard, and A. Ting. Trapping and acceleration in self-modulated laser wakefields. *Phys. Rev. Lett.*, 80(25):5552, 1998.

[74] C. Moore, A. Ting, K Krushelnick E. Esarey R. Hubbard, B. Hafizi, H. Burris, C. Manka, and P. Sprangle. Electron trapping in self-modulated laser wakefields by raman backscatter. *Phys. Rev. Lett.*, 79(20):3909, 1997.

[75] E. Esarey, R. Hubbard, W. Leemans, A. Ting, and P. Sprangle. Electron injection into plasma wakefields by colliding laser pulses. *Phys. Rev. Lett.*, 79(14):2682, 1997.

[76] E. Esarey, J. Krall, and P. Sprangle. Envelope analysis of intense laser pulse self-modulation in plasmas. *Phys. Rev. Lett.*, 72:2887–2890, 1994.

[77] J. Krall, E. Esarey, P. Sprangle, and G. Joyce. Propagation of radius-tailored laser pulses over extended distances in a uniform plasma. *Phys. Plasmas*, 1(5):1738, 19944.

Vita

Mykhailo Fomyts'kyi was born on January 9, 1977 in Kiev, Ukraine (USSR at that time), the son of Vasilii Fomitsky and Elena Fomitskaya. In 1994 he finished lyceum #38 with advanced program in mathematics and computer science. The same year he got accepted to the department of Physics and Power Engineering of Moscow Institute of Physics and Technology (MIPT). The undergraduate research was done in the Moscow Institute of Space Research. In 1999 Mykhailo graduated from MIPT with a Bachelor of Science degree and entered the Ph.D. program in Physics at the University of Texas at Austin.

Permanent Address: 1801 S. Lakeshore #234,
Austin TX-78741

This dissertation was typeset with LaTeX 2_ε[1] by the author.

---

[1] LaTeX 2_ε is an extension of LaTeX. LaTeX is a collection of macros for TeX. TeX is a trademark of the American Mathematical Society. The macros used in formatting this dissertation were written by Dinesh Das, Department of Computer Sciences, The University of Texas at Austin, and extended by Bert Kay and James A. Bednar.